6-18-2020 2:30 PM

Plasmon-Enabled Physical and Chemical Transformations of Nanomaterials

Danielle McRae, *The University of Western Ontario*

Abstract

When the electromagnetic field of light is incident on metallic nanostructures of dimensions smaller than the incident wavelength of the light, there is a strong interaction, resulting in an enhanced, highly confined electromagnetic field in the vicinity of the nanostructure. This effect is referred to as a localized surface plasmon resonance, most commonly exploited for plasmon-enhanced spectroscopies, such as surface-enhanced Raman spectroscopy (SERS) and tip-enhanced Raman spectroscopy (TERS). The location, number and intensity of these regions of enhancement, or "hotspots", can be tuned by changing the nature of the metal, the size, shape and arrangement of the nanoparticles, its surroundings, or the wavelength of the incident light. When a molecule is located within these nanoscale hotspots, it is possible to obtain detailed spectroscopic information about the molecule with high sensitivity.

The decay process of these plasmon resonances can result in the ejection of high energy "hot" carriers, either hot electrons or hot holes, and the subsequent heating of the nanoparticle lattice. When a molecule is adsorbed to the surface of the nanoparticle, the presence of hot electrons and holes or the elevation of temperature can favour a chemical reaction. This effect is most prevalent in metallic nanostructures that exhibit hotspots at their surface, that can in turn be used to photocontrol surface reactions through plasmon excitation.

In this thesis, plasmon-mediated reactions are investigated using a variety of spectroscopic and microscopic techniques, along with the modelling of the light-matter interaction. The reduction of aryl diazonium salts on a gold nanostructured surface is plasmon-catalyzed. For a tip-enhanced Raman spectroscopy system involving a gold tip and a silver nanoplate as a substrate, plasmonic heating is discussed and modelled using finite element methods. New fractal metallic nanostructures are developed and studied for future applications in plasmon-mediated chemistry.

Keywords

Plasmonics, localized surface plasmon resonance, tip-enhanced Raman spectroscopy, surface-enhanced Raman spectroscopy, hot electrons, plasmon-mediated chemistry, diazonium salts, finite-difference time-domain, fractal nanostructures, electron-beam lithography, silver nanoplates

Summary for Lay Audience

Nanoparticles are particles of dimensions less than 100 nanometres, or about a thousand times smaller than the diameter of a human hair. Through a variety of synthesis approaches and techniques, nanoparticles can be made of many different materials and in many different shapes. Of note are metallic nanoparticles, most often made in gold or silver, which can exhibit a very strong interaction when illuminated with visible light. Interestingly, this interaction can be used for enhancing the signal of optical sensing techniques, improving the detection limit so that a signal can be obtained from a few, or even one, molecule. Some side effects of this process are the production of high energy electrons and local heating. These side effects can cause chemical reactions to occur under illumination by laser light when certain molecules are attached to these nanoparticles.

As these reactions are happening on such small scales, techniques with high spatial resolution are needed to observe their progress. These involve the interaction of light with the nanoparticles, with the signal enhanced by the local electric field of the nanoparticles, and the interaction of a sharp nanoscopic tip running along the surface of the nanoparticles, like a record player on the nanoscale, to obtain the topography of the sample. Combination of these two techniques, running a nanoparticle-decorated tip along a surface, gives both the topography and an enhanced signal with a spatial resolution of several nanometres.

Here, these reactions are studied using these techniques, along with the response as predicted by simulations. One such reaction studied here is the grafting of a diazonium salt on a gold surface. The rate of chemical reactions can be augmented by the production of high energy electrons, or through local heating, as heat acts as an energy source for the reaction. To study the latter for a more complex system, involving a sharp gold-coated tip and a flat silver nanoplate, the heating process is modelled by simulations and compared to experimental observations. Finally, new nanoparticles are made based on different self-similar, fractal patterns, and these are characterized for future applications in chemistry.

Co-Authorship Statement

Prof. François Lagugné-Labarthet was the corresponding author on the papers presented in this thesis, and was responsible for the supervision of Danielle McRae over the course of her studies. This thesis includes materials from four publications, all of which had contributions from co-authors.

Danielle McRae was the primary author of the paper presented in Chapter 5. She was responsible for the acquisition of the experimental work in the paper, as well as the writing and revision for all drafts, including the final manuscripts. For the works in Chapter 6, she was a primary and a secondary/tertiary author, responsible for some of the experimental work and the simulations. Throughout this work, data was acquired or jointly acquired and analyzed by co-authors as summarized below:

Chapter 5:

McRae, D. M.; Jeon, K.; Lagugné-Labarthet, F. Plasmon-Mediated Drilling in Thin Metallic Nanostructures. *ACS Omega*, **2018**, *3*, 7269–7277

Keuna Jeon was responsible for synthesis of the silver nanoplates, and their characterization by absorption spectroscopy. Danielle McRae was responsible for all electron microscopy, atomic force microscopy, optical microscopy, Raman spectroscopic measurements and simulations.

Chapter 6:

McRae, D. M.; Therien, D.A.B.; Hou, R.; Wallace, G. Q.; Lagugné-Labarthet, F. Sierpiński Fractals as Plasmonic Metastructures for Second-Harmonic Generation. *ACS Appl. Nano Mater.,* **2020**, *3,* 3922-3929.

Danielle McRae was responsible for the acquisition of the SERS maps, simulations and analysis, as included here. Alex Therien and Dr. Renjie Hou assisted with the acquisition of the second-harmonic generation data, and Dr. Greg Wallace provided optical characterization of the gold Sierpiński fractals, which are not included here.

Bicket, I.; Bellido, E.; **McRae, D. M.**; Lagugné-Labarthet, F.; Botton, G. Carving Plasmon Modes in Silver Sierpinski Fractals. *ACS Photonics*, **2019**, *6*, 2974-2984.

Isobel Bicket and Dr. Edson Bellido were involved with the acquisition and analysis of the experimental EELS data, and Isobel Bicket was responsible for the writing of the manuscript. Danielle McRae was responsible for the results as simulated by FDTD.

Wallace, G. Q.; **McRae, D. M.**; Lagugné-Labarthet, F. Probing Mid-Infrared Plasmon Resonances in Extended Radial Fractal Structures. *Opt. Lett.*, **2019**, *44*, 3865-3868.

Dr. Greg Wallace was responsible for the analysis of the experimental data and writing the manuscript. Danielle McRae was responsible for the FDTD simulations and the associated isowavelength maps.

Acknowledgments

This work would not have been possible without the direction of my supervisor, Prof. François Lagugné-Labarthet. His guidance and mentorship throughout my degree served as a cornerstone to the development of my research abilities, and I thank him for his involvement in what is an ongoing process.

I have had the pleasure of working alongside some amazing people in the FLL group, and I am grateful for their guidance and friendship. Over the years, this has included, but isn't limited to: Dr. Greg Wallace, Lauren Katz, Alex Therien, Sydney Legge, María Olivia Avilés, Dr. Leila Mazaheri, Pooneh Farhat and Nina Ćulum. I am also thankful for having had the opportunity to supervise undergraduate students, Keuna Jeon and Kara Ly.

I would like to acknowledge all those who have had a role in my research. I appreciate help and support of Tim Goldhawk and Dr. Todd Simpson of the Western Nanofabrication Facility, Mary Jane Walzak of Surface Science Western and Dr. Max Eisele of Neaspec GmbH. I appreciate the help of Dr. Fraser Filice with the FEM simulations. I was fortunate enough to receive funding from Mitacs to travel to Paris to work with our collaborators at the Université de Paris, to whom I am grateful: Prof. Nordin Félidj, Prof. Claire Mangeney, Théo Geronimi-Jourdain and Dr. Issam Kherbouche. Finally, I would like to thank our collaborators at the Canadian Centre for Electron Microscopy at McMaster University: Isobel Bicket, Dr. Edson Bellido and Prof. Gianluigi Botton.

Lastly, I want to thank my friends and family: Emma Jorgenson, for proofreading; the women and girls of my Sparks and Guides units, a welcome distraction; and Mom, Dad and Mike, for all their love and support.

Table of Contents

List of Figures

List of Abbreviations, Symbols and Nomenclature

α	polarizability
α_r	half-angle of aperture of objective lens
β	correction factor
χ	shape factor of a nanoparticle
ε_0	permittivity of free space
ε_d	dielectric constant of a dielectric
ε_m	dielectric constant of a metal
λ	wavelength
Λ	grating period
θ	angle of incidence
σ	conductivity
$\sigma_{abs/ext/scat}$	absorption/extinction/scattering cross-section
ω_p	plasmon frequency
4-MPBA	4-mercaptophenylboronic acid
4-NTP	4-nitrothiophenol
AFM	atomic force microscopy
B	magnetic flux density
c	speed of light
CCD	charge-coupled device

C_p	heat capacity at constant pressure
e	elementary charge
E	electric field
E_F	Fermi energy
EBL	electron-beam lithography
EDX	energy-dispersive X-ray spectroscopy
EELS	electron energy loss spectroscopy
EF	enhancement factor
EM	electromagnetic
FDTD	finite-difference time-domain
FEM	finite element method
FTIR	Fourier transform infrared
h	Planck's constant
H	magnetic field strength
HAADF	high-angle annular dark-field imaging
I	light intensity
IR	infrared
J	current density
κ	thermal conductivity
k	wavevector

k_b	Boltzmann constant
LIPSS	laser-induced periodic surface structure
LSPR	localized surface plasmon resonance
m_e	effective mass of an electron
n	refractive index
NA	numerical aperture
n_e	number of electrons
NSL	nanosphere lithography
PML	perfectly matched layer
q	normal coordinate
q_{EM}	electromagnetic power loss density
Q	external heat source
QCL	quantum cascade laser
R	radius of nanoparticle
RMS	root mean square
SEM	scanning electron microscopy
SEIRA	surface-enhanced infrared absorption
SERS	surface-enhanced Raman spectroscopy
s-SNOM	scattering scanning near-field optical microscopy
STEM	scanning transmission electron microscopy

T	temperature
t	time
T_{el}	electron temperature
TERS	tip-enhanced Raman spectroscopy
ρ	density
ν	frequency of vibration
V	volume of nanoparticle

List of Appendices

Chapter 1

1 General Introduction

When illuminated by an electromagnetic wave of visible light, metallic nanostructures can exhibit local enhancement of the electromagnetic field confined in their vicinity; this phenomenon is called localized surface plasmon resonance (LSPR).[1,2] Most commonly, this electromagnetic enhancement is exploited for plasmon-enhanced spectroscopies, the most prominent of which is surface-enhanced Raman spectroscopy (SERS). When a molecule is located within the nanoscale regions of enhancement, it is possible to achieve detailed spectroscopic information about the molecule, with sensitivity down to the single-molecule level.[3,4] Through the effects of the enhanced electric field, and the localized heating and ejection of high-energy electrons and holes that are the result of the LSPR, chemical reactions can be triggered in these regions.[5-7] We explore in this thesis tuning these regions of enhanced electric field, and exploiting them for plasmon-enhanced spectroscopies and catalyzing chemical reactions.

1.1 Plasmon-Mediated Chemistry

The use of plasmons to mediate chemical reactions was first proposed in 1981,[8] and experimentally realized two years later, in a reaction involving cadmium nanoparticles.[9] The field of plasmon-mediated chemistry grew in the 2000s, following the demonstration of the oxidation of *para*-aminothiophenol to 4,4'-dimercaptoazobenzene during SERS measurements.[10,11] This coupling reaction, and that of *para*-nitrothiophenol, remain the most studied plasmon-mediated reactions, often used as a model for determining the involved mechanisms.[12-15]

In parallel, plasmonic nanoparticles were emerging as a new class of hybrid photocatalysts, as Tian *et al.* demonstrated that the incorporation of small gold nanoparticles in porous titanium dioxide films photocatalyzed the oxidation of methanol and ethanol.[16]

1.1.1   Chemical Reactions of Interest

In recent years, plasmon resonances have been used to catalyze increasingly complex chemical reactions. Many reactions have been reported, including the oxidation of carbon monoxide,[17,18] alcohols,[16,19] alkenes,[20] and amines;[21,22] reduction of alkenes and alkynes,[23,24] aldehydes and ketones;[25,26] and coupling reactions.[27-29] For the latter, the Suzuki-Miyaura cross-coupling reaction has emerged as a model reaction, plasmon-catalyzed by Pd-Au nanostructures (Figure 1-1a). These nanostructures include bimetallic alloys[30] and core-partial shell structures involving gold nanorods,[31,32] although other geometries like gold nanoprisms and bipyramids have been exploited for the increased electromagnetic field localization at their apices.[33,34] The cleavage of C-N bonds in benzyl viologen and ethyl viologen has been shown to be plasmon-driven, and can be monitored by SERS.[35] SERS has also been used to monitor other plasmon-mediated reactions, such as the methyl cleavage on methylene blue[36,37] and ethylene epoxidation.[38]

Recently, work has shown that plasmon-catalyzed reactions may be the result of photo-activated O_2 at the surface, as opposed to the direct transfer of hot electrons or holes.[39-41] Takeuchi *et al.* demonstrated the oxidation of alkanes *para*-methylthiophenol, decylamine, and 1-butanethiol on silver nanoparticles under green light excitation, attributing the oxidation to activated oxygen species (Figure 1-1b).[42] Polymerization reactions, as shown in Figure 1-1c, have also been shown to be plasmon-catalyzed, such as that of diazonium salts,[43-45] resulting in the formation of thick poly(aryl) layers, and divinylbenzene, styrene and methyl methacrylate.[46] Interestingly, such polymerization reactions also shift the frequency of the plasmon mode, allowing for tuning of the mode frequency through a plasmon-mediated reaction.[47]

On a larger scale, the synthesis of metal nanoparticles can be catalyzed by plasmon resonance;[48] the most common example of this is the synthesis of monodisperse silver nanoplates by the irradiation of small silver nanoparticles.[49-52] However, many different nanoparticle geometries have been generated through plasmon-mediated syntheses, including highly anisotropic structures like bipyramids[52,53] and icosahedra.[54,55] These

syntheses are usually attributed to the plasmon-mediated oxidation of citrate (Figure 1-1d), which in turn reduces the metal precursor.[56,57]
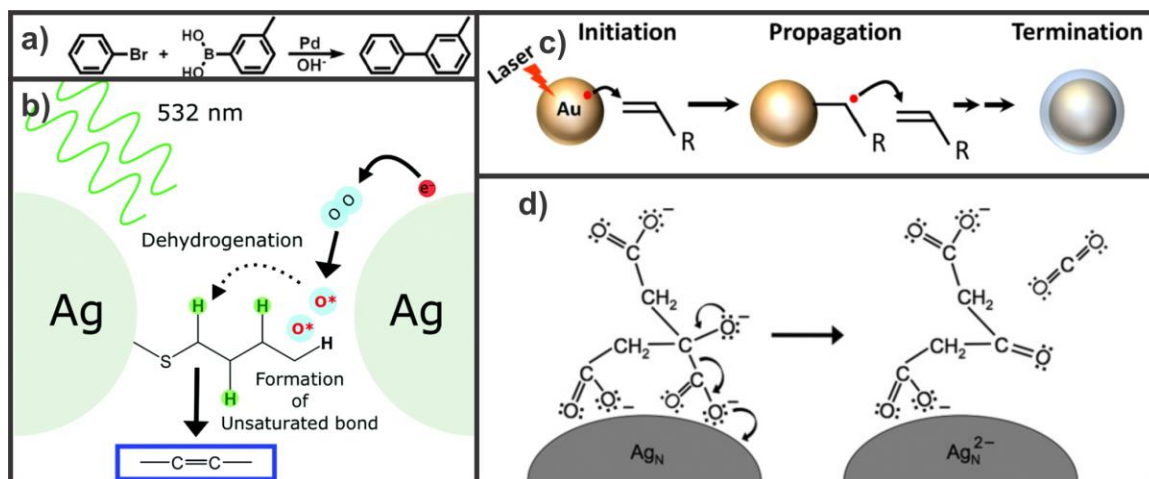
Figure 1-1 a) Suzuki-Miyaura cross-coupling of bromobenzene and *m*-tolylboronic acid, as catalyzed by plasmonic Pd-decorated Au nanorods;[31] Adapted with permission from ref. [31]. Copyright 2019 Wiley-VCH. b) Proposed mechanism for the dehydrogenation of alkanes by activated oxygen species produced by plasmon resonance;[42] Reproduced with permission from ref. [42]. Copyright 2019 Royal Society of Chemistry. c) Mechanism of plasmon-induced polymerization;[46] Reproduced with permission from ref. [46]. Copyright 2018 Springer Nature. d) Proposed mechanism for the oxidation of citrate in the plasmon-mediated synthesis of metallic nanoparticles.[48] Reproduced with permission from ref. [48]. Copyright 2013 Wiley-VCH.

1.1.2   Applications to Energy Storage and CO_2 Reduction

Examples of chemical reactions of societal importance are water splitting, for the production of dihydrogen as an energy source, and carbon dioxide reduction, for the reduction of pollution and its role in climate change. These reactions could be applied on larger scales if they could be catalyzed by sunlight. One barrier to these large-scale applications is the short lifetime of hot carriers, which decay on the femtosecond timescale, often before coupling to a chemical reaction.[58,59] The lifetime of these hot carriers can be extended through the formation of a Schottky barrier (Figure 1-2a) at the

interface between a noble metal and a large bandgap semiconductor, as this leads to an accumulation of hot electrons at the conduction band of the semiconductor, and hot holes at the Fermi level of the metal.[60,61] This has led to a new class of hybrid photocatalysts with improved efficiencies. Formation of these hybrid photocatalysts involves incorporation of plasmonic nanoparticles, often gold or silver nanorods or nanospheres, into semiconductors films or arrays, usually of TiO_2. Critical to the performance of these photocatalysts is the formation of the physical interfaces, and an appropriate band alignment between the Fermi level of the metal and the conduction band of the semiconductor.[61] For the former, it has been shown that the electromagnetic enhancement at the interface influences the number of electrons tunneling through the Schottky barrier, further influencing the reaction in question.[62,63]

Water splitting using a TiO_2 photoanode was first demonstrated by Fujishima and Honda in 1972, followed by the reduction of CO_2 in 1979.[64,65] Since then, TiO_2, and other wide band semiconductors such as WO_3 and CeO_2,[66,67] have been used for applications in photoelectrochemical reactions, due to their stability over broadband semiconductors such as Si, CdS and CdSe, which are prone to photocorrosion.[68,69] Due to its wide band gap, TiO_2 responds only in the ultraviolet (UV) region of the spectrum, resulting in a limited efficiency;[69,70] this is also an issue for wide-scale applications, considering that UV light constitutes only 5% of solar radiation.[71] It is therefore desirable to sensitize these semiconductors to energies below that of the band gap, particularly those corresponding to visible light, improving the conversion ratio between solar energy and H_2 production (or CO_2 reduction). This can be improved by doping or photosensitizing wide band semiconductors.[72,73] Plasmonic nanoparticles are ideal candidates as photosensitizing agents, as they absorb strongly in the visible spectrum, and can transfer energy to the semiconductors either through resonant energy transfer or directly, through hot electron injection.[74] The absorption of plasmonic nanoparticles is tunable, allowing for broadband absorption.

Plasmonic nanoparticles have been incorporated into semiconductor arrays and nanoparticles in many different morphologies. Ideally, there is a direct contact area between the plasmonic nanoparticle and the semiconductor for efficient charge separation

to occur.[70] Semiconductors take the form of planar thin films, arrays of nanowires or nanorods, or porous arrays of nanowires, as shown in Figure 1-2b – 1-2d.[75-77] Plasmonic nanoparticles can be embedded or buried in the semiconductor support, or isolated from it with a thin dielectric layer.[78] Recent work has focused on designing new hybrid photocatalyst morphologies in order to improve conversion efficiencies at increasingly longer wavelengths. Recently, Naya *et al.* demonstrated water splitting under irradiation by red light (640 nm) using a half-cut Au core-CdS shell structure with a high quantum yield of 0.24%.[79] Core-shell structures allow for good contact between the semiconductor and plasmonic nanoparticle, but can impede the reactant supply to the core and diffusion of the products; a half-cut allows for diffusion to the core while maintaining the metal-semiconductor contact. Importantly, the photo-dissolution of CdS may be suppressed by the selective excitation of the LSPR of the gold nanoparticles.

The incorporation of plasmonic nanoparticles may have advantages beyond enhanced broadband efficiencies. In the reduction of CO_2 under visible light as photocatalyzed by small silver nanoparticles, Kumari *et al.* perform dynamic *in situ* SERS measurements (Figure 1-2e). This allows for the identification of reaction intermediates, such as the surface-adsorbed hydrocarbonyl HOCO*, and elucidation of the reaction mechanism.[80]
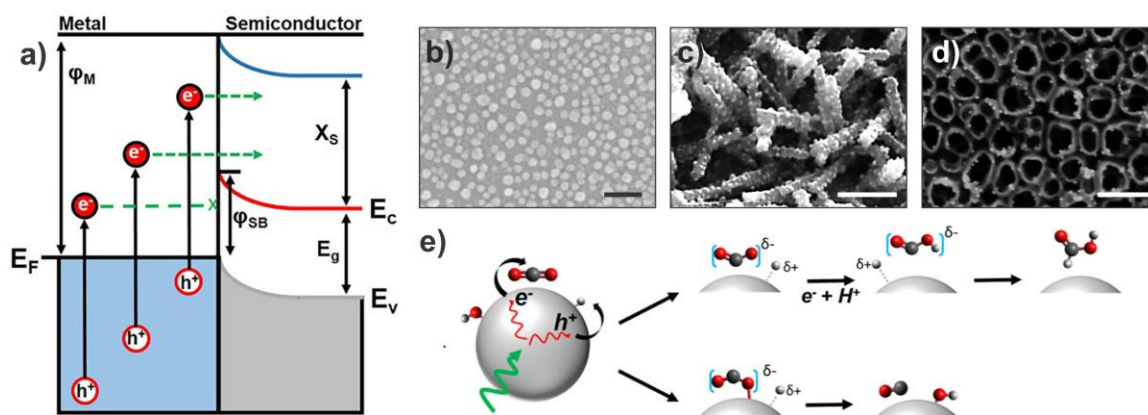
Figure 1-2 a) Plasmon-induced hot carrier generation in a metal in contact with a semiconductor. A proportion of hot electrons has sufficient energy to pass the Schottky barrier of height φ_{SB}, and are injected into the semiconductor.[81] Reproduced with permission from ref. [81]. Copyright 2014 Elsevier. Scanning electron micrographs of hybrid photocatalysts: b) with gold nanoparticles on a TiO_2

film;[75] Adapted with permission from ref. [75]. Copyright 2013 Elsevier. c) semiconductor nanowire arrays sensitized by core-shell gold nanoparticles;[76] Adapted with permission from ref. [76]. Copyright 2014 American Chemical Society. d) of a porous nanotube array, decorated with gold nanoparticles.[77] Adapted with permission from reference [77]. Copyright 2014 Elsevier. Scale bars are 200 nm. e) Proposed mechanisms of CO_2 reduction under visible light, as determined by SERS.[80] Adapted with permission from ref. [80]. Copyright 2018 American Chemical Society.

1.2 Scope of Thesis

The present thesis is organized as follows:

In Chapter 2, the essential theoretical background for the understanding of plasmon-mediated chemistry is provided. The principles of Raman spectroscopy and plasmonics are described, and their combination in the plasmon-enhanced spectroscopies, surface- and tip-enhanced Raman spectroscopy, is described. Finally, the mechanism of plasmon decay and coupling to chemical reactions is elaborated.

The experimental methods are described in Chapter 3, providing technical details of the spectroscopy and microscopy measurements that follow, as well as details of the calculations and synthesis of metallic nanostructures.

In Chapter 4, the plasmon-catalyzed reduction of aryl diazonium salts on gold surfaces is discussed. The reaction is investigated on different surfaces: gold nanoislands of random shape and size, and gold nanoprisms patterned by nanosphere lithography.

Chapter 5 of this thesis focusses on the tip-enhanced Raman spectroscopic measurements on silver nanoplates. Local ablation of the nanoplates is observed, and the possible causes, including plasmonic heating, are discussed.

Chapter 6 contains details of designing fractal nanostructures for future applications in plasmon-mediated chemistry. As the fractal generation is increased, the changes in the plasmonic response and subsequent optical properties are predicted by calculations, and

observed experimentally by nano-FTIR and electron energy loss spectroscopy combined with scanning transmission electron microscopy.

In the conclusion chapter, the present work is summarized, and we give a review of the emerging fields in plasmon-mediated chemistry and their wider applications.

1.3　　References

1.　　Willets, K. A.; Van Duyne, R. P. *Annu. Rev. Phys. Chem.* **2007**, *58*, 267-297.

2.　　Jiang, N.; Zhuo, X.; Wang, J. *Chem. Rev.* **2018**, *118*, 3054-3099.

3.　　Csaki, A.; Schneider, T.; Wirth, J.; Jahr, N.; Steinbrück, A.; Stranik, O.; Garwe, F.; Müller, R.; Fritzsche, W. *Philos. Trans. R. Soc. A* **2011**, *369*, 3483-3496.

4.　　Le Ru, E. C.; Etchegoin, P. G. *Annu. Rev. Phys. Chem.* **2012**, *63*, 65-87.

5.　　Gellé, A.; Jin, T.; de la Garza, L.; Price, G. D.; Besteiro, L. V.; Moores, A. *Chem. Rev.* **2020**, *120*, 986-1041.

6.　　Ren, X.; Cao, E.; Lin, W.; Song, Y.; Liang, W.; Wang, J. *RSC Adv.* **2017**, *7*, 31189-31203.

7.　　Zhan, C.; Chen, X.-J.; Yi, J.; Li, J.-F.; Wu, D.-Y.; Tian, Z.-Q. *Nat. Rev. Chem.* **2018**, *2*, 216-230.

8.　　Nitzan, A.; Brus, L. E. *J. Chem. Phys.* **1981**, *75*, 2205-2214.

9.　　Chen, C. J.; Osgood, R. M. *Phys. Rev. Lett.* **1983**, *50*, 1705-1708.

10.　　Huang, Y.-F.; Zhu, H.-P.; Liu, G.-K.; Wu, D.-Y.; Ren, B.; Tian, Z.-Q. *J. Am. Chem. Soc.* **2010**, *132*, 9244-9246.

11.　　Wu, D.-Y.; Liu, X.-M.; Huang, Y.-F.; Ren, B.; Xu, X.; Tian, Z.-Q. *J. Phys. Chem. C* **2009**, *113*, 18212-18222.

12.　　Kafle, B.; Poveda, M.; Habteyes, T. G. *J. Phys. Chem. Lett.* **2017**, *8*, 890-894.

13.　　Sarhan, R. M.; Koopman, W.; Schuetz, R.; Schmid, T.; Liebig, F.; Koetz, J.; Bargheer, M. *Sci. Rep.* **2019**, *9*, 3060.

14.　　van Schrojenstein Lantman, E. M.; Deckert-Gaudig, T.; Mank, A. J. G.; Deckert, V.; Weckhuysen, B. M. *Nat. Nanotechnol.* **2012**, *7*, 583-586.

15.　　Zhang, Z.; Merk, V.; Hermanns, A.; Unger, W. E. S.; Kneipp, J. *ACS Catal.* **2017**, *7*, 7803-7809.

16.　　Tian, Y.; Tatsuma, T. *J. Am. Chem. Soc.* **2005**, *127*, 7632-7637.

17.　　Jia, C.-J.; Liu, Y.; Bongard, H.; Schüth, F. *J. Am. Chem. Soc.* **2010**, *132*, 1520-1522.

18.　　Kim, S. M.; Lee, S. J.; Kim, S. H.; Kwon, S.; Yee, K. J.; Song, H.; Somorjai, G. A.; Park, J. Y. *Nano Lett.* **2013**, *13*, 1352-1358.

19. Liu, L.; Ouyang, S.; Ye, J. *Angew. Chem. Int. Ed.* **2013**, *52*, 6689-6693.

20. Christopher, P.; Xin, H.; Linic, S. *Nat. Chem.* **2011**, *3*, 467-472.

21. Wang, J.; Ando, R. A.; Camargo, P. H. C. *Angew. Chem. Int. Ed.* **2015**, *54*, 6909-6912.

22. Zhai, Z.-Y.; Guo, X.-N.; Jin, G.-Q.; Guo, X.-Y. *Catal. Sci.* **2015**, *5*, 4202-4207.

23. Quiroz, J.; Barbosa, E. C. M.; Araujo, T. P.; Fiorio, J. L.; Wang, Y.-C.; Zou, Y.-C.; Mou, T.; Alves, T. V.; de Oliveira, D. C.; Wang, B.; Haigh, S. J.; Rossi, L. M.; Camargo, P. H. C. *Nano Lett.* **2018**, *18*, 7289-7297.

24. Zhao, X.; Long, R.; Liu, D.; Luo, B.; Xiong, Y. *J. Mater. Chem. A* **2015**, *3*, 9390-9394.

25. Landry, M. J.; Gellé, A.; Meng, B. Y.; Barrett, C. J.; Moores, A. *ACS Catal.* **2017**, *7*, 6128-6133.

26. Hao, C.-H.; Guo, X.-N.; Pan, Y.-T.; Chen, S.; Jiao, Z.-F.; Yang, H.; Guo, X.-Y. *J. Am. Chem. Soc.* **2016**, *138*, 9361-9364.

27. Mohammadparast, F.; Dadgar, A. P.; Tirumala, R. T. A.; Mohammad, S.; Topal, C. O.; Kalkan, A. K.; Andiappan, M. *J. Phys. Chem. C* **2019**, *123*, 11539-11545.

28. González-Béjar, M.; Peters, K.; Hallett-Tapley, G. L.; Grenier, M.; Scaiano, J. C. *Chem. Commun.* **2013**, *49*, 1732-1734.

29. Lanterna, A. E.; Elhage, A.; Scaiano, J. C. *Catal. Sci.* **2015**, *5*, 4336-4340.

30. Sarina, S.; Zhu, H.; Jaatinen, E.; Xiao, Q.; Liu, H.; Jia, J.; Chen, C.; Zhao, J. *J. Am. Chem. Soc.* **2013**, *135*, 5793-5801.

31. Verkaaik, M.; Grote, R.; Meulendijks, N.; Sastre, F.; Weckhuysen, B. M.; Buskens, P. *ChemCatChem* **2019**, *11*, 4974-4980.

32. Wang, F.; Li, C.; Chen, H.; Jiang, R.; Sun, L.-D.; Li, Q.; Wang, J.; Yu, J. C.; Yan, C.-H. *J. Am. Chem. Soc.* **2013**, *135*, 5588-5601.

33. Gangishetty, M. K.; Fontes, A. M.; Malta, M.; Kelly, T. L.; Scott, R. W. J. *RSC Adv.* **2017**, *7*, 40218-40226.

34. Zhu, X.; Jia, H.; Zhu, X.-M.; Cheng, S.; Zhuo, X.; Qin, F.; Yang, Z.; Wang, J. *Adv. Funct. Mater.* **2017**, *27*, 1700016.

35. Brooks, J. L.; Chulhai, D. V.; Yu, Z.; Goodpaster, J. D.; Frontiera, R. R. *J. Phys. Chem. C* **2019**, *123*, 29306-29313.

36. Tesema, T. E.; Annesley, C.; Habteyes, T. G. *J. Phys. Chem. C* **2018**, *122*, 19831-19841.

37. Tesema, T. E.; Kafle, B.; Tadesse, M. G.; Habteyes, T. G. *J. Phys. Chem. C* **2017**, *121*, 7421-7428.

38. Zhang, X.; Kumari, G.; Heo, J.; Jain, P. K. *Nat. Commun.* **2018**, *9*, 3056.

39. Seemala, B.; Therrien, A. J.; Lou, M.; Li, K.; Finzel, J. P.; Qi, J.; Nordlander, P.; Christopher, P. *ACS Energy Lett.* **2019**, *4*, 1803-1809.

40. Huang, Y.-F.; Zhang, M.; Zhao, L.-B.; Feng, J.-M.; Wu, D.-Y.; Ren, B.; Tian, Z.-Q. *Angew. Chem. Int. Ed.* **2014**, *53*, 2353-2357.

41. Macia, N.; Kabanov, V.; Heyne, B. *J. Phys. Chem. C* **2020**, *124*, 3768-3777.

42. Takeuchi, Y.; Fujita, T.; Takeyasu, N. *Phys. Chem. Chem. Phys.* **2019**, *21*, 7502-7507.

43. Nguyen, M.; Kherbouche, I.; Gam-Derouich, S.; Ragheb, I.; Lau-Truong, S.; Lamouri, A.; Lévi, G.; Aubard, J.; Decorse, P.; Félidj, N.; Mangeney, C. *Chem. Commun.* **2017**, *53*, 11364-11367.

44. Nguyen, V.-Q.; Ai, Y.; Martin, P.; Lacroix, J.-C. *ACS Omega* **2017**, *2*, 1947-1955.

45. Tijunelyte, I.; Kherbouche, I.; Gam-Derouich, S.; Nguyen, M.; Lidgi-Guigui, N.; de la Chapelle, M. L.; Lamouri, A.; Lévi, G.; Aubard, J.; Chevillot-Biraud, A.; Mangeney, C.; Felidj, N. *Nanoscale Horiz.* **2018**, *3*, 53-57.

46. Wang, Y.; Wang, S.; Zhang, S.; Scherman, O. A.; Baumberg, J. J.; Ding, T.; Xu, H. *Nano Res.* **2018**, *11*, 6384-6390.

47. Ding, T.; Mertens, J.; Lombardi, A.; Scherman, O. A.; Baumberg, J. J. *ACS Photonics* **2017**, *4*, 1453-1458.

48. Langille, M. R.; Personick, M. L.; Mirkin, C. A. *Angew. Chem. Int. Ed.* **2013**, *52*, 13910-13940.

49. Lee, S.-W.; Chang, S.-H.; Lai, Y.-S.; Lin, C.-C.; Tsai, C.-M.; Lee, Y.-C.; Chen, J.-C.; Huang, C.-L. *Materials* **2014**, *7*, 7781-7798.

50. Xue, B.; Wang, D.; Zuo, J.; Kong, X.; Zhang, Y.; Liu, X.; Tu, L.; Chang, Y.; Li, C.; Wu, F.; Zeng, Q.; Zhao, H.; Zhao, H.; Zhang, H. *Nanoscale* **2015**, *7*, 8048-8057.

51. Jin, R.; Cao, Y.; Mirkin, C. A.; Kelly, K. L.; Schatz, G. C.; Zheng, J. G. *Science* **2001**, *294*, 1901-1903.

52. Zhang, J.; Langille, M. R.; Mirkin, C. A. *J. Am. Chem. Soc.* **2010**, *132*, 12502-12510.

53. Zhang, J.; Li, S.; Wu, J.; Schatz, G. C.; Mirkin, C. A. *Angew. Chem. Int. Ed.* **2009**, *48*, 7787-7791.

54. Keunen, R.; Cathcart, N.; Kitaev, V. *Nanoscale* **2014**, *6*, 8045-8051.

55. Langille, M. R.; Zhang, J.; Mirkin, C. A. *Angew. Chem. Int. Ed.* **2011**, *50*, 3543-3547.

56. Redmond, P. L.; Wu, X.; Brus, L. *J. Phys. Chem. C* **2007**, *111*, 8942-8947.

57. Thrall, E. S.; Preska Steinberg, A.; Wu, X.; Brus, L. E. *J. Phys. Chem. C* **2013**, *117*, 26238-26247.

58. Christopher, P.; Moskovits, M. *Annu. Rev. Phys. Chem.* **2017**, *68*, 379-398.

59. Brongersma, M. L.; Halas, N. J.; Nordlander, P. *Nat. Nanotechnol.* **2015**, *10*, 25-34.

60. Khan, M. R.; Chuan, T. W.; Yousuf, A.; Chowdhury, M. N. K.; Cheng, C. K. *Catal. Sci.* **2015**, *5*, 2522-2531.

61. Negrín-Montecelo, Y.; Comesaña-Hermo, M.; Khorashad, L. K.; Sousa-Castillo, A.; Wang, Z.; Pérez-Lorenzo, M.; Liedl, T.; Govorov, A. O.; Correa-Duarte, M. A. *ACS Energy Lett.* **2020**, *5*, 395-402.

62. Kong, X.-T.; Wang, Z.; Govorov, A. O. *Adv. Opt. Mater.* **2017**, *5*.

63. Sousa-Castillo, A.; Comesaña-Hermo, M.; Rodríguez-González, B.; Pérez-Lorenzo, M.; Wang, Z.; Kong, X.-T.; Govorov, A. O.; Correa-Duarte, M. A. *J. Phys. Chem. C* **2016**, *120*, 11690-11699.

64. Fujishima, A.; Honda, K. *Nature* **1972**, *238*, 37-38.

65. Inoue, T.; Fujishima, A.; Konishi, S.; Honda, K. *Nature* **1979**, *277*, 637-638.

66. Rani, B. J.; Kumar, M. P.; Ravichandran, S.; Ravi, G.; Ganesh, V.; Guduru, R. K.; Yuvakkumar, R.; Hong, S. I. *J. Phys. Chem. Solids* **2019**, *134*, 149-156.

67. Wu, T.; Vegge, T.; Hansen, H. A. *ACS Catal.* **2019**, *9*, 4853-4861.

68. Takayama, K.; Fujiwara, K.; Kume, T.; Naya, S.-i.; Tada, H. *J. Phys. Chem. Lett.* **2017**, *8*, 86-90.

69. Lee, J.; Mubeen, S.; Ji, X.; Stucky, G. D.; Moskovits, M. *Nano Lett.* **2012**, *12*, 5014-5019.

70. Zheng, Z.; Xie, W.; Huang, B.; Dai, Y. *Chem. Eur. J.* **2018**, *24*, 18322-18333.

71. Ueno, K.; Oshikiri, T.; Misawa, H. *ChemPhysChem* **2016**, *17*, 199-215.

72. Morikawa, T.; Sato, S.; Sekizawa, K.; Arai, T.; Suzuki, T. M. *ChemSusChem* **2019**, *12*, 1807-1824.

73. Shao, W.; Wang, H.; Zhang, X. *Dalton Trans.* **2018**, *47*, 12642-12646.

74. Warren, S. C.; Thimsen, E. *Energy Environ. Sci.* **2012**, *5*, 5133-5146.

75. Chen, W.; Lu, Y.; Dong, W.; Chen, Z.; Shen, M. *Mater. Res. Bull.* **2014**, *50*, 31-35.

76. Shan, Z.; Clayton, D.; Pan, S.; Archana, P. S.; Gupta, A. *J. Phys. Chem. B* **2014**, *118*, 14037-14046.

77. Wu, L.; Li, F.; Xu, Y.; Zhang, J. W.; Zhang, D.; Li, G.; Li, H. *Appl. Catal. B* **2015**, *164*, 217-224.

78. Liu, G.; Du, K.; Xu, J.; Chen, G.; Gu, M.; Yang, C.; Wang, K.; Jakobsen, H. *J. Mater. Chem. A* **2017**, *5*, 4233-4253.

79. Naya, S.-i.; Kume, T.; Akashi, R.; Fujishima, M.; Tada, H. *J. Am. Chem. Soc.* **2018**, *140*, 1251-1254.

80.   Kumari, G.; Zhang, X.; Devasia, D.; Heo, J.; Jain, P. K. *ACS Nano* **2018**, *12*, 8330-8340.

81.   Marchuk, K.; Willets, K. A. *Chem. Phys.* **2014**, *445*, 95-104.

Chapter 2

2 Plasmon-Enhanced Spectroscopies

The application of plasmonic platforms for plasmon-mediated reactions requires a preliminary understanding of the optical properties of these structures in order to further exploit the plasmon resonances to trigger selected chemical surface reactions. Simultaneously, the Raman measurements of analytes deposited at the surface of these platforms allow for a better understanding of the properties of the material before and after photoinduced reactions. The principles of Raman spectroscopy and plasmonics that are presented in this chapter form a basis to support the research work that follows in this thesis.

2.1 Principles of Raman Spectroscopy

The process of inelastic scattering of light by molecules was discovered in the early twentieth century by Chandrashekhara Venkata Raman, an Indian physicist. His publication of the first Raman spectrum was in 1928, work for which he was awarded the Nobel Prize in 1930.[1] As the Raman scattering process is inefficient, the technique went many years without widespread application, as it necessitated intense light sources and very long acquisition times, on the order of days, due to poorly efficient detectors. The invention of the laser in 1960, along with the development of more efficient optical detectors, led to the development and application of Raman spectroscopy to many diverse fields.[2] Further discovery of the high Raman signal on roughened metal surfaces in the 1970's led to further applications in surface-enhanced Raman spectroscopy (SERS) and beyond.[3-5] The combination of Raman spectroscopy with microscopy, started in the 1980's, led to many new fields of application that benefitted from better spatial resolution. The combination with confocal microscopy allowed for chemical analysis on the microscale level, while the later combination with tip-enhanced spectroscopy allowed for sub-10 nm resolution.[6,7]

Raman spectroscopy, widely used to identify the vibrational fingerprint of a molecule, is a vibrational spectroscopic technique based on the analysis of the energy of scattered

photons. Raman spectroscopy can reveal details of the structure, symmetry, bonding and electronic environment of molecules, and has found applications in fields as diverse as art analysis,[8,9] forensic science[10,11] and biomedicine.[12,13] When a molecule is illuminated by light that does not match the energy of an electronic transition, the light is scattered (Figure 2.1). Elastically scattered, or Rayleigh scattered, light exhibits no change in wavelength. Inelastic scattering, or Raman scattering, can be experimentally detected at both a lower energy, therefore longer wavelength, relative to the incident light source (Stokes scattering), or higher energy (shorter wavelength; anti-Stokes scattering). The relative population of these two inelastic scattering pathways can be described by the Boltzmann distribution, shown in Equation 2.1, that Stokes scattering is much more prevalent than anti-Stokes scattering at room temperature.[14]

$$\frac{I_S}{I_{AS}} = \frac{(\tilde{v}_i - \tilde{v}_{vib})^4}{(\tilde{v}_i + \tilde{v}_{vib})^4} e^{(\frac{hc\tilde{v}_{vib}}{k_b T})} \tag{2.1}$$

Here, I_S and I_{AS} represent the intensities of the Stokes and anti-Stokes scattering, respectively; $\tilde{v}_i$ and $\tilde{v}_{vib}$ represent the frequency of the incident light and the frequency of the vibration of the molecule, respectively; h is Planck's constant; c is the speed of light; k_b is the Boltzmann constant; and T is the temperature.
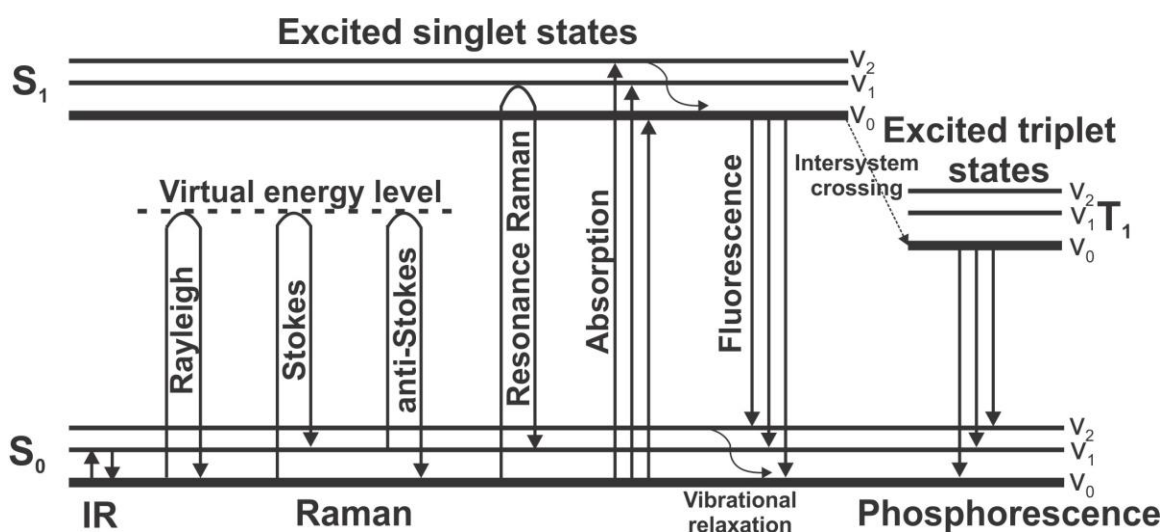
Figure 2-1 Jablonski diagram showing depicting different light-matter interactions

Only molecular vibrations that involve a change in the polarizability α will be visible in the Raman spectrum; the selection rule is:[15]

$$\frac{\partial \boldsymbol{\alpha}}{\partial \boldsymbol{q}} \neq 0 \qquad\qquad (2.2)$$

where $\boldsymbol{q}$ is the normal coordinate of the molecule. The polarizability of a molecule is the ease with which an electric field can distort the electron cloud of the molecule: in highly polarizable species, a dipole is easily induced by a local electric field. For a linear process such as Raman spectroscopy, the polarizability is mathematically represented by a second-rank tensor, with nine elements, at least one of which needs to vary with the molecular vibration in order for the vibration to be Raman active. In crystalline materials, with known symmetry, character tables relate the symmetry elements and Raman activity of vibrational modes. The symmetry of different Raman-active modes can be revealed through the use of polarized light in Raman spectroscopy by rotating the polarization of the incident beam and the analyzer.[16]

Raman scattering suffers from a very low quantum efficiency, such that only about 1 in 10^8 photons will promote a molecule to an excited virtual state such that it will decay to an excited upper vibrational state.[2,17] The low efficiency of this process generally yields a poor signal-to-noise ratio, necessitating the use of long acquisition times and higher laser powers in experiments. This can be improved upon through the exploitation of the plasmon resonances of nanostructured metal, which is the main enhancement factor in surface-enhanced Raman spectroscopy. Furthermore, signal enhancement can be combined with greater spatial resolution through the use of a nanoscale metal tip, in the application of tip-enhanced Raman spectroscopy (TERS). When combined with electronic resonances, such as those observed in dye molecules like crystal violet and Prussian blue, the signal can be further increased by three to four orders of magnitude.[18,19]

2.2 Plasmon Resonances in Nanostructured Metal

Plasmonics is a field involving the use of conductive nanostructures to convert light into localized electric fields; this is made possible by the strong interaction between the

incident light and the free conduction electrons of the conductive surface, which is often a metal such as Al, Au or Ag. Other conductive materials like graphene have been marginally exploited for surface enhancement.[20,21] Alteration of the metallic surface through the creation of micro- or nanoscale features allows for the tuning of this interaction on a nanoscale level, optimizing the confinement of the light.[22,23] Many applications based on such interactions are under development for sensing applications,[24,25] faster opto-electronic circuitry,[26] enhanced photovoltaic effect for the next generation of solar cells,[27] and for plasmon-mediated reactions.[28,29]

2.2.1 Plasmons

Electromagnetic radiation, such as light, can interact with metallic structures to excite the oscillation of the free conduction electrons of the metal out of phase relative to the incident electromagnetic radiation. This collective oscillation of the conduction electron is referred to as a plasmon. The frequency of oscillation of a bulk plasmon ω_p:[22]

$$\omega_p = \frac{1}{2\pi} \sqrt{\frac{n_e e^2}{m_e \varepsilon_0}} \qquad (2.3)$$

where n_e is the electron density, e is the elementary charge, m_e is the effective mass of the electron, and ε_0 is the permittivity of free space.

2.2.2 Surface Plasmons

When confined to the interface between a metal and a dielectric, plasmons are classified as surface plasmons (SP). A surface plasmon is a term that refers to the collective oscillation of the electron density at the surface, driven by the oscillating field of the incident light. The generation of these surface charges requires an electric field normal to the interface (Figure 2-2). When also considering the electromagnetic field induced in the dielectric medium, the term "surface plasmon polariton" is used; when it is further confined on a nanostructure smaller than the wavelength of the incident light, it is called a localized surface plasmon (LSP).[30] Figure 2.2 depicts the charge motion and resultant electromagnetic field associated with a surface plasmon polariton. Crucially, an

evanescent electric field is established in the dielectric medium, decaying exponentially with distance from the metal-dielectric interface.
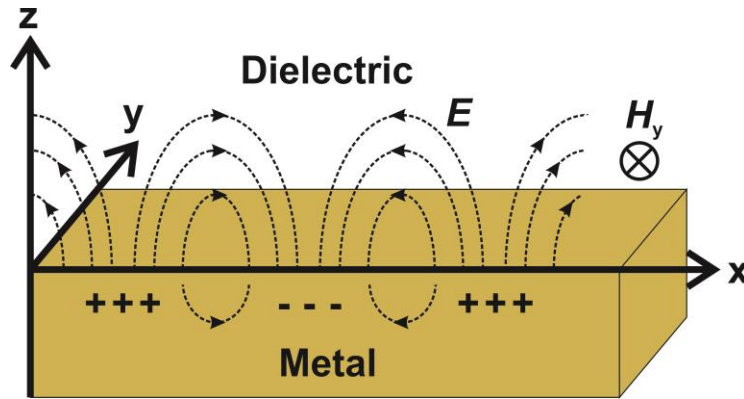
Figure 2-2 Charge motion on a metal surface due to a surface plasmon, and the induced electromagnetic field

In most instances, the establishment of a surface plasmon at the surface of a material requires that the dielectric function of the material has a negative real component and a positive imaginary component. The relationship between the dielectric constant of the metal ε_m and the plasmon frequency ω_p is given by:[22]

$$\varepsilon_m = 1 - \frac{\omega_p^2}{\omega^2} \qquad (2.4)$$

where ω is the frequency of the incident light. This is satisfied when $|\omega| < |\omega_p|$. These conditions are most commonly satisfied by coinage metals, though other metals such as Pt and Al can exhibit these conditions. The dielectric constant of metals can be calculated from the Drude-Lorentz model, and is shown for Ag, Au, Cu and Al in Figure 2.3.[31]
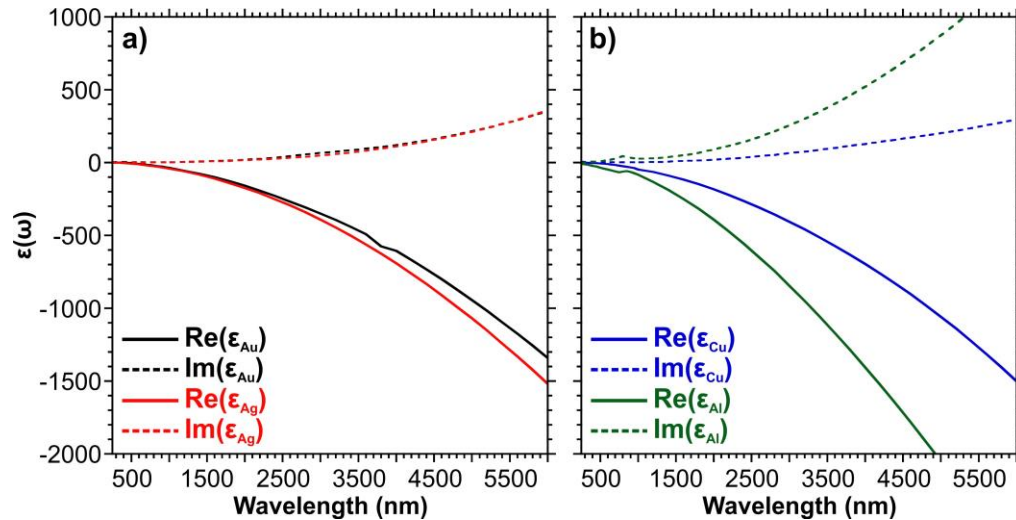
Figure 2-3 Complex dielectric constants a) gold and silver and b) copper and aluminum, as calculated by the Drude-Lorentz model.

2.2.3 Localized Surface Plasmon Resonance

A localized surface plasmon occurs when a surface plasmon is confined to an isolated nanostructure smaller than the wavelength of the incident light in all dimensions, usually by about an order of magnitude. Plasmon resonances may propagate in nanomaterials with at least one non-nanoscale dimension, such as in nanowires. In localized surface plasmon resonances (LSPR), incident light will incite the free electrons of the metal nanostructure to oscillate collectively with respect to the incident electric field, creating a charge accumulation at the surface.[22,32] This leads to a large enhancement in the local electric field, known as "hotspots" (Figure 2-4). This effect is further enhanced when nanostructures are adjacent, as small gaps allow neighbouring hotspots to couple, and is strongest at sharp points, where charge accumulates easily.
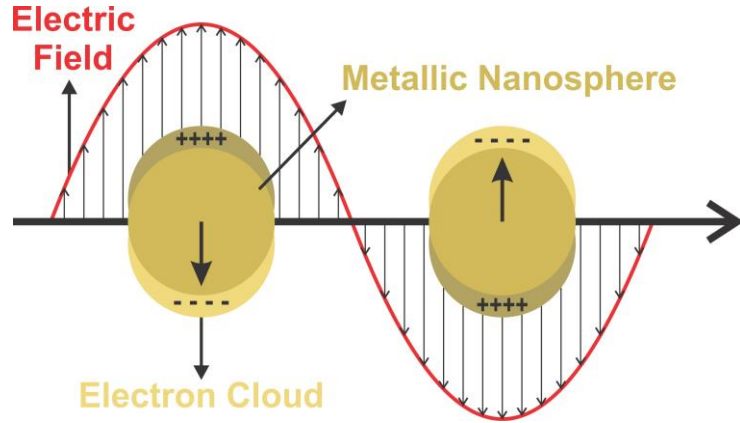
Figure 2-4 Oscillating charge and the induced electric field of a localized surface plasmon resonance

The spectral position of a localized surface plasmon resonance mode can be calculated using Mie theory, which provides the analytical solution to Maxwell's equations for the extinction (σ_{ext}), scattering (σ_{scat}) and absorption (σ_{abs}) coefficients, approximated for a small nanosphere:[22]

$$\sigma_{ext} = \frac{18\pi\varepsilon_d^{\frac{3}{2}}V}{\lambda} \times \frac{Im(\varepsilon_m)}{[Re(\varepsilon_m) + \chi\varepsilon_d]^2 + [Im(\varepsilon_m)]^2} \qquad (\mathbf{2.5})$$

$$\sigma_{scat} = \frac{32\pi^4\varepsilon_d^2V^2}{\lambda^4} \times \frac{[Re(\varepsilon_m) - \varepsilon_d]^2 + [Im(\varepsilon_m)]^2}{[Re(\varepsilon_m) + \chi\varepsilon_d]^2 + [Im(\varepsilon_m)]^2} \qquad (\mathbf{2.6})$$

$$\sigma_{abs} = \sigma_{ext} - \sigma_{scat} \qquad (\mathbf{2.7})$$

Here, ε_d and ε_m are the dielectric constants of the surrounding medium and the metal, respectively; λ is the incident wavelength; χ is shape factor and V is the volume of the nanoparticle. These localized surface plasmon modes allow for the control of light on the nanometer regime, limited primarily by the dimensions of the metal nanostructure supporting these modes. As shown in equations 2.4 – 2.6, the metal composition, size, dielectric environment, as well as shape of a nanoparticle determines the light-matter interaction, including absorption and scattering processes, the number of plasmon modes and their respective frequencies. For anisotropic nanomaterials, no analytical solution to Maxwell's equations exists, and thus LSPR modes are determined through semi-

empirical calculations. The field of plasmonics involves the tuning of these modes by changing the metal, shape, size, and spacing of these nanoparticles, and exploiting the resultant electromagnetic fields for applications in spectroscopy, biomedicine, and solar cells, among many other diverse fields.[30]

2.3 Surface-Enhanced Raman Spectroscopy

As previously discussed, the probability of an incident photon scattering inelastically in the Raman process is very low. The localized electric field enhancement that is the result of localized surface plasmon resonance can be applied as a remedy to the low quantum efficiency of the Raman scattering process. This was first seen experimentally by Fleischmann *et al.* in 1974, with the observation of an anomalously strong Raman signal of pyridine adsorbed on a roughened silver electrode.[4] Further work by the groups of Van Duyne and Creighton in 1977 determined the nature of the enhancement, giving rise to the new field of surface-enhanced spectroscopies.[3,5] Such techniques developed include are surface-enhanced Raman spectroscopy (SERS), surface-enhanced infrared absorption (SEIRA), and tip-enhanced Raman spectroscopy (TERS), which involves the application of the SERS mechanism to highly spatially resolved surface Raman measurements.[4,6,33]

Inarguably, the most common technique exploiting this electromagnetic field enhancement is surface-enhanced Raman spectroscopy. SERS is a technique that relies on a molecule of interest being in close proximity or adsorbed onto the surface of a metallic nanostructure or rough metallic surface. In the initial SERS studies, rough metallic surfaces, obtained by electrochemical roughening or mechanical alterations, were the most common material used as active platforms. In the decades since, the advent of advanced nanofabrication technologies has allowed the development of more efficient SERS platforms, with improved reproducibility and precise control over shape and size. Such technologies have allowed for analytical signal detection down to the single molecule level.[34,35] The enhancement of the Raman signal varies between nanostructures, with most reported enhancement factors lying in a range of 10^4-10^7. More recently, SERS studies have highlighted that two mechanisms must be accounted

for in the enhancement of the Raman signal: electromagnetic enhancement and chemical enhancement.

2.3.1 Electromagnetic Enhancement Mechanism

Electromagnetic enhancement is the dominant enhancement mechanism in SERS, with a typical signal increase of $10^4 – 10^6$ over the normal Raman spectrum.[36-38] The electromagnetic enhancement is a result of the LSPR of the metallic nanostructure. The degree of enhancement depends on the plasmonic properties of the metal nanostructure, which are affected by the size and shape of the metal particles, as well as the interparticle distance and the polarization of the excitation source.[23,32] Despite this local EM field increase, the intensity of this electric field decays exponentially with distance from the metal surface, which classifies SERS as a surface-specific technique. Generally, the region of enhancement is limited to several nanometres from the surface of the metallic nanostructure;[39] hotspots as small as 0.4 nm have been observed.[40]

Sharp metallic plasmonic nanostructures act as optical nanoantennae, converting freely propagating optical radiation into localized hotspots of electromagnetic field enhancement. When a molecule of interest is located in the vicinity of this nanoantenna, both incident light and Raman scattered light are enhanced. Due to this, the enhancement factor (EF) of the SERS signal over the Raman signal follows the equation:[22]

$$EF = \frac{|E_{LSPR}|^2 |E'_{LSPR}|^2}{|E_0|^4} \qquad (2.8)$$

where E_0 is the incident electric field, E_{LSPR} is the electric field outside the metal nanoparticle at the frequency of the incident light, and E'_{LSPR} is the field at the frequency of the Raman scattering. Therefore, the maximum enhancement of the signal is achieved when both the incident laser and the Raman scattered light are close in frequency to that of the LSPR mode. The electromagnetic enhancement mechanism is the dominant mechanism in SERS; however, it fails to account for the entire enhancement observed experimentally. In order to explain the other instances of SERS enhancement, the chemical enhancement mechanism must be introduced.

2.3.2 Chemical Enhancement Mechanism

Chemical enhancement that is intrinsic to SERS involves the interaction between the adsorbate and the metal structure. Chemical enhancement can be due to charge transfer or changes in the electronic properties of the molecule due to adsorption. A charge transfer occurs when the applied field is in resonance with an electron transition occurring between the molecule and the metal. Such charge transfers will change the polarizability of a molecule, thus changing its Raman scattering cross-section.[41] This chemical enhancement typically accounts for 10^2-10^3 of the total enhancement of the SERS process.[37,42,43] Chemical enhancement due to resonance occurs when the incident laser energy matches an allowed electronic transition of the adsorbed molecule; this is described as surface-enhanced resonance Raman spectroscopy (SERRS).[41,44] Non-resonant chemical enhancement can occur, as adsorption onto the metal often changes the energy levels of a molecule, changing its Raman cross-section.[45,46] The degree of non-resonant chemical enhancement is dependent upon the size, charge, binding site and orientation of the molecule, as well as the molecule-metal separation.[45] As this enhancement mechanism is dependent upon the molecule of interest, it is much more common to optimize the SERS signal by exploiting the electromagnetic enhancement mechanism. This is done experimentally by changing the opto-geometric properties of the metallic nanostructure in question, rather than changing the molecule of interest.

2.4 Diffraction Limit in Optical Microscopy

In optical measurements, the lateral spatial resolution is limited by diffraction. This can be understood through the interferences of Airy patterns, which describe the distribution of light intensity of an optimally focused beam by a perfect lens with a circular apex. The Airy diffraction pattern follows the equation:[47]

$$ I = I_0 \left[\frac{2J_1(x)}{x} \right]^2 \qquad (\mathbf{2.9}) $$

such that the maximum intensity is I_0, $J_1(x)$ is the Bessel function of the first kind of order one, and x is the distance from the centre of the pattern. The Airy diffraction pattern is a bright area in the middle, of maximum intensity, and a series of concentric bright rings,

as shown in Figure 2.5. The minimum distance at which adjacent patterns can be resolved is such that the first minimum of one pattern is aligned with the maximum of the adjacent one.
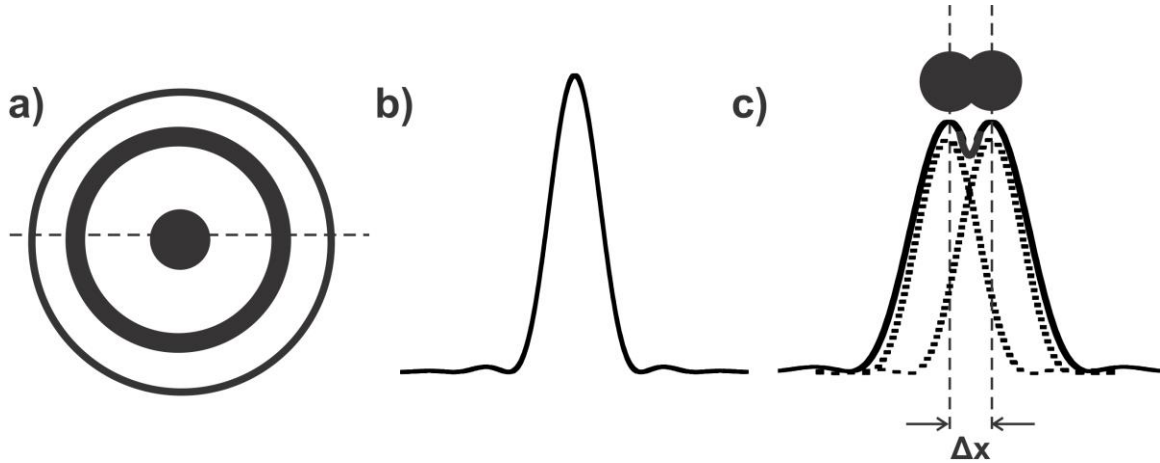
Figure 2-5 a) Top view of an Airy diffraction pattern, with a dotted line indicating the side view b); c) Overlap of two Airy diffraction patterns, showing the minimum resolvable distance *Δx*

This minimum resolvable distance *Δx* is given by the Rayleigh criterion:[48]

$$\Delta x = \frac{1.22\lambda}{2n \sin \alpha_r} \tag{2.10}$$

for an incident wave of wavelength λ travelling in a medium of refractive index n with a half-angle α_r. The value $n \sin \alpha$ is a property of the objective, and is defined as the numerical aperture (NA). In ideal experimental conditions, using an objective with a high NA, this limit reaches several hundreds of nanometres, too large to probe materials on the nanoscale (i.e. with at least one dimension less than 100 nm). Therefore, recent developments in optical microscopy have been focused on surpassing this diffraction limit.[48,49] One such method is achieved through accessing the optical near-field of the system. In this regime, less than one wavelength from the surface, evanescent waves that contain nanoscale details propagate; however, these waves cannot be detected directly, as they decay exponentially with distance from the sample.[50]

Despite its high sensitivity, surface-enhanced Raman spectroscopy is restricted by the diffraction limit of light; for this reason, tip-enhanced Raman spectroscopy was developed. In tip-enhanced Raman spectroscopy, high spatial resolution is achieved by accessing the optical near-field of the sample by using a metallic probe, which mimics a single particle probing the surface.

2.5   Tip-Enhanced Raman Spectroscopy

In surface-enhanced Raman spectroscopy (SERS), an enhancement of typically several orders of magnitude (10^6 - 10^8) is achieved by placing the analyte on a roughened metal film, metallic nanostructures, or in a colloidal solution of metal nanoparticles. However, such measurements are still limited in spatial resolution: optical diffraction limits the applicability of SERS to objects on the order of several hundred nanometres in size, or larger. For this reason, the principles of SERS have been extended to develop tip-enhanced Raman spectroscopy (TERS), first experimentally reported in 2000.[6,51,52]

Tip-enhanced Raman spectroscopy involves a controlled interaction between a sharp metallic tip, as shown in Figure 2-6a, and a sample, and the collection of the Raman signal resulting from the scattering of the tip. TERS offers both an enhanced signal and spatial resolution beyond the diffraction limit of light. The TERS tip serves two functions: first, it acts as an optical nanoantenna that confines the local electric field in its vicinity (Figure 2-6b); secondly, in scanning the surface, the tip acts as a perturbing element, interacting with evanescent waves confined at the surface of the sample.[50] These evanescent waves, that contain the small spatial details of the sample, are converted into propagating waves by the metallic tip. This is the reciprocity theorem of light: if a propagating wave can be partly transformed into an evanescent wave, then an evanescent wave can be transformed into a propagating wave. These propagating waves are then detectable in the far-field by a conventional detector.[53] Enhancement occurs via the lightning rod effect and electromagnetic enhancement. The lightning rod effect occurs as charge accumulates in the sharp corners of metallic structures.[54,55] The electromagnetic mechanism is based on the LSPR of the tip, also contributing to a charge accumulation at the tip apex. This leads to a strongly localized electromagnetic field at the apex, enhancing the TERS signal.
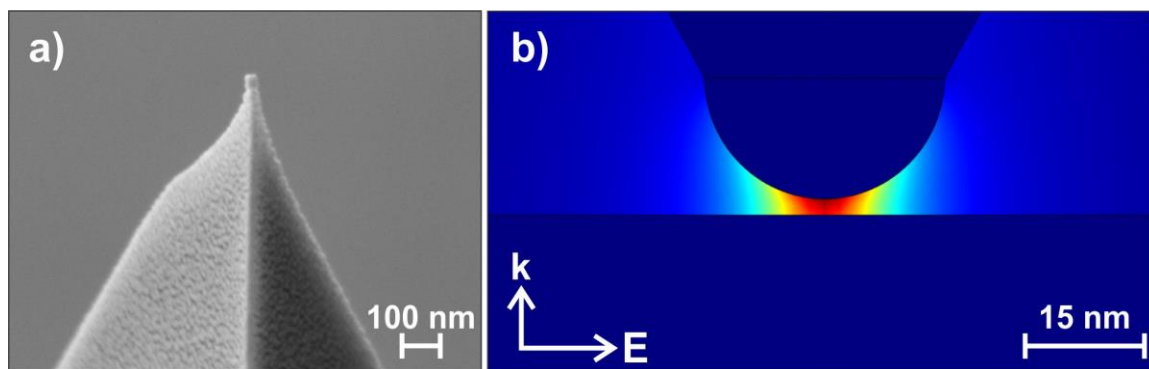
Figure 2-6 a) Scattering electron micrograph of a gold-coated TERS tip; b) Simulation of the confined electric field around the gold TERS tip.

As for SERS, the LSPR effect is the main driving source of enhancement. Many factors can influence the electromagnetic enhancement, including the tip geometry, the substrate, the laser polarization and the surrounding medium. Enhancement is optimal when the laser wavelength spectrally matches the LSPR of the TERS tip and when the incident beam has a polarization component along the tip axis.[56,57] The tip must be sufficiently close to the substrate (< 5 nm) to see enhancement, and a stronger enhancement is seen when the tip is coupled with a noble metal substrate. The LSPR of the TERS system is affected by the material of the tip and the surrounding medium. The spatial resolution of TERS is generally limited by the tip apex; however, resolution of dimensions smaller than the apex of the tip has been achieved, and attributed to smaller protrusions or nanocavities.[55,58,59]

2.6   Plasmon Decay

As discussed, the field of plasmonics has largely involved exploiting the localized surface plasmon resonance of metal nanoparticles for plasmon-enhanced spectroscopies, such as SERS and TERS. In addition to this, the byproduct of these resonances, the generation of hot carriers and local heating, have been exploited for applications such as photothermal therapy and catalyzing chemical reactions.[28,60-62]

2.6.1 Hot Carrier Generation

The illumination of a metal structure or surface can lead to many complex processes, such as the generation of strong optical fields via surface plasmons; the ejection, or fast internal relaxation, of hot electron-hole pairs; or the emission of a photon. The latter comprises the radiative decay pathway of the plasmon resonance. Non-radiative decay consists of Landau damping, a quantum mechanical process where a plasmon is transferred to an electron-hole pair; this occurs on a timescale of 1 -100 fs.[63,64] The branching ratio of radiative to non-radiative decay depends on the geometry and composition of the nanostructure. Landau damping is related to the imaginary component of the dielectric function of a material $Im(\varepsilon_m)$ such that a plasmon resonance at a wavelength corresponding to a larger $Im(\varepsilon_m)$ of the metal results in a higher generation of hot carriers.[65] Mie theory predicts that radiative decay follows R^6, where R is the radius of a small nanosphere, while non-radiative decay follows R^3;[66] therefore, smaller nanoparticles produce more hot carriers, but also have a lower electromagnetic field strength, as their LSPRs decay through hot carrier generation.[67] The combination of high field strength and high generation of hot carriers is achieved through the fabrication of arrays of plasmonic nanostructures.

The distribution of carriers in a material is a function of plasmon energy, particle size, and the electronic structure and density of states of the material. Hot carriers are preferentially emitted from regions of high electromagnetic field, such as in plasmonic hotspots, and then accelerated by evanescent fields. In this way, they are steered by the geometry of the nanostructure.[28,29]

Coinage metals, typical materials for applications in plasmonics, are characterized by a filled valence d-band, and a diffuse band of hybridized s and p states (sp-band), reaching both above and below the Fermi energy (E_F), as seen in Figure 2-7a. The sp-band has a near-constant density of states, which is lower than that of the d-band.[65] When illuminated by a photon of an energy less than the difference between the d-band and E_F, that is, the interband transition threshold, phonons and intraband transitions between sp-band states are excited (Figure 2-7b). The probability of a plasmon-derived charge carrier in this energy window [$E_F - h\nu$, $E_F + h\nu$] is approximately constant, due to the

relatively constant density of states of the sp-band. Above this interband transition threshold, plasmons decay through the excitation of interband transitions (Figure 2-7c). As a result, the plasmon-derived hot carriers above this threshold are mainly hot holes.[65,68]
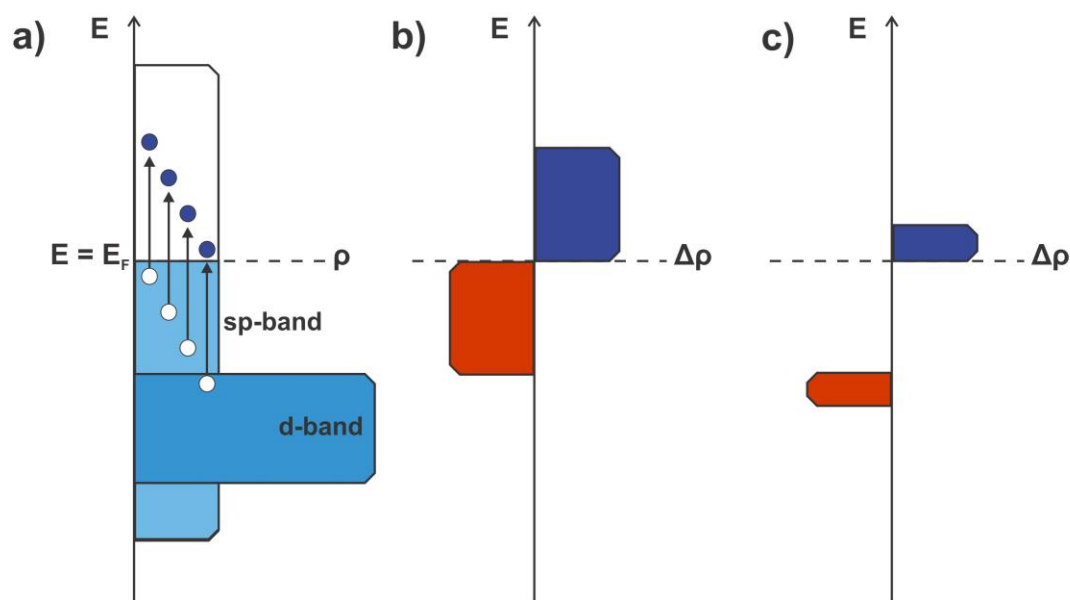
Figure 2-7 a) Density of states of Ag, showing allowed electronic transitions; Hot carrier distribution in Ag, involving hot holes (red) and hot electrons (blue) at excitation b) below and c) above the interband threshold. Here, ρ is the density of electronic states, and Δρ is the change in density following electronic excitation.

2.6.2 Heating Effects

After the hot electron-hole pairs are excited by Landau damping of the plasmon resonance, their energy is averaged through electron-electron and hole-hole interactions. This occurs in femtoseconds after the excitation of the hot carriers. The population of the electronic states resembles a Fermi-Dirac-like distribution, characterized by a high temperature T_{el}. In the following picoseconds, the lower energy electrons and holes will experience more interactions with phonons, such that their excess energy is thermalized through electron-phonon or hole-phonon interactions. The lattice temperature and electron temperature T_{el} equilibrate over several picoseconds. Finally, the temperature equilibrates with the surroundings. [64] This process is summarized in Figure 2-8. Current

research involves decoupling the contributions of hot carrier generation and the local increase in temperature to the increased reaction rate of plasmon-mediated reactions.[69,70] Such heating can reach over a hundred K under continuous wave laser irradiation;[71,72] heating as high as 650 K has been measured by Raman thermometry.[73]
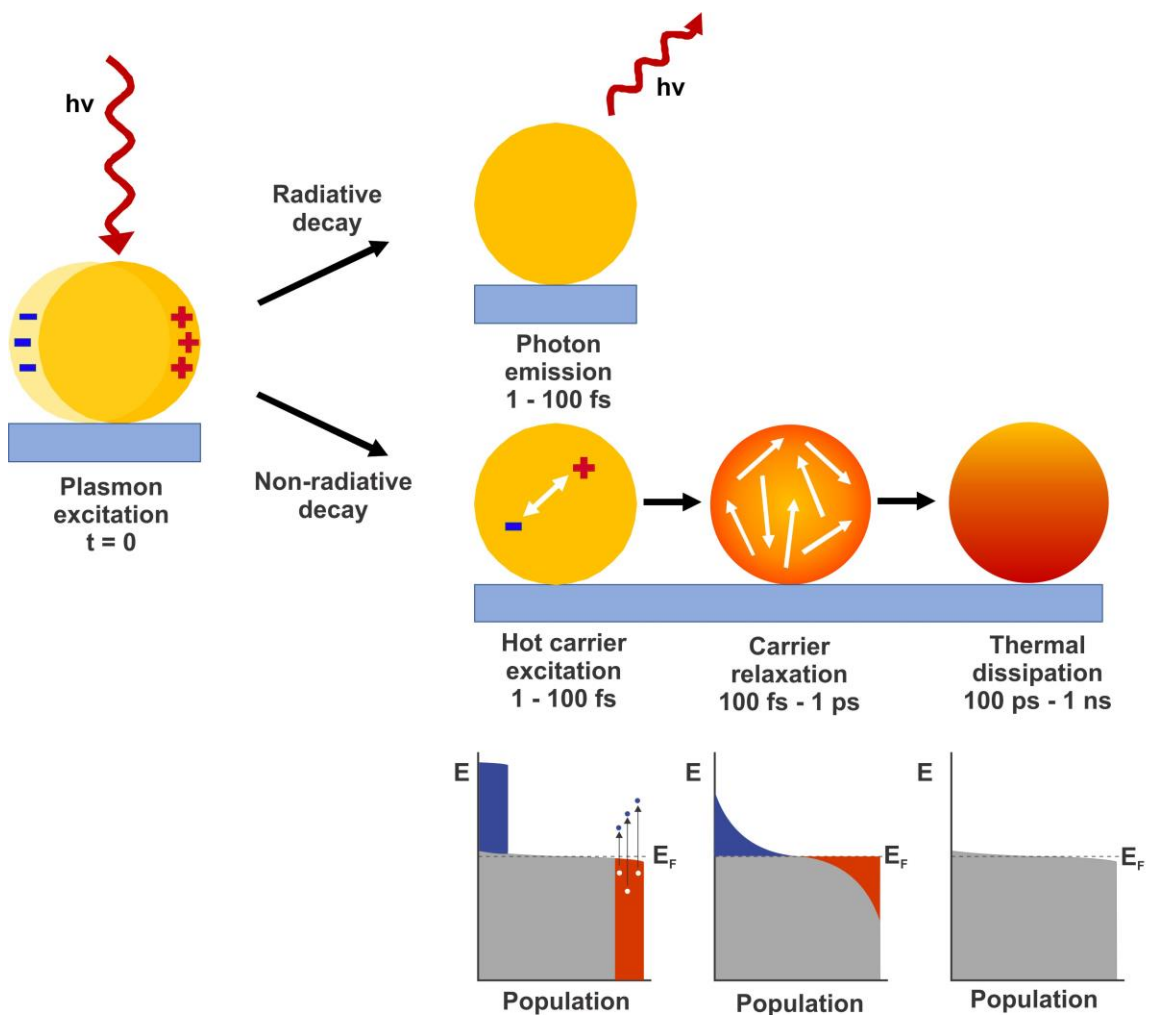
Figure 2-8 Decay process following plasmon excitation at t = 0, including the corresponding density of electronic states, with hot holes depicted in red, hot electrons in blue.

2.6.3 Coupling to Chemical Reactions

When a molecule is adsorbed on the surface of the metal nanoparticle, hot electrons can transfer to the molecule by one of two mechanisms: i) indirectly, through the excitation

of hot electrons in the metal nanostructure, which eventually get transferred to the molecule, or ii) directly, where plasmons decay by exciting an electron from the metal to the molecule. The Menzel-Gomer-Redhead model describes the indirect hot electron transfer.[74,75] In the model, a hot electron approaches the surface of a metal nanoparticle, where a molecule is adsorbed. The electron can transiently localize in an unpopulated metal-adsorbate state, which then equilibrates to an excited state of the metal-adsorbate system. In this excited state, bond lengths differ from their equilibrium positions; therefore, the nuclei move to attain equilibrium again. These vibrations help overcome the activation barrier for the reaction. Due to the high number of unpopulated metal electronic states near the Fermi energy, the decay of the electron in this metal-adsorbate state is very probable, leading to a lifetime of this state to several femtoseconds.[65]

In contrast to Landau damping (Figure 2-9a), wherein hot electrons are excited inside a metal, chemical interface damping involves plasmons decaying directly into an interfacial charge transfer state, involving no hot carrier transfer in the metal (Figure 2-9b). As this mechanism avoids the loss of energy to electron scattering interactions, it is much more efficient; however, as the efficiency of the decay pathway is increased, the plasmon lifetime is decreased, resulting in a lower localized electric field.[67,76] For use in applications such as photovoltaics, a balance is struck between the energy of the plasmon and the efficiency of the charge transfer by changing the geometry and size of the metal nanoparticles.[77]
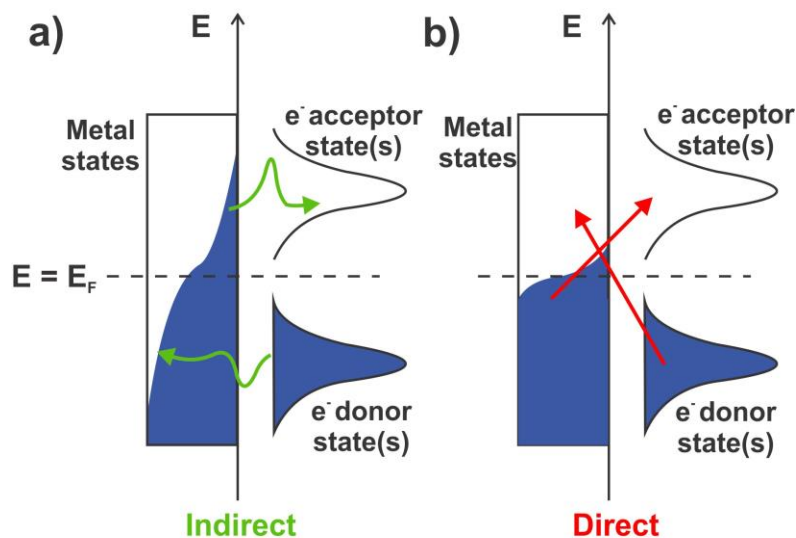
Figure 2-9 Hot carriers transferred to an adsorbate a) indirectly, by Landau damping, involving the excitation of a hot electron-hole pair in the metal, and b) directly, by chemical interface damping, where an interfacial electronic transition separates the hot electron and hole.

2.7   Summary

In this chapter, the principles of plasmonics and its application to Raman spectroscopy was reviewed. In short, Raman spectroscopy involves the inelastic scattering of light by molecular vibrations. This is an inefficient process, necessitating large sample volumes, high laser powers and long acquisition times. In a localized surface plasmon resonance, the electric field around a metal nanoparticle is locally enhanced, creating nanoscale hotspots of intense electric field. The degree of this enhancement depends on the size, shape, chemical composition, and surroundings of the metal nanoparticle, as well as interparticle spacing. These hotspots are used to increase the poor efficiency of Raman scattering, leading to surface-enhanced Raman spectroscopy. In surface-enhanced Raman spectroscopy, the spatial resolution of measurements is limited by optical diffraction. This physical limit led to the development of tip-enhanced Raman spectroscopy, where metal nanoprobe is used to both enhance the local electric field and perturb the evanescent fields in the near-field, converting them to propagating waves detectable in the far-field, thus overcoming the diffraction limit. Lastly, the dynamic

behavior of plasmon decay is discussed, as the resultant hot carriers and local heating can be coupled to molecules adsorbed on the surface of the metal nanoparticle, triggering chemical reactions. Chemical reactions of societal interest, such as the splitting of water (for hydrogen production) or CO_2 reduction, are presently investigated with the goal of using plasmon-mediated reactions using sunlight.

2.8 References

1. Raman, C. V.; Krishnan, K. S. *Nature* **1928**, *121*, 501-502.

2. McCreery, R. L. In *Raman Spectroscopy for Chemical Analysis*; John Wiley & Sons, Inc.: **2000**, p 1-14.

3. Albrecht, M. G.; Creighton, J. A. *J. Am. Chem. Soc.* **1977**, *99*, 5215-5217.

4. Fleischmann, M.; Hendra, P. J.; McQuillan, A. J. *Chem. Phys. Lett.* **1974**, *26*, 163-166.

5. Jeanmaire, D. L.; Van Duyne, R. P. *J. Electroanal. Chem.* **1977**, *84*, 1-20.

6. Hayazawa, N.; Inouye, Y.; Sekkat, Z.; Kawata, S. *Opt. Commun.* **2000**, *183*, 333-336.

7. Opilik, L.; Schmid, T.; Zenobi, R. *Annu. Rev. Anal. Chem.* **2013**, *6*, 379-398.

8. Bersani, D.; Conti, C.; Matousek, P.; Pozzi, F.; Vandenabeele, P. *Anal. Methods* **2016**, *8*, 8395-8409.

9. Leona, M. *Proc. Natl. Acad. Sci. U.S.A.* **2009**, *106*, 14757-14762.

10. Doty, K. C.; Lednev, I. K. *Trends Anal. Chem.* **2018**, *103*, 215-222.

11. Menżyk, A.; Damin, A.; Martyna, A.; Alladio, E.; Vincenti, M.; Martra, G.; Zadora, G. *Talanta* **2020**, *209*, 120565.

12. Ember, K. J. I.; Hoeve, M. A.; McAughtrie, S. L.; Bergholt, M. S.; Dwyer, B. J.; Stevens, M. M.; Faulds, K.; Forbes, S. J.; Campbell, C. J. *NPJ Regen. Med.* **2017**, *2*, 12.

13. Antonio, K. A.; Schultz, Z. D. *Anal. Chem.* **2014**, *86*, 30-46.

14. Ornstein, L. S.; Rekveld, J.; Utrecht. *Phys. Rev.* **1929**, *34*, 720-725.

15. McCreery, R. L. In *Raman Spectroscopy for Chemical Analysis* **2000**, p 15-33.

16. Kiefer, J.; Kaspereit, M. *Anal. Methods* **2013**, *5*, 797-800.

17. Petry, R.; Schmitt, M.; Popp, J. *ChemPhysChem* **2003**, *4*, 14-30.

18. Fateixa, S.; Nogueira, H. I. S.; Trindade, T. *ACS Omega* **2018**, *3*, 4331-4341.

19. Yin, Y.; Li, Q.; Ma, S.; Liu, H.; Dong, B.; Yang, J.; Liu, D. *Anal. Chem.* **2017**, *89*, 1551-1557.

20. Shi, H.; Zhao, B.; Ma, J.; Bronson Jr, M. J.; Cai, Z.; Chen, J.; Wang, Y.; Cronin, M.; Jensen, L.; Cronin, S. B. *ACS Appl. Mater. Interfaces* **2019**, *11*, 36252-36258.

21. Silver, A.; Kitadai, H.; Liu, H.; Granzier-Nakajima, T.; Terrones, M.; Ling, X.; Huang, S. *Nanomaterials* **2019**, *9*, 516.

22. Mayer, K. M.; Hafner, J. H. *Chem. Rev.* **2011**, *111*, 3828-3857.

23. Lu, X.; Rycenga, M.; Skrabalak, S. E.; Wiley, B.; Xia, Y. *Annu. Rev. Phys. Chem.* **2009**, *60*, 167-192.

24. Chou, A.; Jaatinen, E.; Buividas, R.; Seniutinas, G.; Juodkazis, S.; Izake, E. L.; Fredericks, P. M. *Nanoscale* **2012**, *4*, 7419-7424.

25. Oroval, M.; Coronado-Puchau, M.; Langer, J.; Sanz-Ortiz, M. N.; Ribes, Á.; Aznar, E.; Coll, C.; Marcos, M. D.; Sancenón, F.; Liz-Marzán, L. M.; Martínez-Máñez, R. *Chem. Eur. J.* **2016**, *22*, 13488-13495.

26. Fang, Y.; Sun, M. *Light: Science & Applications* **2015**, *4*, e294-e294.

27. Jang, Y. H.; Jang, Y. J.; Kim, S.; Quan, L. N.; Chung, K.; Kim, D. H. *Chem. Rev.* **2016**, *116*, 14982-15034.

28. Nguyen, V.-Q.; Ai, Y.; Martin, P.; Lacroix, J.-C. *ACS Omega* **2017**, *2*, 1947-1955.

29. Nguyen, M.; Kherbouche, I.; Gam-Derouich, S.; Ragheb, I.; Lau-Truong, S.; Lamouri, A.; Lévi, G.; Aubard, J.; Decorse, P.; Félidj, N.; Mangeney, C. *Chem. Commun.* **2017**, *53*, 11364-11367.

30. Jiang, N.; Zhuo, X.; Wang, J. *Chem. Rev.* **2018**, *118*, 3054-3099.

31. Barchiesi, D.; Grosges, T. *J. Nanophotonics* **2014**, *8*, 083097.

32. Rycenga, M.; Cobley, C. M.; Zeng, J.; Li, W.; Moran, C. H.; Zhang, Q.; Qin, D.; Xia, Y. *Chem. Rev.* **2011**, *111*, 3669-3712.

33. Osawa, M.; Ataka, K.-I.; Yoshii, K.; Nishikawa, Y. *Appl. Spectrosc.* **1993**, *47*, 1497-1502.

34. Almehmadi, L. M.; Curley, S. M.; Tokranova, N. A.; Tenenbaum, S. A.; Lednev, I. K. *Sci. Rep.* **2019**, *9*, 12356.

35. Mao, P.; Liu, C.; Favraud, G.; Chen, Q.; Han, M.; Fratalocchi, A.; Zhang, S. *Nat. Commun.* **2018**, *9*, 5428.

36. Paul, A. M.; Fan, Z.; Sinha, S. S.; Shi, Y.; Le, L.; Bai, F.; Ray, P. C. *J. Phys. Chem. C* **2015**, *119*, 23669-23675.

37. Pramanik, A.; Gao, Y.; Gates, K.; Begum, S.; Ray, P. C. *ACS Omega* **2019**, *4*, 11112-11118.

38. Singh, A. K.; Khan, S. A.; Fan, Z.; Demeritte, T.; Senapati, D.; Kanchanapally, R.; Ray, P. C. *J. Am. Chem. Soc.* **2012**, *134*, 8662-8669.

39. Kumari, G.; Kandula, J.; Narayana, C. *J. Phys. Chem. C* **2015**, *119*, 20057-20064.

40. Joshi, G. K.; White, S. L.; Johnson, M. A.; Sardar, R.; Jain, P. K. *J. Phys. Chem. C* **2016**, *120*, 24973-24981.

41. Jensen, L.; Aikens, C. M.; Schatz, G. C. *Chem. Soc. Rev.* **2008**, *37*, 1061-1073.

42. Demeritte, T.; Viraka Nellore, B. P.; Kanchanapally, R.; Sinha, S. S.; Pramanik, A.; Chavva, S. R.; Ray, P. C. *ACS Appl. Mater. Interfaces* **2015**, *7*, 13693-13700.

43. Fan, Z.; Yust, B.; Nellore, B. P. V.; Sinha, S. S.; Kanchanapally, R.; Crouch, R. A.; Pramanik, A.; Chavva, S. R.; Sardar, D.; Ray, P. C. *J. Phys. Chem. Lett.* **2014**, *5*, 3216-3221.

44. Nicolson, F.; Jamieson, L. E.; Mabbott, S.; Plakas, K.; Shand, N. C.; Detty, M. R.; Graham, D.; Faulds, K. *Analyst* **2018**, *143*, 5965-5973.

45. Morton, S. M.; Ewusi-Annan, E.; Jensen, L. *Phys. Chem. Chem. Phys.* **2009**, *11*, 7424-7429.

46. Kim, J.; Jang, Y.; Kim, N.-J.; Kim, H.; Yi, G.-C.; Shin, Y.; Kim, M. H.; Yoon, S. *Front. Chem.* **2019**, *7*.

47. Abbe, E. *Archiv für Mikroskopische Anatomie* **1873**, *9*, 413-468.

48. Kawata, S.; Inouye, Y.; Verma, P. *Nat. Photonics* **2009**, *3*, 388-394.

49. Dedecker, P.; Hofkens, J.; Hotta, J.-i. *Mater. Today* **2008**, *11*, 12-21.

50. Hartschuh, A. *Angew. Chem. Int. Ed.* **2008**, *47*, 8178-8191.

51. Anderson, M. S. *Appl. Phys. Lett.* **2000**, *76*, 3130-3132.

52. Stöckle, R. M.; Suh, Y. D.; Deckert, V.; Zenobi, R. *Chem. Phys. Lett.* **2000**, *318*, 131-136.

53. Kawata, S. *Appl. Spectrosc.* **2013**, *67*, 117-125.

54. Asghari-Khiavi, M.; Wood, B. R.; Hojati-Talemi, P.; Downes, A.; McNaughton, D.; Mechler, A. *J. Raman Spectrosc.* **2012**, *43*, 173-180.

55. Urbieta, M.; Barbry, M.; Zhang, Y.; Koval, P.; Sánchez-Portal, D.; Zabala, N.; Aizpurua, J. *ACS Nano* **2018**, *12*, 585-595.

56. Kazemi-Zanjani, N.; Vedraine, S.; Lagugné-Labarthet, F. *Opt. Express* **2013**, *21*, 25271-25276.

57. Mino, T.; Saito, Y.; Verma, P. *ACS Nano* **2014**, *8*, 10187-10195.

58. Chen, X.; Liu, P.; Hu, Z.; Jensen, L. *Nat. Commun.* **2019**, *10*, 2567.

59. Trautmann, S.; Aizpurua, J.; Götz, I.; Undisz, A.; Dellith, J.; Schneidewind, H.; Rettenmayr, M.; Deckert, V. *Nanoscale* **2017**, *9*, 391-401.

60. Kim, M.; Lee, J.-H.; Nam, J.-M. *Adv. Sci.* **2019**, *6*, 1900471.

61. Ibarra, M. R.; Khlebtsov, N. G. *J. Appl. Phys.* **2019**, *126*, 170401.

62. Brooks, J. L.; Chulhai, D. V.; Yu, Z.; Goodpaster, J. D.; Frontiera, R. R. *J. Phys. Chem. C* **2019**, *123*, 29306-29313.

63. Li, X.; Xiao, D.; Zhang, Z. *New J. Phys.* **2013**, *15*, 023011.

64. Brongersma, M. L.; Halas, N. J.; Nordlander, P. *Nat. Nanotechnol.* **2015**, *10*, 25-34.

65. Christopher, P.; Moskovits, M. *Annu. Rev. Phys. Chem.* **2017**, *68*, 379-398.

66. Brus, L. *Acc. Chem. Res.* **2008**, *41*, 1742-1749.

67. Foerster, B.; Joplin, A.; Kaefer, K.; Celiksoy, S.; Link, S.; Sönnichsen, C. *ACS Nano* **2017**, *11*, 2886-2893.

68. Brown, A. M.; Sundararaman, R.; Narang, P.; Goddard, W. A.; Atwater, H. A. *ACS Nano* **2016**, *10*, 957-966.

69. Zhan, C.; Liu, B.-W.; Huang, Y.-F.; Hu, S.; Ren, B.; Moskovits, M.; Tian, Z.-Q. *Nat. Commun.* **2019**, *10*, 2671.

70. Yu, Y.; Sundaresan, V.; Willets, K. A. *J. Phys. Chem. C* **2018**, *122*, 5040-5048.

71. Liebig, F.; Sarhan, R. M.; Sander, M.; Koopman, W.; Schuetz, R.; Bargheer, M.; Koetz, J. *ACS Appl. Mater. Interfaces* **2017**, *9*, 20247-20253.

72. Baffou, G.; Polleux, J.; Rigneault, H.; Monneret, S. *J. Phys. Chem. C* **2014**, *118*, 4890-4898.

73. Boerigter, C.; Aslam, U.; Linic, S. *ACS Nano* **2016**, *10*, 6108-6115.

74. Menzel, D.; Gomer, R. *J. Chem. Phys.* **1964**, *41*, 3311-3328.

75. Redhead, P. A. *Can. J. Phys.* **1964**, *42*, 886-905.

76. Kale, M. J.; Christopher, P. *Science* **2015**, *349*, 587-588.

77. Besteiro, L. V.; Kong, X.-T.; Wang, Z.; Hartland, G.; Govorov, A. O. *ACS Photonics* **2017**, *4*, 2759-2781.

Chapter 3

3 Characterization and Fabrication of Plasmonic Platforms

As the appropriate potential applications of plasmonic nanoparticles and platforms depend heavily on its morphology and optical properties, several methods are necessary to characterize these nanoparticles to better understand the light-matter interaction. In this chapter, we describe the methods used in this work.

3.1 Visible-NIR and Mid-Infrared Absorption

Upon irradiation, the metallic nanoparticles will couple with the excitation light at specific wavelengths. Depending on their chemical nature, shape and size, the nanoparticles will scatter or absorb the incident light, the sum of which is probed by absorption spectroscopy. The absorption spectrum will reveal the optical resonances referred to as the plasmon resonances. Such knowledge is important to determine which wavelength to use in order to efficiently excite a plasmon of a nanostructure. Such absorption measurements were conducted in transmission through the samples deposited over a glass coverslip. The detected signal is compared to that of a blank coverslip, and the extinction spectrum is obtained by calculating their ratio. A diagram of the set-up for micro-absorption measurements is shown in Figure 3-1.
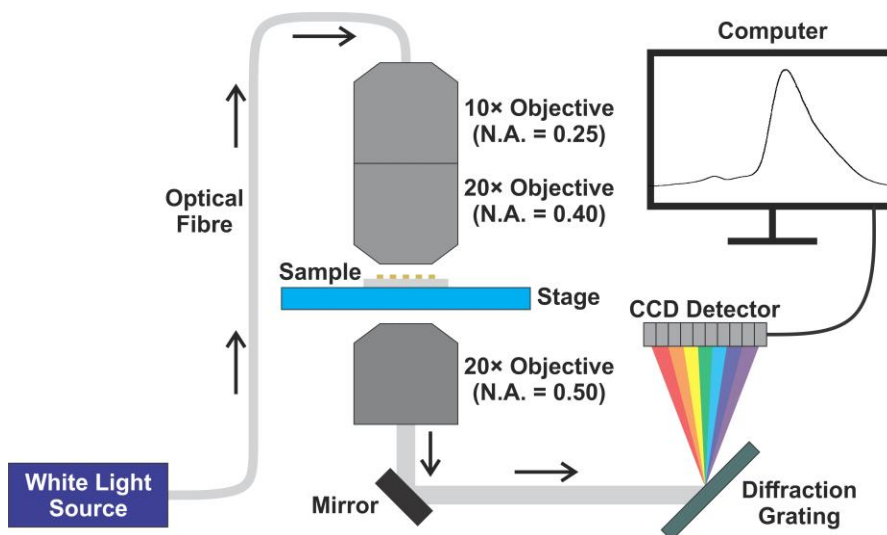
Figure 3-1 Set-up for absorption measurements in the visible-near infrared spectral range

In this thesis, absorption measurements were performed using a homebuilt setup to probe small fields of view. For the measurements in Chapter 5.2, a halogen lamp was coupled to an inverted optical microscope by a 100 μm optical fibre. The source beam was first expanded by a 10× (NA = 0.25) objective, and recollimated using a 20× (NA = 0.4) objective onto the sample, resulting in a spot size of about 50 μm. After passing through the sample, the transmitted light was collected by a 20× (NA = 0.5) objective. A pinhole size of 200 μm and a diffraction grating of 150 gr/mm were used, with a spectrometer of 800 mm focal length equipped with a liquid-nitrogen-cooled charge-coupled device (HR LabRam). Analysis was performed in the 400–1000 nm range, with an acquisition time of 1 s per spectrum over 50 accumulations to increase the signal-to-noise ratio. For the work in Chapter 4, a similar set-up was built on a Nikon Diaphot inverted optical microscope, with the analysis of the scattered light using a USB 4000-VIS-NIR-ES spectrometer (Ocean Optics, USA) with a grating of 600 gr/mm.

Fourier transform infrared (FT-IR) microspectroscopy measurements (Chapter 6.2) were performed by Dr. Greg Wallace at the Mid-IR synchrotron beamline located at the Canadian Light Source (Beamline 01B-01). The beamline end station consists of a Bruker Optics Vertex 70v FT-IR spectrometer coupled to a Hyperion 3000 IR Microscope. Light was focused and collected in absorbance mode using a 36× objective

(NA = 0.65). The collected light was measured using a narrowband fast DC coupled mercury cadmium telluride (liquid nitrogen-cooled) Kolmar detector. Measurements were collected from 8000 to 800 cm^{-1} with a spectral resolution of 4 cm^{-1}. Each spectrum is the average of 512 spectra. The absorbance measurements were performed with the background acquired on regions of the substrate void of the fractal nanostructures.

3.2   Atomic Force Microscopy

In atomic force microscopy, a sharp nanoscale tip made of silicon or silicon dioxide and supported by a flexible cantilever, is brought into contact or near-contact with a sample. By focusing a laser spot on the cantilever and tracking its deflection as it interacts with the surface, measurements of the topography of the sample can be obtained with spatial resolution of about 1 nm in the *xy*-direction and 0.1 nm in the *z*-direction. Focusing a laser on the apex of this tip has important applications in spectroscopy, leading to techniques such as nano-FTIR (Chapter 3.2.1) and tip-enhanced Raman spectroscopy (Chapter 3.3.2).

In this work, the most frequently used mode for AFM is tapping, or intermittent contact, mode. In tapping mode, the cantilever is driven by a piezoelectric element to oscillate near its resonance frequency, typically around 150-300 kHz. The amplitude of this oscillation is a few to tens of nanometres. The amplitude and frequency of the driving signal is held constant. When there is interaction with the sample, forces such as van der Waals and electrostatic forces change the amplitude of this oscillation. The feedback loop corrects for this change in amplitude and adjusts the height of the head to keep the amplitude constant.[1] The sample topography is obtained by interpreting this change in height over the sample surface. A diagram of this is shown in Figure 3-2.
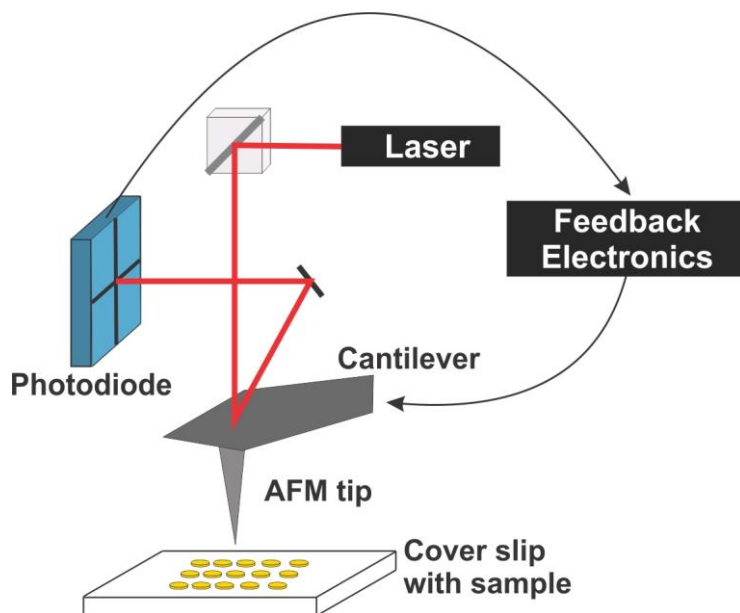
Figure 3-2 Diagram of atomic force microscope

The topographies of the samples in Chapters 4 and 5 were analyzed with a commercial atomic force microscope (NanoWizard II, JPK Instruments Inc.) in intermittent contact mode with 512×512 points per image. The AFM is equipped with a high-resolution piezoelectric *xy* TAO stage, independent of the *xyz* control of the tip. Commercial silicon tips (NCL-50, NanoWorld Inc.), with resonance frequency of 190 kHz and force constant of 48 N/m, were typically used in the measurements, unless otherwise specified.

3.2.1 Nano-FTIR

Due to the diffraction limit of light, Fourier-transform infrared spectroscopy (FTIR) cannot be applied to nanoscale samples. In order to measure the infrared spectrum of samples on the nanoscale, a technique called nano-FTIR was used. In nano-FTIR, a laser is focused on the apex of tip as it interacts with the sample. As the tip moves over the sample, the laser light scattered from the tip changes as a function of the properties of the sample. Nano-FTIR involves tracking this scattered light. In an optical heterodyne configuration, the beam is modulated, the further analysis of which yields amplitude- and phase-resolved measurements in the near-field.[2]

The stage of the sample is placed into one arm of a Michelson interferometer, with the reference arm as a mirror on a piezo stage (Figure 3-3). A quantum cascade laser (QCL), tunable between 3.6 and 12 µm, is focused on the surface of the sample through the use of a parabolic mirror. A mirror on top of the sample collects the light onto the detector. The backscattered signal of the laser on the tip while translating the reference mirror yields an interferogram. Subsequently, the Fourier transform of this interferogram can be calculated, resulting in the near-field spectrum of the sample. By tuning the QCL to a specific plasmon mode and scanning over the surface, a map of the intensity of this signal over the surface is obtained.[3] In this work, the s-SNOM instrument is the neaSNOM (Neaspec GmbH). The experiments, in Chapter 6.2.1, were conducted at Neaspec in Germany by Dr. Max Eisele.
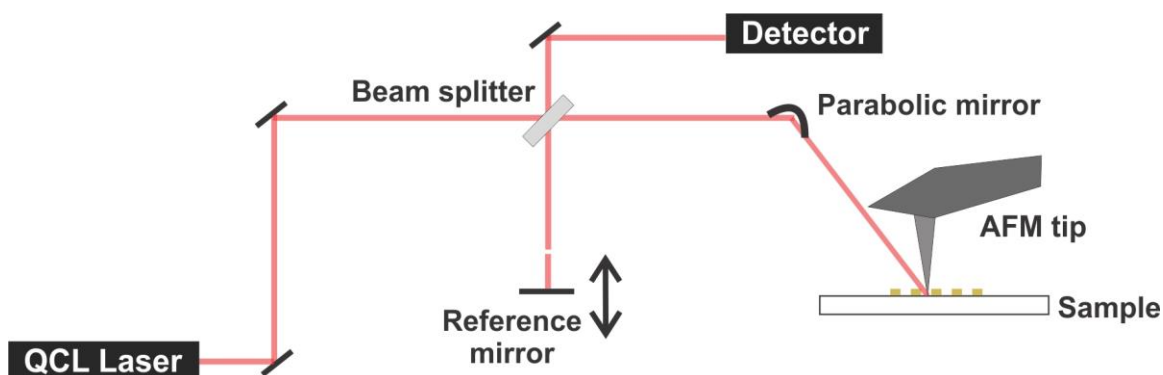
Figure 3-3 Set-up for nano-FTIR measurements

3.3 Raman Spectroscopy

As discussed in Chapter 2.1, Raman spectroscopy is based on the detection of the inelastic scattering of light. As most light is scattered elastically, Raman spectroscopy has a very low quantum efficiency, necessitating the exploitation of the enhanced electric fields near metallic nanoparticles in surface- and tip-enhanced Raman spectroscopy. Here, only the methods of these techniques are discussed.

3.3.1 Surface-Enhanced Raman Spectroscopy

In Raman and surface-enhanced Raman spectra, a laser, having passed through an interference filter to clean-up the excitation source, is focused on the sample by an

objective. The laser light is scattered by the sample, and collected back by the same microscope objective and filtered using an edge or notch filter that removes the elastically scattered photons from the excitation laser line. Interestingly, the edge (or notch) filter fully reflects the incident excitation, but transmits the Stokes Raman photons, and is generally a key optical component of compact Raman microscopes. In the spectrometer, a confocal pinhole controls the spot size on the diffraction grating, which diffracts the light on the charge-coupled device (CCD) detector. This principle is shown in Figure 3-4 and was similar to the three Raman microscopes used in this thesis.
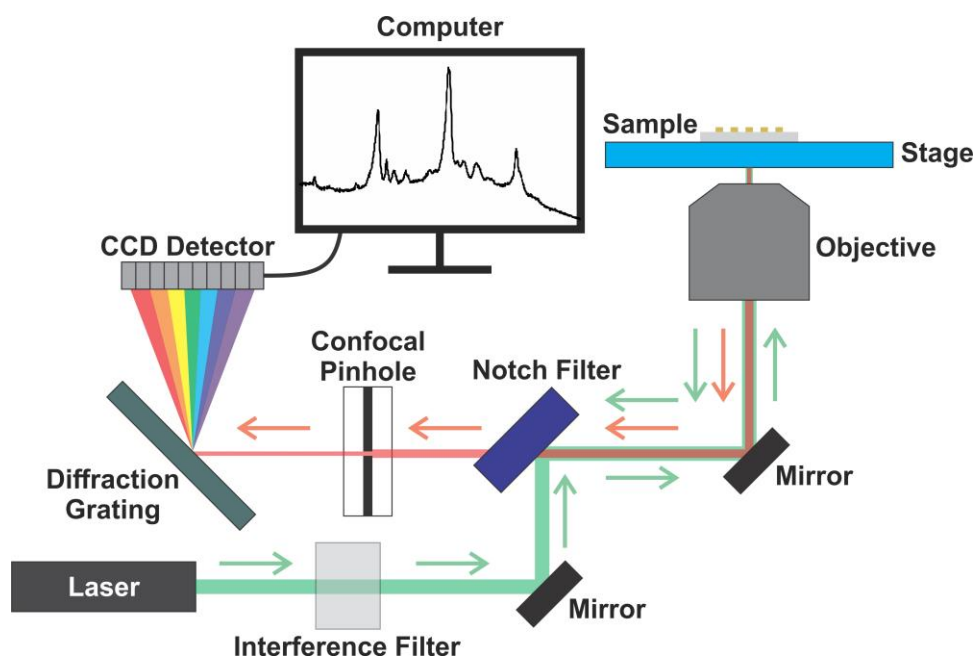
Figure 3-4 Set-up for the measurements of Raman and surface-enhanced Raman spectra

For the work in Chapter 4, SERS was measured using a Horiba Xplora Plus Raman spectrometer with a 600 gr/mm grating and an excitation wavelength of 638 nm. The spectrometer slit width was 100 µm and a 100× objective (NA = 0.7) was used to collect the scattered Raman signal. The laser power at the sample was 1 mW, with an acquisition time of 10 s.

For the work in Chapter 6.3.2, SERS measurements were performed on a Renishaw inVia Raman spectrometer available at Surface Science Western. The StreamLineHR mode was used, with an excitation wavelength of 632.8 nm. A 100× objective was used to collect the scattered Raman signal, with a spectrometer slit width of 50 µm. The laser power at the sample was 0.88 mW, with an acquisition time of 500 ms.

All other SERS spectra were recorded on the HR LabRam set-up, in the same manner as the TERS spectra as described in the following section, but in the absence of the TERS tip.

3.3.2 Tip-Enhanced Raman Spectroscopy

The TERS setup (Figure 3-5) combines a Raman spectrometer (HR LabRam, Horiba) connected to an inverted optical microscope (Olympus IX71) with an AFM (NanoWizard II, JPK Instruments). The laser is focused by a 100× objective (NA = 0.9, PlanAPO Olympus) on the sample and metallized tip from below, in transmission mode, and the same objective collects the scattered Raman signal. This signal is detected through the use of a liquid-nitrogen-cooled charge-coupled device (Horiba, Symphony), with the fundamental laser line (632.8 nm) removed by a notch filter. The temperature of the CCD is typically -124 °C. In order to align the metallized tip in the focal point of the objective, a photodiode is connected to the AFM control so that the Rayleigh scattering from the tip is detected.
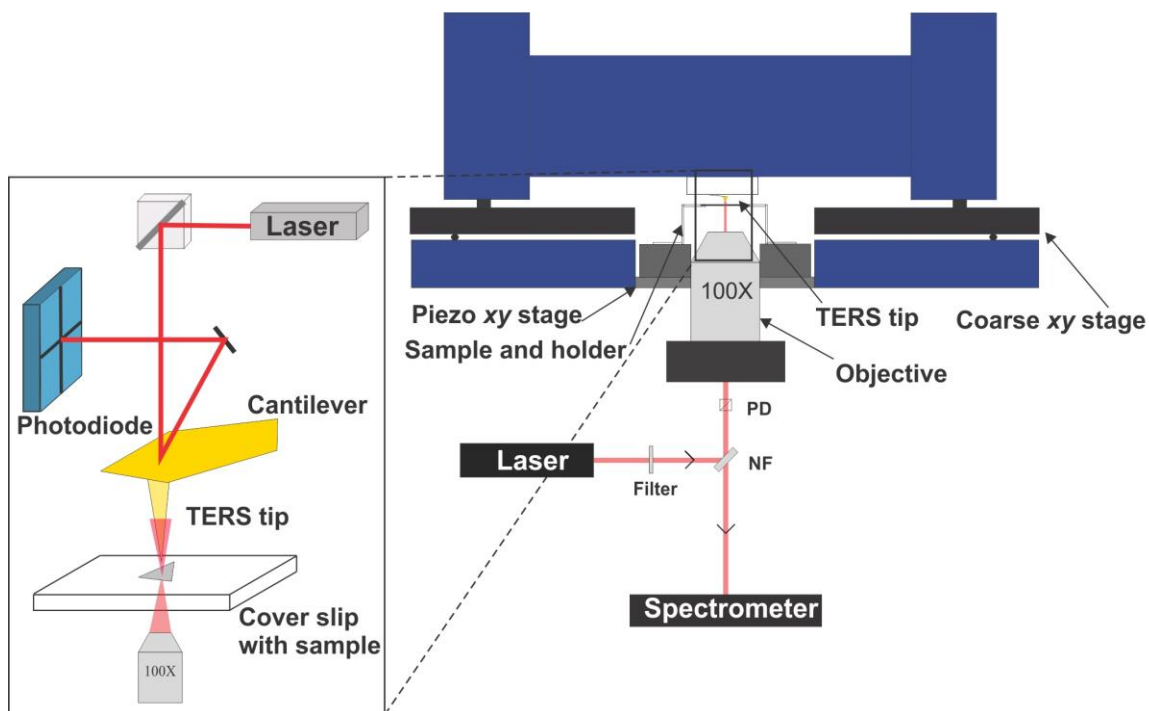
Figure 3-5 TERS set-up, with inset showing the tip interaction with the sample as controlled by the AFM

The excitation laser of 632.8 nm was set to an intensity of 1 mW before the sample, and the Rayleigh scattering from the TERS tip was measured by the photodiode. The tip was aligned to the centre of the focal point, and the tip was frozen in the x- and y-directions. An AFM topography scan was first obtained by scanning the sample under the tip while the tip remains frozen in position. All AFM measurements were performed in intermittent contact mode, with a setpoint of ca. 10-20 nm.

The TERS signal was then collected at selected points or arrays with a 600 gr/mm grating and a spectrometer slit width of 200 µm. Spectra were typically recorded in the 700 – 1800 cm^{-1} range, with a 10 s acquisition per spectrum, and the corresponding SERS spectra collected under the same conditions in the absence of the TERS tip. TERS results are presented in Chapter 5.2.

In the following sections, the technical aspects of TERS and the factors influencing the TERS enhancement are discussed.

3.3.3 Tip Fabrication

One challenge in obtaining successful TERS measurements is the fabrication of reproducible TERS active probes. Ideally, TERS probes exhibit a localized surface plasmon resonance that matches the excitation wavelength, with the shape and size of the tip suitable for atomic force microscopy measurements. Silver and gold are the most common candidates for efficient TERS enhancement, sometimes with a protective layer on silver tips to protect from oxidation.[4] There are commercial TERS tips available for purchase, but they are often also fabricated in-house. Tips may be fabricated through the electrochemical etching of metal wires.[5,6] Most simply, commercial AFM tips, made of Si or Si_3N_4, are coated with gold or silver through physical evaporation or sputtering methods,[7] or through wet chemical or electrochemical deposition.[8,9] The geometry of the apex of the tip is critical to the TERS enhancement, as any variation in the geometry will change the localized electric field. Due to this, TERS tips have a poor reproducibility, even among tips prepared in the same manner.

The TERS tips used in this study were commercial AFM tips (NCL-50, NanoWorld) onto which was deposited an adhesion layer of 5 nm of Ti, followed by 20 nm of Au by electron-beam evaporation. The deposition rate was typically 0.3–0.5 Å/s. An SEM image of a TERS tip prepared in this manner is shown in Figure 3-6a.

3.3.4 Alignment of Tip and Laser Focal Spot

Another challenge in TERS measurements is obtaining a precise alignment of the tip with the focused laser spot, which is critical to TERS enhancement. This requires the precise determination of the position of the tip apex on the cantilever, in order to then move it to the focal spot of the focused laser.

In this work, the method of alignment relies on the Rayleigh scattering of the tip. The laser is focused on the sample, and the TERS tip is scanned over the laser spot. The scattered signal is detected using a photodiode, which is input into the AFM controller. This generates an image of the scattered light. If the laser focus is optimal, the tip apex can be located as a bright spot near the top of the cantilever (Figure 3-6b,c). Depending on the geometry of the tip and the focus, other bright spots can be observed; however, the

tip apex is usually located a symmetrical distance from the edges of the cantilever, aiding in discriminating the scattering from the tip apex from other bright spots. After determination of the position of the tip apex, the tip and the focal spot are precisely aligned using piezoelectric actuators that provide lateral positioning of the tip above the focal spot with sub-nanometer resolution. Subsequent scans of the sample surface are performed with the tip frozen in the x- and y-directions, moving only the sample.
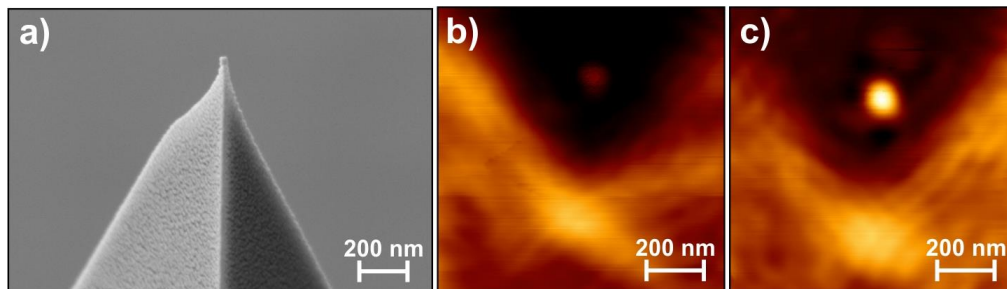
Figure 3-6 a) SEM image of a gold-coated TERS tip; Alignment by Rayleigh scattering of the tip with b) improper focus and c) proper focus.

It is also possible to align the tip and the laser focal spot by measuring the Raman signal of the tip, with the point of highest intensity corresponding to the tip apex, under appropriate focus of the excitation laser. As the TERS tips in question are gold- or silver-coated silicon, it is possible to measure a strong signal of silicon.

3.3.5 Laser Polarization

The polarization of the excitation laser is crucial to local enhancement at the tip apex in TERS measurements. Optimal enhancement is achieved when a large component of the excitation light is polarized along the tip axis.[10,11] In a transmission TERS system, with bottom illumination, there is a polarization component along the tip axis when irradiated by a tightly focused, linearly polarized laser; however, it is fairly weak, as the main polarized component is perpendicular to the tip axis, providing no strong charge confinement at the tip apex. A larger polarization component along the tip axis can be achieved in a side-illumination geometry, with a large incident angle. The enhancement possible in the TERS measurements presented here is, in part, limited by the laser polarization and geometry of the system.

3.3.6 Limitations and Difficulties in TERS

TERS measurements are limited by the quality of the TERS tip, which is susceptible to both mechanical and chemical degradation. Mechanical damage to the tip occurs during use in AFM scans before obtaining TERS measurements, resulting in the change of shape or removal of the metal at the tip apex. This can be mitigated by changing AFM parameters to minimize tip-sample interaction. When necessary, an AFM scan of higher quality was obtained after TERS measurements. Tip degradation could also be caused by laser-induced heating, potentially changing the size and shape of the tip apex.

Chemical degradation of the tip can be caused by the reaction of ambient gases with the metal coating of the tip. For example, the oxidation of silver tips greatly reduces their TERS enhancement over time, necessitating their application to TERS measurements soon after preparation. Resistance of the tips to mechanical or chemical damage could be improved through coating an additional layer of alumina or silicon oxide, but this is likely to decrease the TERS enhancement of the tip.[11,12]

Additionally, during TERS measurements it is possible that small molecule analytes migrate from the sample to the tip, contaminating the tip. When this occurs, a SERS spectrum of the molecule on the tip is obtained, dominating over the spatially resolved TERS measurement. It is possible to ascertain whether a spectrum in question originates from a molecule adsorbed on the tip by placing the tip in a position where no sample is present (for example, on a clean glass coverslip) and collecting a spectrum. If a strong signal is obtained, it is likely that the tip is contaminated.

Lastly, the overall enhancement in TERS is typically lower than the enhancement achieved in SERS measurements, in part due to the fact that TERS exploits the enhancement of a single or very few nanoparticles at the apex of the tip, while SERS typically uses arrays or assemblies of nanoparticles. This can result in low or no TERS signal for some materials, which can be improved through the use of a metal substrate, allowing for gap-mode TERS.[13,14]

3.4   Modelling the Electric Field

Computational modelling can be used in order to determine the electric field in the near-field of plasmonic nanoparticles; while the electromagnetic field of simple geometries, such as spheres, can be computed analytically, no exact solutions can be calculated for more complex geometries.[15] These methods allow for the determination of the electromagnetic hotspots of plasmonic nanoparticles, individually or in arrays, ascertaining their efficacy in applications such as surface- and tip-enhanced Raman spectroscopy. This can be done through developing approximate solutions to Maxwell's equations, either in integral or differential form. Most commonly, solutions to the integral forms of Maxwell's equations are computed through discrete dipole approximation (DDA), involving the approximation of a nanoparticle by a finite array of polarizable points, or boundary element method (BEM), involving the calculation of the electric field at interfaces. Both of these techniques generally constitute calculations in the frequency domain, and are only valid for free-space scattering, inapplicable to scatterers on a substrate without further modification.[16,17] Due to the slow convergence of frequency-domain methods, solutions are limited to order 10^7 electromagnetic field unknowns; in time-domain techniques such as the finite-difference time-domain (FDTD) method, more than 10^{12} electromagnetic field unknowns can be calculated.[18] In solving Maxwell's differential equations, FDTD and finite element method (FEM) are the most common techniques.

3.4.1 Finite-Difference Time-Domain Method

Finite-Difference Time-Domain (FDTD) is an efficient method to apply to the wave optics regime, where the structures are on the order of the wavelength of the impinging light. FDTD involves numerically discretizing and solving Maxwell's equations on a grid in space and time, with derivatives calculated by finite differences. The advantages of this method are that, apart from the finite mesh and time steps, no approximations or assumptions are made; it solves all vector components of the electric and magnetic fields; and, as it is a time-domain method, a single simulation can give broadband results.[19]

To calculate the local electromagnetic field, Maxwell's equations, which describe the electric field $\boldsymbol{E}$ and magnetic field $\boldsymbol{B}$ in a medium, are discretized. These equations can first be expressed as a series of differential equations:

$$\nabla \cdot \boldsymbol{E} = \frac{\rho}{\varepsilon_0} \qquad\qquad \nabla \cdot \boldsymbol{B} = 0$$

$$\nabla \times \boldsymbol{E} = -\frac{\partial \boldsymbol{B}}{\partial t} \qquad\qquad \nabla \times \boldsymbol{B} = \mu_0 \left(\boldsymbol{J} + \varepsilon_0 \frac{\partial \boldsymbol{E}}{\partial t} \right) \qquad\qquad (\boldsymbol{3.1})$$

where ρ and $\boldsymbol{J}$ are the charge and current density, and μ_0 and ε_0 are the permittivity and permeability of free space, respectively.

In FDTD, Maxwell's curl equations are discretized on a mesh, such that a point in a Cartesian coordinate system can be expressed as $(i, j, k) = (i\Delta x, j\Delta y, k\Delta z)$. In this instance, $\Delta x, \Delta y$ and Δz represent the size of the grid in each respective direction. This discretization is called a Yee cell (Figure 3-7), where the components of $\boldsymbol{E}$ and $\boldsymbol{B}$ are spatially offset, with the electric field components on the edges of the cubic lattice and the magnetic field components on the faces. Material properties, such as the permittivity, are also discretized on this cell. Due to this, there can be staircasing effects when the interface of a material lies on an angle with respect to the Cartesian axes of the cell, resulting, in some cases, in unphysical hotspots.
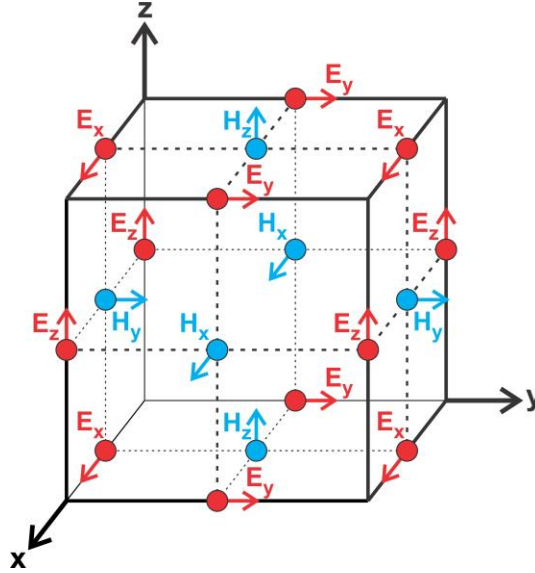
Figure 3-7. Illustration of a Cartesian Yee cell, showing the distribution of the electric field (red) and magnetic field (blue) vector components over the cell.

Calculation of B and E involves a "leapfrog" update: $H = \mu B$ is first calculated at time n, and E is calculated at time $n + \frac{1}{2}$. This allows for second order accuracy in time.

$$E^{n+\frac{1}{2}} = E^{n-\frac{1}{2}} + \frac{\Delta t}{\varepsilon} \nabla \times H^n \tag{3.2}$$

$$H^{n+1} = H^n - \frac{\Delta t}{\mu} \nabla \times E^{n+\frac{1}{2}} \tag{3.3}$$

Where Δt is the time step, and μ and ε are the permittivity and permeability of the material, respectively.[19] This leapfrog process is repeated until the results converge and a steady-state solution is achieved. As the memory required to run the simulation scales as $\left(\frac{\lambda}{\Delta x}\right)^3$ and the time required scales as $\left(\frac{\lambda}{\Delta x}\right)^4$, where λ is the wavelength of interest, the size of the Yee cell must be chosen to balance between the required simulation time and memory and the precision of the simulation.

In this thesis, Lumerical FDTD Solutions (Vancouver, Canada) is used to carry out FDTD calculations of optical scattering cross-section, and electromagnetic field and

charge distribution of fractal structures. Convergence testing was performed to determine the appropriate mesh size.

In Chapter 6.2.1, the Bethe lattice nanostructures were modelled with a rod width of 50 nm, with the length, number of branches and generation varying as indicated. The thickness of the titanium layer was 3 nm, with a gold layer of 20 nm, modelled using the dielectric values for gold and titanium from Palik.[20] The structures were placed on a substrate with a constant refractive index of 1.42, representing the CaF_2 window. A plane wave source was used for all calculations, along with periodic boundary conditions along the x- and y-directions, and perfectly matched layers along the z-direction. Mesh sizes of 3 nm along the x-, y-, and z-directions were used near the structure. For the iso-wavelength maps, the electric field maps were calculated for a wavelength range of 1.4 to 12 μm, and analyzed in MATLAB (MathWorks, USA). The electric field maps of the gold Sierpiński nanostructures (Chapter 6.3.2) were constructed in a similar manner, with nanoprisms with a base length of 125 nm, with the same metal thickness and dielectric constants. In order to truncate the simulation area, perfectly matched layers were applied along all boundaries, at least 400 nm from the Sierpiński nanostructures. The structures were meshed by a grid of 2×2 nm in the x- and y-directions, with a mesh of 3 nm in the z-direction. A maximum of 10 mesh cells per wavelength was applied outside of the Sierpiński nanostructures.

For the simulations presented in Chapter 6.3.1, the silver Sierpiński fractal structures were of sizes as indicated, with a thickness of 30 nm to match the structures as fabricated. The inverse fractal structures were modelled by etching the same fractal structures in a silver layer of the same thickness. All structures were placed on a SiN substrate. Materials were modelled using the dielectric functions of silver from Palik[20] and that of silicon nitride from Luke.[21] The Sierpiński fractal structures of 285 nm side length were meshed with a grid with sizes of 1.5 nm in the x- and y-directions, and 2 nm in the z-direction. For the largest Sierpiński structures, a mesh of 6.5 nm was used for the x- and y-directions, while maintaining the 2 nm mesh in the z-direction. In the simulation region outside of the structure, the mesh was set to at least 10 mesh cells per wavelength. Perfectly matched layers (PML) were applied in the x-, y-, and z-axes to truncate the

simulation region. When applicable, symmetry boundary conditions were applied along the *x*-minimum boundary, in order to reduce computation time.

3.4.2 Finite Element Method

In the finite element method (FEM), Maxwell's equations are also discretized on a mesh, much like FDTD. Compared to FDTD, FEM is much more computationally expensive and is computed in the frequency domain, making broadband simulations difficult.[22] However, the advantage of FEM is such that it is a versatile method and can easily be used to solve differential equations apart from Maxwell's equations; it is for this reason that FEM is used here, as the electric field result is used in subsequently solving for the resultant heating.

In this thesis, COMSOL Multiphysics 5.2 was employed for finite-element modelling of the electric field of the TERS tip and the resulting temperature rise in Chapter 5.3.4. The TERS tip was modelled as an inverted Si cone with an angle of 22.5°, with a 30 nm diameter spherical tip and a 20 nm thick Au shell. The simulation area was 2 μm wide and 600 nm tall. The tip was positioned above the silver nanoplate layer, which was 50 nm thick, in air. The simulation area was meshed by tetrahedral elements, with a size of 2 – 50 nm, a growth rate of 1.45 and a curvature factor of 0.5. Where necessary, the relative permeability was set as 1. The initial conditions were such that there is no electric field present and the temperature is 293.15 K. All boundaries were held at the initial temperature, except the top of the tip, which was thermally insulated. To truncate the simulation region by absorbing reflections, perfectly matched layers (PMLs) of 200 nm were set at the edges of the simulation region, and the PML was meshed using a swept mesh of eight layers. A scattering boundary condition was applied along the top face of the air boundary. The bottom of the simulation region was illuminated by a tightly focused Gaussian beam with a wavelength of 632.8 nm, 1 μm spot size and 1 mW of power. As the beam was tightly focused, the longitudinal component of the electric field was set to be:[23]

$$E_z = ik_0 \frac{\partial E_x}{\partial x} \tag{3.4}$$

The electric field is calculated using the Wave Optics module, and is linked to the Heat Transfer Module using the Multiphysics approach.

3.5   Electron Microscopy

Up to this point, techniques discussed have been based on the interaction of light with materials. Electron microscopy uses electrons in the place of light, with the short wavelength of electrons allowing for increased spatial resolution compared to conventional light microscopy. Advanced techniques, such as electron energy loss spectroscopy (EELS), allow for the spectroscopic imaging of plasmon modes of nanomaterials through their interaction with electrons.

3.5.1 Scanning Electron Microscopy

In scanning electron microscopy, an image of the topography of a sample is formed by scanning a beam of focused electrons over a sample and detecting the electrons after they have interacted with the sample. These interactions can include: the generation of secondary electrons as ionization products; back-scattering electrons, reflecting off the sample; and the emission of characteristic X-rays or photons (Figure 3-8).[24] Measurements are performed under vacuum, to avoid electrons scattering off molecules in the air. Electron microscopy requires conductive samples, except for the case of certain partial vacuum SEM, to avoid charging the sample, which significantly decreases spatial resolution of the image.

With back-scattered electrons, electrons from the incident beam are elastically scattered. This scattering occurs deeper in the sample, resulting in poorer spatial resolution of images formed from this process. However, the probability of elastic scattering is related to the atomic mass of the element, allowing for the identification of areas of different elemental composition. This technique is often used with energy-dispersive X-ray spectroscopy (EDX), where the characteristic X-rays of a sample are analyzed, in order to determine the chemical composition of these different areas.[24]

Images formed from secondary electrons are of better spatial resolution, due to this process occurring at or closer to the surface of the sample. For this reason, this is the main method of imaging samples in SEM.
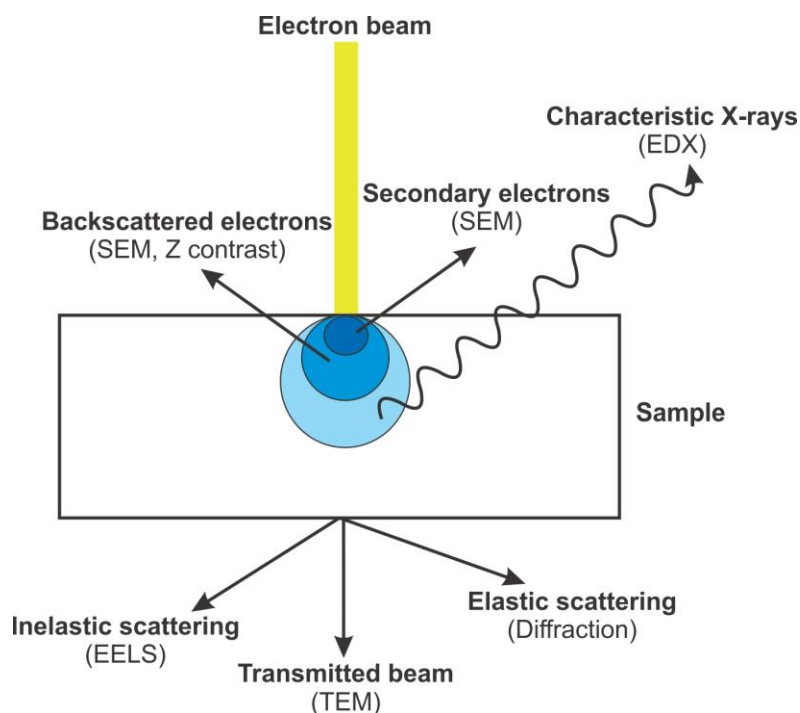
Figure 3-8 Diagram of typical interactions between the incident electron beam and the sample in electron microscopy

Scanning electron microscopy was used to image nanomaterials in Chapter 4.3, 5.2, 6.2 and 6.3, and TERS tips in Chapter 5.4. For the imaging of nanomaterials, a LEO Zeiss 1530 SEM was used. To image and analyze TERS tips, a LEO Zeiss 1540XB (Zeiss, Oberkochen, Germany) fitted with an Oxford Instruments X-ray system, allowing for *in situ* EDX analyses and mapping, was used.

3.5.2 Transmission Electron Microscopy

In transmission electron microscopy (TEM), a micrograph of the sample is formed by passing the electron beam through the very thin sample. Instead of detecting scattered electrons as in SEM, transmitted electrons are detected. The probability of an electron passing through the sample without scattering is inversely proportional to its mass.

Therefore, heavier elements scatter more electrons, and these regions appear darker in the transmission electron micrograph. High-angle annular dark-field scanning transmission electron microscopy (HAADF-STEM) was performed in conjunction with the electron energy loss spectroscopy in Chapter 6.3. HAADF-STEM images were acquired by Isobel C. Bicket, in the group of Prof. Gianluigi Botton at McMaster University, at the Canadian Centre for Electron Microscopy.

3.5.3 Electron Energy Loss Spectroscopy

In electron energy loss spectroscopy (EELS), electrons that undergo inelastic scattering are spectroscopically analyzed in order to determine their energy loss. The sample is exposed to an electron beam narrow in energy width. Electrons are scattered inelastically as they pass through the sample, and the cause of their energy loss is determined. In this thesis, this is most relevant to the study of plasmonic nanoparticles: electrons that scatter off these plasmon resonances will differ by the energy of the plasmon mode. This allows for an accurate experimental determination of the energy of a plasmon mode, with the nanoscale spatial resolution of the TEM.[25] EELS images can be obtained by measuring the EELS spectrum over the surface of the nanostructure, as it is exposed to the electron beam.

Electron energy loss spectrum images in Chapter 6.3.1 were acquired by Isobel C. Bicket on a monochromated FEI Titan microscope at 80 kV, equipped with a Gatan Tridiem (model 865) spectrometer. An energy resolution of approximately 60 meV (about 15 nm) was achieved, as measured from the full width at half maximum of the zero loss peak (ZLP). The Richardson-Lucy deconvolution algorithm was used on the acquired spectrum images to deconvolve the effect of the point spread function (PSF) of the microscope from the response of the fractal nanostructures, effectively improving the energy resolution to approximately 40 meV. Analysis of the EELS images was performed using custom Python software. All spectra were normalized to the maximum intensity of the ZLP. Nanostructures for EELS were study by EELS were fabricated by electron-beam lithography using silver, so that higher-order modes would lie in the visible range rather than the mid-infrared.

3.6   Fabrication of Plasmonic Nanomaterials

One important aspect of the study of plasmonic nanomaterials is the fabrication of such nanomaterials. Nanoparticles are formed in two different ways: by wet chemical synthesis, termed "bottom-up", or by lithographic "top-down" methods. Both are discussed here, in the bottom-up synthesis of colloidal silver nanoplates, and the top-down methods of nanosphere lithography and electron-beam lithography.

3.6.1 Synthesis of Silver Nanoplates

As the shape and size of a nanoparticle is critical to its optical properties, many synthesis methods have been developed for nanoparticles of different shapes, including spheres,[26] rods,[27,28] worms,[29] cubes,[30] stars[31] and rice grains.[28] Here, as the TERS measurements occur in transmission, an ultrathin nanoplate is critical to allow the laser to pass through the nanoplate and reach the analyte on its surface. A flat surface is crucial to avoid parasitic SERS scattering. These characteristics are met by a synthesis method reported by Zhang *et al.,*[32] wherein a seed solution is first made, and then successive slow rounds of growth are performed to achieve the nanoplates with high aspect ratio. These nanoplates are used for tip-enhanced Raman measurements in Chapter 5.

A seed solution was prepared by combining aqueous $AgNO_3$ (0.1 mM, 25 mL), trisodium citrate (30 mM, 0.3 mL), poly(vinylpyrrolidone) (MW $\sim$ 29 000 g/mol, 3.5 mM, 1.5 mL), and H_2O_2 (30 wt %, 60 µL) under stirring. An aqueous $NaBH_4$ solution (100 M, 250 µL) was injected, and the solution was stirred for 30 min. The solution was centrifuged at 11 000 rpm for 8 min, and the nanoplates were redispersed in deionized water. This washing step was repeated twice, and the seeds were then dispersed in 40 mL of deionized water. In the seeded growth process, L-ascorbic acid (0.1 M, 0.375 mL) and trisodium citrate (0.075 M, 0.125 mL) were injected to 10 mL of the seed solution under stirring. A solution of $AgNO_3$ (1 mM, 20 mL), citric acid (0.1 M, 0.125 mL), and sodium citrate (1.5 mM, 0.1 mL) was prepared. It was added to the seed solution using a syringe pump at a rate of 0.2 mL/min. After injection, 20 mL of the reaction solution was removed and the remaining solution was used as seeds for the next growth cycle. In total, four rounds of growth were performed. Nanoplates were drop-cast onto clean coverslips,

for characterization by atomic force microscopy and scanning electron microscopy. SEM images are shown in Figure 3-9.
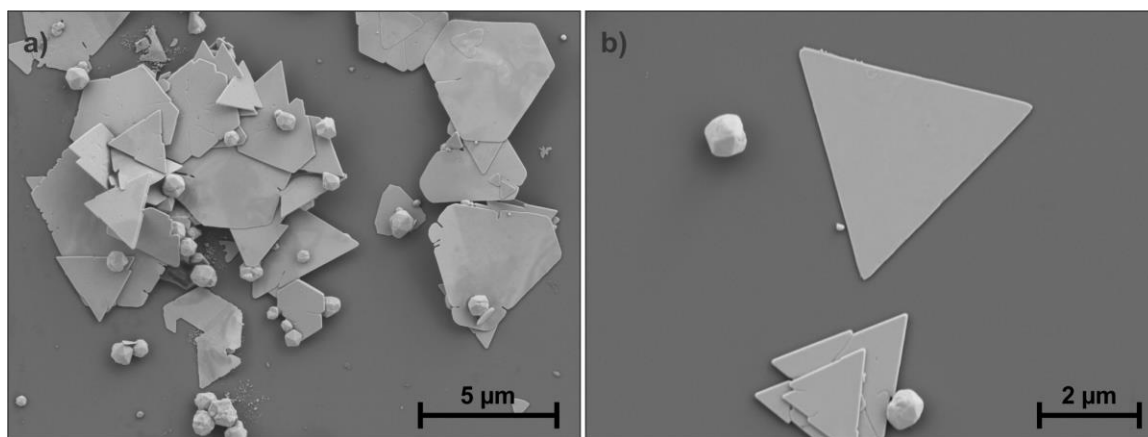
Figure 3-9 Scanning electron micrographs of the silver nanoplates, showing a) stacked nanoplates, with the byproduct multifaceted nanoparticles; b) an isolated nanoplate, suitable for TERS measurements.

3.6.2 Fabrication of Gold Nanoislands

Gold nanoisland substrates were fabricated through the electron beam-induced evaporation of 4 nm of gold onto clean glass slides, resulting in nanoparticles of diverse size, shape and orientation. The gold nanoisland substrates are used in Chapter 4.3.1, for the plasmon-mediated reduction of aryl diazonium salts.

3.6.3 Nanosphere Lithography

Nanosphere lithography (NSL) is a simple method to form a plasmonic platform over larger areas (cm^2). Instead of individually forming the nanoprisms in solution, a colloidal technique is used. First, a layer of polystyrene spheres is formed on a clean glass coverslip. Layers of titanium, as an adhesion layer, and gold, to form the plasmonic nanostructures, are deposited over the layer of polystyrene beads. The beads are removed by sonication. If a monolayer of polystyrene beads was properly formed in the first step, this leaves the glass coverslip patterned with gold nanoprisms in the areas that were not protected by the polystyrene beads (Figure 3-10).

Monolayer of Particles **Metal Deposition** **Removal of Particles**

Top View

Side View
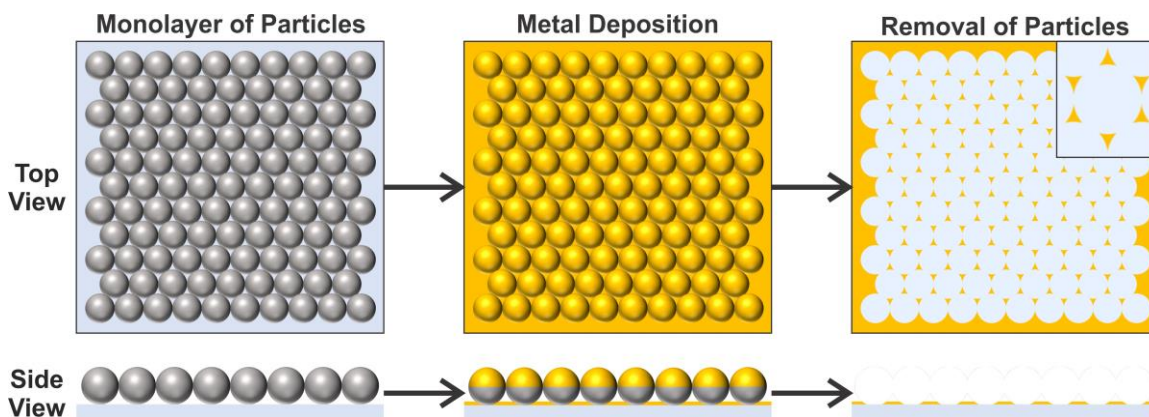
Figure 3-10 Nanosphere lithography procedure: a monolayer of polystyrene spheres is deposited on a glass coverslip. An adhesion layer of Ti is deposited, followed by a layer of gold. The nanoparticles are removed by sonication, leaving gold nanoprisms.

Polystyrene spheres (1 µm, ThermoScientific Co.) in a solution of 50% ethanol were dropcast onto a clean glass coverslip. After drying, 3 nm of Ti were deposited by electron-beam evaporation, followed by 20 nm of Au. The coverslips were then sonicated in order to remove the polystyrene spheres. NSL-patterened samples were used for the plasmon-mediated reduction of diazonium salts in Chapter 4.3.2.

3.6.4 Electron-Beam Lithography

Nanosphere lithography, as discussed in section 3.6.2, is a simple and quick method of forming plasmonic nanostructures; however, it is not without the drawback of many defects in the structures, due to poor packing of the polystyrene beads. Furthermore, the experience of the operator often greatly influences the quality of the resulting platform. Electron beam lithography is a more precise technique, allowing for the exact determination of shape and position of nanoparticles on a substrate, due to its spatial resolution of approximately 20 nm.[33] In electron beam lithography, a polymer layer, acting as a photoresist, is precisely exposed to the electron beam in a scanning electron microscope, forming the desired pattern. Exposure to the electron beam causes scission of the polymer chains, locally increasing its solubility. The sample is placed in developing solution to remove this exposed area, and metal is deposited. The remaining

polymer is then removed, leaving only the areas that had originally been exposed to the electron beam. A summary of this process is shown in Figure 3-11.
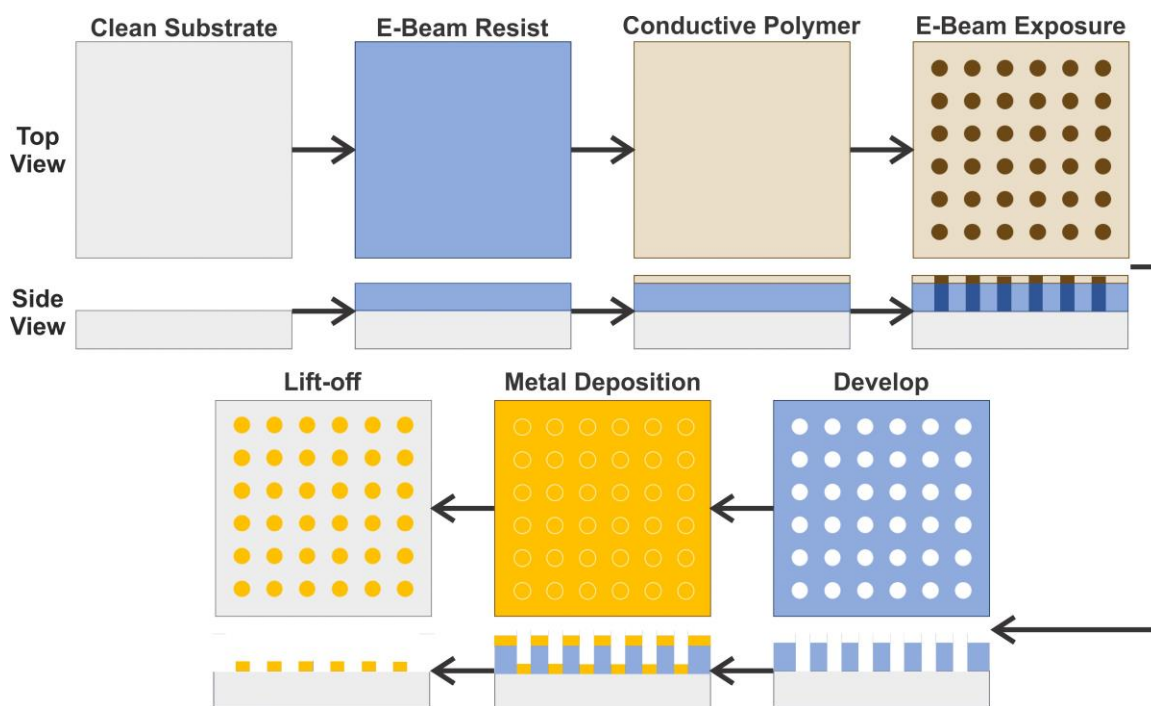
Figure 3-11 Electron-beam lithography procedure

For the nanostructures in Chapter 6.3.1, Isobel C. Bicket performed the electron-beam lithography. The nanostructures were fabricated on TEM grids with 50 nm thick suspended silicon nitride membranes. Here, the very thin substrate added to the complexity of the fabrication, but was necessary for subsequent TEM measurements. Poly(methyl methacrylate) (3% in anisole) with a molecular weight of 950 kg/mol was spin-coated into the TEM grids at 6000 rpm for 90 s. The grids were then baked at 175 °C for 5 min. Exposure of the patterns was done using Nanometer Pattern Generation System (NPGS) on a JEOL JSM-7000F SEM. The patterned resist was developed in methyl isobutyl ketone in isopropanol (MIBK/IPA) for 2 min before deposition of 30 nm of silver using electron beam evaporation and a lift-off process in acetone. A series of nanoprisms is shown in Figure 3-12a.
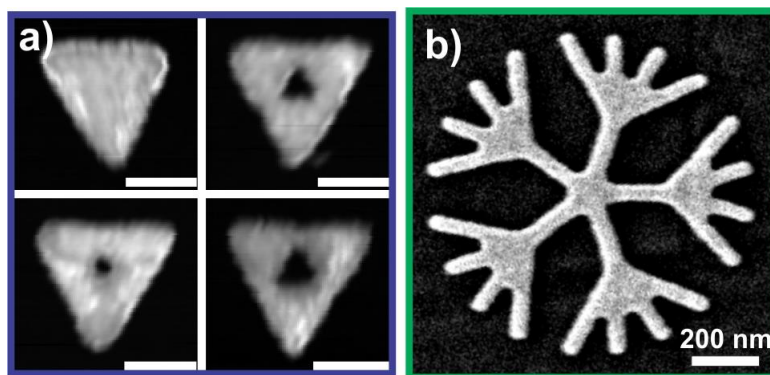
Figure 3-12 SEM images of a) silver Sierpiński nanoprisms and b) gold Bethe lattice nanostructures, as fabricated by electron-beam lithography. Scale bar inset in a) is 150 nm.

A similar method was used for the fabrication of the fractal nanostructures in Chapter 6.2 and 6.3.2. A 100 nm thick film of poly(methyl methacrylate) (PMMA, A2 950 resist, MicroChem Corp., MA, USA), was spin-coated on a clean glass coverslip, followed by a thin conductive layer (AquaSAVE, Mitsubishi Rayon America, NY, USA). The fractal structures were designed in DesignCAD 2000. Inscription of the fractal pattern on the coated coverslip surface was achieved using a LEO 1530 field emission scanning electron microscope at an acceleration voltage of 30.0 kV with an aperture of 10 µm. After inscription, the conductive layer was dissolved in water and the exposed photoresist was developed in a 1:4 mixture of MIBK/IPA (Microchem Corp., MA, USA) followed by IPA alone (VWR International, PA, USA), to halt the development process, and dried under nitrogen. A thin film of 3 nm titanium was deposited by e-beam evaporation, which served as an adhesion layer for gold, 20 nm of which was deposited by the same method. The desired structure was obtained by removing the photoresist using a liftoff procedure in acetone (CHROMASOLV, Sigma-Aldrich, MO, USA). Scanning electron micrographs of the structures were then obtained using the Leo Zeiss 1530 SEM, and shown in Figure 3-12b.

3.7 Functionalization of Plasmonic Nanomaterials

The surface of the nanostructures, fabricated by electron-beam lithography or wet chemical synthesis, was functionalized through the self-assembly of a thiol monolayer,

for study by SERS or TERS. For the work in Chapter 5, the molecule chosen was 4-mercaptophenyl benzoic acid (4-MPBA); for the work in Chapter 6.3.2, the molecule was 4-nitrothiophenol (4-NTP). In both cases, a 1 mM solution of the analyte in ethanol was prepared, in which the cover slip with the nanostructures was immersed for 24 h. The cover slip was then rinsed in absolute ethanol and deionized water, and dried under nitrogen. For the work in Chapter 4, the spontaneous functionalization process was contrasted with the plasmon-mediated process.

3.7.1 Plasmon-Mediated Functionalization

Functionalization of the plasmonic nanostructures was enhanced by plasmon excitation using a white light source (LightningCure, Hamamatsu) with a UV filter for the work on gold nanoislands in Chapter 4.3.1, and using a laser source in Chapters 4.3.1 and 4.3.2. Diazonium salt solutions, of either 4-nitrobenzenediazonium tetrafluoroborate or 4-cyanobenzendiazonium tetrafluoroborate, were prepared at a concentration of 3 mM, unless indicated otherwise. The 632.8 nm laser was focused using a 10× objective in transmission, with a power of 5.5 mW. Exposure times ranged between 10 – 90 s. After exposure, the sample was rinsed in distilled water and ethanol.
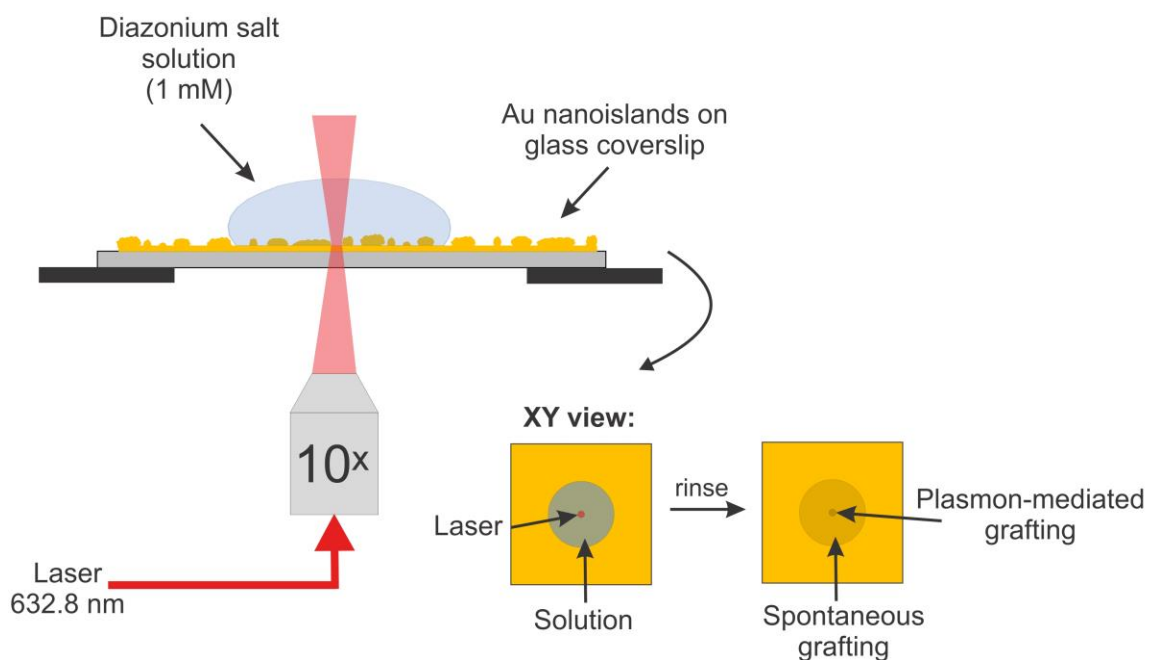
Figure 3-13 Procedure for plasmon-mediated functionalization under focused laser

3.8 References

1. Geisse, N. A. *Mater. Today* **2009**, *12*, 40-45.

2. Amarie, S.; Keilmann, F. *Phys. Rev. B* **2011**, *83*, 045404.

3. Zenin, V. A.; Andryieuski, A.; Malureanu, R.; Radko, I. P.; Volkov, V. S.; Gramotnev, D. K.; Lavrinenko, A. V.; Bozhevolnyi, S. I. *Nano Lett.* **2015**, *15*, 8148-8154.

4. Kumar, N.; Spencer, S. J.; Imbraguglio, D.; Rossi, A. M.; Wain, A. J.; Weckhuysen, B. M.; Roy, D. *Phys. Chem. Chem. Phys.* **2016**, *18*, 13710-13716.

5. Foti, A.; Barreca, F.; Fazio, E.; D'Andrea, C.; Matteini, P.; Maragò, O. M.; Gucciardi, P. G. *Beilstein J. Nanotechnol.* **2018**, *9*, 2718-2729.

6. Walke, P.; Toyouchi, S.; Wolf, M.; Peeters, W.; Prabhu, S. R.; Inose, T.; De Feyter, S.; Fujita, Y.; Uji-i, H. *J. Phys. Chem. Lett.* **2018**, *9*, 7117-7122.

7. Asghari-Khiavi, M.; Wood, B. R.; Hojati-Talemi, P.; Downes, A.; McNaughton, D.; Mechler, A. *J. Raman Spectrosc.* **2012**, *43*, 173-180.

8. Huang, T.-X.; Li, C.-W.; Yang, L.-K.; Zhu, J.-F.; Yao, X.; Liu, C.; Lin, K.-Q.; Zeng, Z.-C.; Wu, S.-S.; Wang, X.; Yang, F.-Z.; Ren, B. *Nanoscale* **2018**, *10*, 4398-4405.

9. Gao, L.; Zhao, H.; Li, Y.; Li, T.; Chen, D.; Liu, B. *Nanoscale Res. Lett.* **2018**, *13*, 366.

10. Kitahama, Y.; Uemura, S.; Katayama, R.; Suzuki, T.; Itoh, T.; Ozaki, Y. *Appl. Phys. Lett.* **2017**, *110*, 233104.

11. Kazemi-Zanjani, N.; Vedraine, S.; Lagugné-Labarthet, F. *Opt. Express* **2013**, *21*, 25271-25276.

12. Takeyasu, N.; Yamaguchi, K.; Kagawa, R.; Kaneta, T.; Benz, F.; Fujii, M.; Baumberg, J. J. *J. Phys. Chem. C* **2017**, *121*, 18795-18799.

13. Yang, M.; Mattei, M. S.; Cherqui, C. R.; Chen, X.; Van Duyne, R. P.; Schatz, G. C. *Nano Lett.* **2019**, *19*, 7309-7316.

14. Sheng, S.; Wu, J.-B.; Cong, X.; Zhong, Q.; Li, W.; Hu, W.; Gou, J.; Cheng, P.; Tan, P.-H.; Chen, L.; Wu, K. *ACS Nano* **2019**, *13*, 4133-4139.

15. Fu, Q.; Sun, W. *Appl. Opt.* **2001**, *40*, 1354-1361.

16. Loke, V. L. Y.; Mengüç, M. P. *J. Opt. Soc. Am. A* **2010**, *27*, 2293-2303.

17. Santinom, A.; da Silva, M. A.; Villa, J. E. L.; Poppi, R. J.; Mazali, I. O.; dos Santos, D. P. *Vib. Spectrosc* **2018**, *99*, 34-43.

18. Sankaran, K. *Eng. Rep.* **2019**, *1*, e12041.

19. Gedney, S. D. *Introduction to the Finite-Difference Time-Domain (FDTD) Method for Electromagnetics*; Morgan & Claypool Publishers, **2011**; Vol. 6.

20. Palik, E. D. *Handbook of Optical Constants of Solids*; Academic Press: Burlington, Ontario, **1997**.

21. Luke, K.; Okawachi, Y.; Lamont, M. R. E.; Gaeta, A. L.; Lipson, M. In *CLEO: 2015*; Optical Society of America: San Jose, California, **2015**.

22. Reddy, J. N. *Introduction to the Finite Element Method*; 3rd ed.; McGraw-Hill Education: New York, **2006**.

23. Lax, M.; Louisell, W. H.; McKnight, W. B. *Phys. Rev. A* **1975**, *11*, 1365-1370.

24. Vernon-Parry, K. D. *III-Vs Review* **2000**, *13*, 40-44.

25. Ramasse, Q. M.; Seabourne, C. R.; Kepaptsoglou, D.-M.; Zan, R.; Bangert, U.; Scott, A. J. *Nano Lett.* **2013**, *13*, 4989-4995.

26. Li, L.; Sun, J.; Li, X.; Zhang, Y.; Wang, Z.; Wang, C.; Dai, J.; Wang, Q. *Biomaterials* **2012**, *33*, 1714-1721.

27. Nikoobakht, B.; El-Sayed, M. A. *Chem. Mater.* **2003**, *15*, 1957-1962.

28. Wiley, B. J.; Chen, Y.; McLellan, J. M.; Xiong, Y.; Li, Z.-Y.; Ginger, D.; Xia, Y. *Nano Lett.* **2007**, *7*, 1032-1036.

29. Xie, H.-n.; Larmour, I. A.; Smith, W. E.; Faulds, K.; Graham, D. *Analyst* **2012**, *137*, 2297-2299.

30. Siekkinen, A. R.; McLellan, J. M.; Chen, J.; Xia, Y. *Chem. Phys. Lett.* **2006**, *432*, 491-496.

31. Plascencia-Villa, G.; Bahena, D.; Rodríguez, A. R.; Ponce, A.; José-Yacamán, M. *Metallomics* **2013**, *5*, 242-250.

32. Zhang, Q.; Hu, Y.; Guo, S.; Goebl, J.; Yin, Y. *Nano Lett.* **2010**, *10*, 5037-5042.

33. Quake, S. R.; Scherer, A. *Science* **2000**, *290*, 1536.

Chapter 4

4 Nanolocalized Chemical Reactions Induced by Plasmon Resonances

As discussed in Chapter 2.6.3, chemical reactions can be catalyzed by nanostructured surfaces through the excitation of the plasmon resonance, due to some combination of the locally enhanced electromagnetic field, hot carrier ejection and temperature increase. Since these plasmon resonances are spatially localized, it opens the possibility to trigger photochemically-induced reactions that are spatially confined. In this chapter, the plasmon-mediated reaction of aryl diazonium salts on plasmonic surfaces is described.

4.1   Introduction

Among the plasmon-mediated chemical reactions currently under study, the functionalization of the surface of nanoparticles is increasingly interesting, as it allows for the generation of locally tailored chemical reactivity on surfaces. Through further reactions, this can be used to guide larger molecules and structures, such as proteins or quantum dots, into hotspots of the nanoparticle surface.[1] The spatial location of these hotspots can change as a function of the intensity, wavelength and polarization of the excitation source; therefore, the multi-functionalization of plasmonic surfaces is possible through modification of the excitation beam. The reduction of aryl diazonium salts is one such reaction that is catalyzed by plasmon excitation, resulting in the grafting of poly(aryl) films in the hotspots of the nanostructured gold surface.[2,3] An example is shown in Figure 4.1.
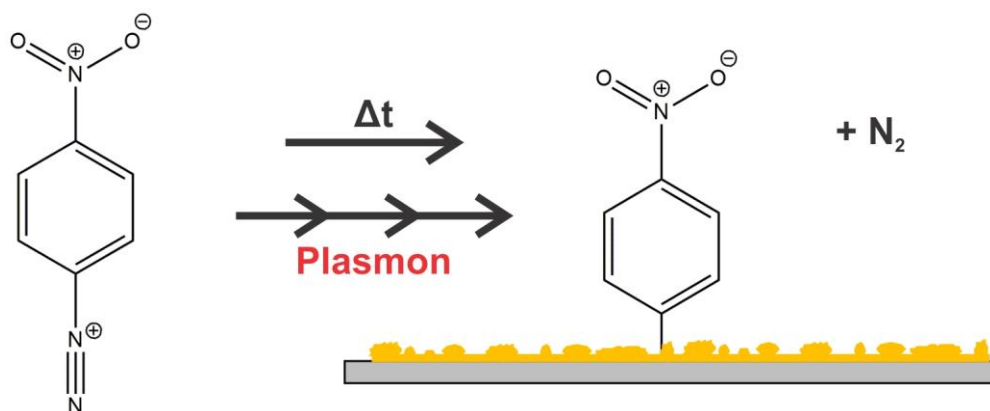
Figure 4-1 Reduction of 4-nitrobenzenediazonium on a gold nanoisland surface, as catalyzed by a plasmon resonance.

The grafting mechanism involves the hot electron transfer from the surface to the diazonium salt concomitantly with the cleavage of the dinitrogen, resulting in the production of aryl radicals.[4] These aryl radicals are then able to bind to the gold surface via covalent bonds, but can also bind to the aromatic rings already attached to the gold surface, forming extended structures through a polymerization process.[5,6] This leads to the formation of multilayers. The radicals may also diffuse in solution, potentially leading to side products that may precipitate on the surface.[4]

Interestingly, the regioselective grafting of these poly(aryl) layers derived from diazonium salts by plasmon excitation of gold nanoparticles has been shown in the literature.[2,3] This is a promising strategy for the nanoscale patterning of organic layers in the hotspots of nanostructured surfaces.

In this chapter, two types of aryl diazonium salts were used, 4-nitrobenzenediazonium tetrafluoroborate (DNO_2) and 4-cyanobenzendiazonium tetrafluoroborate (DCN), along with two substrates, gold nanoislands and gold nanoprisms, as produced by nanosphere lithography (NSL). AFM and SEM were primary tools used to investigate the spatial grafting of the materials.

4.2   Plasmon-Mediated Chemical Reactions

Chemical reactions can be photo-induced in diverse ways using plasmon resonances, and are heavily influenced by their surroundings and the optical properties of the nanostructures.

4.2.1 Inciting Plasmon-Mediated Reactions

Plasmon-mediated reactions can be incited or catalyzed by one or more of three properties of plasmon resonances and their decay: reactions can be photocatalyzed by the enhanced electric field at the surface of the nanoparticle; reactions can be catalyzed by the hot carriers that are ejected as the result of the plasmon decay; and they can be catalyzed by the resultant rise in temperature.

Reactions incited by the enhanced electric field depend upon the electronic excitation of the reactant molecules. For reactions to be photocatalyzed by the nanolocalized electric field at the surface of the nanoparticles, there must be an overlap in the absorption spectrum of the plasmonic nanostructure and the reaction precursor, as for traditional photocatalysis.[7] This method of catalysis has been applied to the catalytic photodegradation of phenol using TiO_2 with gold and silver nanoparticles,[8] and the evolution of hydrogen under visible light irradiation of a gold nanorod/carbon nitride nanotube hybrid system,[9] among others.

Reactions promoted by the hot electrons or holes that are the result of plasmon decay must also have suitable energy levels in contact with the plasmonic nanostructure, such that there is a metal-adsorbate state near the Fermi energy that can be accessed by the hot carrier. Many reactions have been attributed to the excitation of hot carriers; of interest, these include the demethylation of methylene blue, triggered by direct hot electron transfer,[10] and the oxidation of glucose, involving the direct transfer of both hot electrons and hot holes.[11]

Local heating can also increase the reaction rate, following the Arrhenius law.[12,13] Nanoparticles can be exploited in this method as nanosources of heat, as will be described in Chapter 5.3.

Reactions can be catalyzed by one of the above mechanisms, or any combination of them. Determining the method of catalysis for a given plasmon-mediated reaction is of great research interest.[14-16] It can easily be ascertained whether the photocatalysis mechanism is applicable to a given reaction through measurement of the plasmon resonance of the nanostructure and the reactant. Whether reactions are catalyzed by hot carriers or plasmonic heating can be more difficult to ascertain; this is further discussed in Chapter 5.3.1.

4.2.2 Factors Influencing Plasmon-Mediated Reactions

A given plasmon-mediated reaction and the resulting yield is influenced by the localized surface plasmon resonance (LSPR) of the metallic nanostructure, and the efficiency of the coupling between the LSPR and the plasmon-mediated reaction. As discussed in Chapter 2.2.3, the LSPR of a metallic nanostructure is a function of its composition, shape, size, spacing from other nanoparticles, and the surrounding medium. These factors, along with the characteristics of the excitation source, determine the location of the plasmonic hotspots, the regions at which the reaction is most likely to occur.[17,18]

Often, the lifetime of the hot carriers as excited by plasmon resonance is too short to participate in chemical reactions. This leads to a low efficiency of charge transfer from the plasmonic nanostructure to the reaction precursor.[19,20] Charge transfer mediators, such as semiconductors, are used to increase this efficiency, and can be tuned to influence the population of charge carriers. Under Schottky contact, hot electrons can be separated from hot holes, preventing their fast recombination.[21,22] Conversely, with Ohmic contact, lower energy electrons, such as those from interband transitions, are permitted to transfer from the metal to the semiconductor.[22]

4.2.3 Plasmon-Catalyzed Polymerization Reactions

Polymerization reactions have been catalyzed through plasmon excitation. As the polymer product are not typically soluble, this allows for the correlation between nanoparticle geometry and hotspots in which hot carriers are generated. This permits the experimental mapping of the LSPR resonances for reactions that are primarily catalyzed by hot carriers. Such reactions have been carried out using a variety of nanoparticles,

including nanorods,[3] nanodisks and spheres,[6,23,24] and nanoprisms.[2] Plasmon-catalyzed polymerization reactions have also been catalyzed through tip-enhanced Raman spectroscopy (TERS). The Deckert group has demonstrated the polymerization of dibenzo(1,2)dithiine-3,8-diamine on a gold nanoplate, involving the coupling of amino groups to form azo groups as observed in the TERS spectra.[25] As the silver-coated tip scans during measurement, the polymerization occurs over the surface of the nanoplate. This could be further extended to locally generate one-dimensional materials through further control of the polymerization reaction.

Conversely, in reactions primarily catalyzed by the localized heating that results from plasmon excitation, a uniform polymer coating is typically formed.[12] These polymerizations have found applications as molecular thermometers, to estimate the temperature reached due to plasmonic heating. For example, soybean oil, a mix of triglycerides, polymerizes above 230 °C, allowing for a rough estimation of the temperature upon observation of the polymerization reaction.[26]

4.3 Reduction of Diazonium Salts Catalyzed by Plasmons

Here, the reduction of aryl diazonium salts, DCN and DNO_2, are studied on gold nanoisland and NSL substrates.

The work in Chapter 4.3.1 was conducted in collaboration with the groups of Profs. C. Mangeney and N. Félidj at Université de Paris, within a collaboration funded by a Mitacs Globalink Research Award.

4.3.1 Gold Nanoisland Substrate

In order to study the reduction of diazonium salts, gold nanoisland substrates were fabricated as described in Chapter 3.6.2 and characterized by scanning electron microscopy (SEM), as shown in Figure 4-2. The surface shows nanoparticles of random shape, size and orientation.
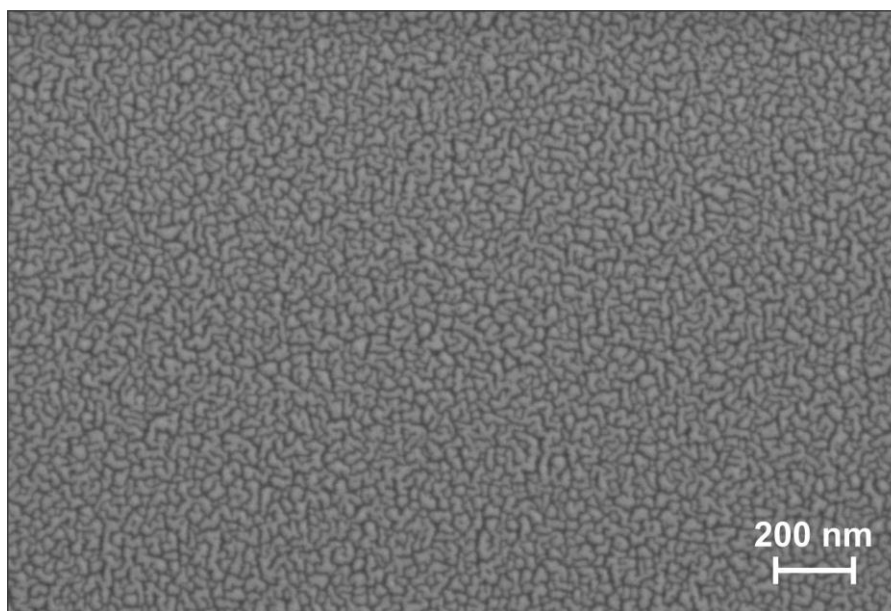
Figure 4-2 SEM image of the gold nanoisland surface

To determine the ideal excitation for plasmon-mediated functionalization, an absorption spectrum was collected, and is shown in Figure 4-3. This shows a broad resonance, due to the random nature of the gold nanoisland assembly.
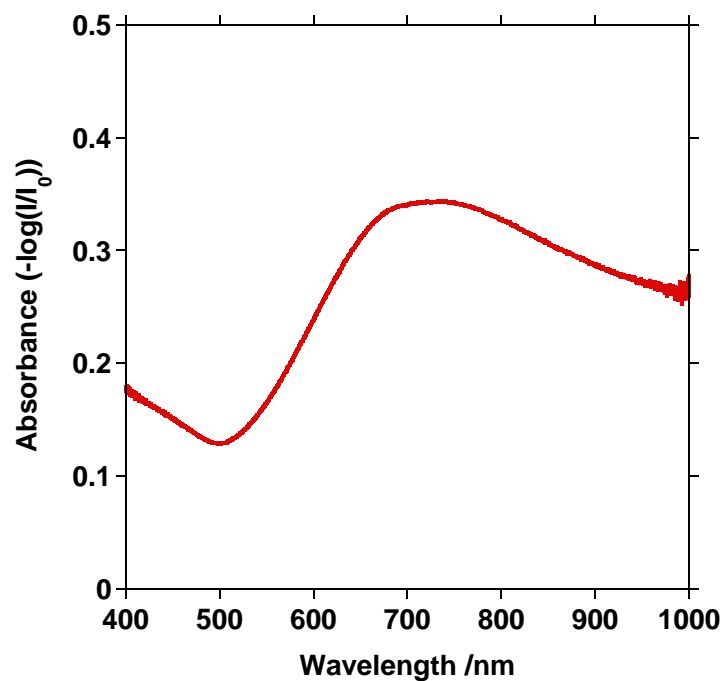
Figure 4-3 Absorption spectrum of the gold nanoisland substrate

SERS spectra were recorded for both DCN and DNO_2, as shown in Figure 4-4. The spectra are easily distinguishable by their characteristic peaks: for DCN, the nitrile stretch is observed at 2240 cm^{-1};[27] for DNO_2, the symmetric NO_2 stretch is observed at 1335 cm^{-1}.[28] This is critical for the potential future studies involving multi-functionalized nanoparticles.
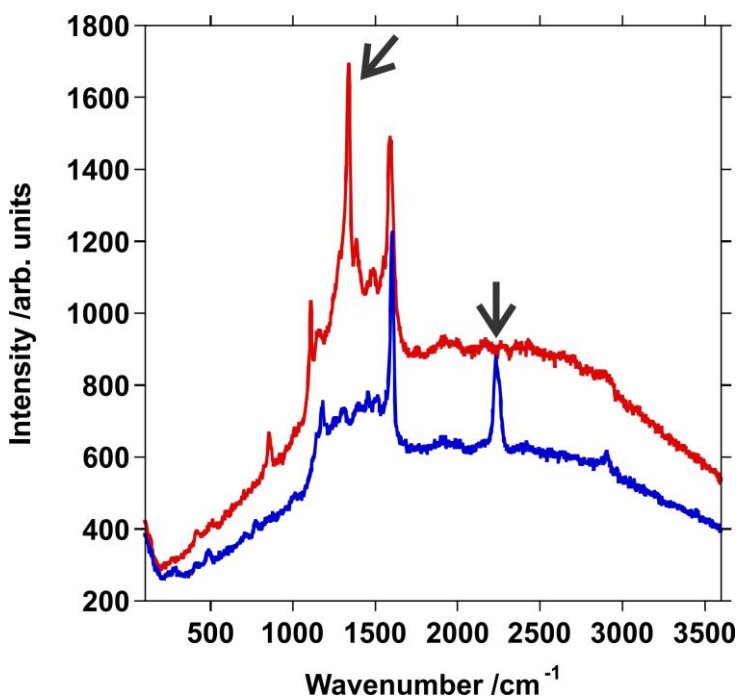
Figure 4-4 Comparison of the SERS spectrum of DCN (blue), indicating the nitrile stretch, and DNO_2 (red), indicating the symmetric NO_2 stretch.

The gold nanoisland substrates were grafted with DCN and DNO_2, through both spontaneous and plasmon-mediated methods, as described in Chapter 3.7. In both instances, the sample was placed in a dish of diazonium salt solution. For plasmon-mediated grafting, the dish was placed under a bright white light; for spontaneous grafting, it was kept in the dark. The functionalization time was kept constant for the methods, in order to compare the efficiency; typically, it was three minutes.

For comparison, SERS spectra were collected for plasmon-mediated *vs*. spontaneously grafted gold nanoislands. Typically, the plasmon-mediated functionalized sample is, at

maximum, a factor of 2-3× more intense than the spontaneously functionalized sample. An example is shown in Figure 4-5. It can be concluded that, although the reaction is plasmon-catalyzed, it spontaneously reacts sufficiently to obtain a decent SERS signal. It is such that the difference between plasmon-mediated and spontaneously grafted areas can be comparable to the difference between different spots on the gold nanoisland substrate, as the random nature of the arrangement of the nanoislands means that the SERS signal intensity is not reproducible over the surface. It may be that there are differences between the plasmon-mediated and spontaneously grafted samples that cannot be probed by SERS, as SERS is highly distance-dependent and can only probe up to a few nanometres.[29,30] Ideally, for use in further applications, the reaction is catalyzed such that there is only substantial grafting localized in the hotspots. To investigate whether the spontaneous grafting observed was concentration dependent, functionalization was performed for concentrations from mM to nM range. As all concentrations showed minimal difference between plasmon-mediated and spontaneous grafting, it was concluded that the effect was not greatly influenced by the concentration, and the original mM concentration was used for further experiments.
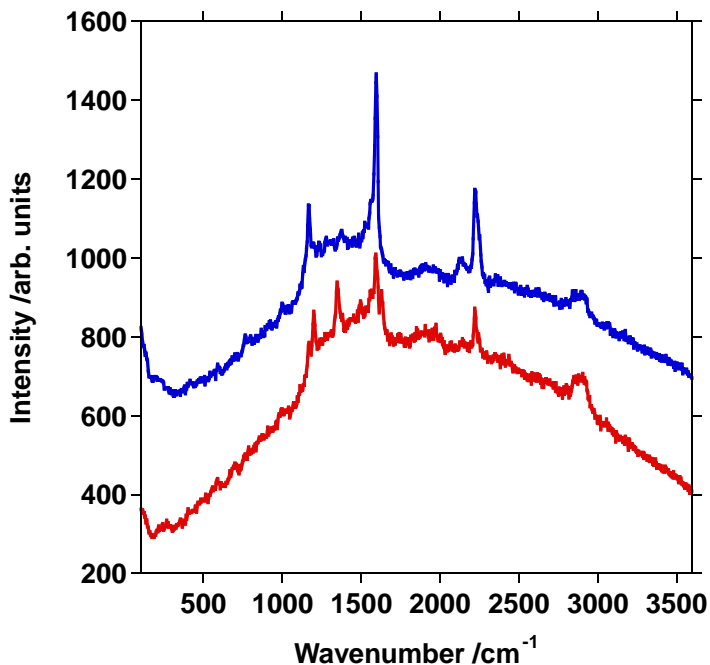
Figure 4-5 Comparison of the SERS spectrum of DCN on gold nanoislands functionalized spontaneously (red) and under plasmon resonance (blue). Spectra have been offset for clarity.

As no great difference was seen in the SERS spectra between spontaneous and plasmon-mediated functionalization, other methods, such as atomic force microscopy (AFM) and scanning electron microscopy (SEM), were selected to evaluate the plasmon-mediated grafting. Additionally, a 632.8 nm laser was used to excite the plasmon resonance, replacing the white light source. With a focused laser, a higher power density is achieved, and the reaction is localized.

Gold nanoislands were functionalized with DNO_2 by focusing a 632.8 nm laser (5.5 mW at the sample) using a $10\times$ (NA 0.25) objective, with a 1 mM solution of the diazonium salt. After exposure, the sample is rinsed with water and ethanol. The sample was investigated using AFM, and material build-up is observed where the laser was focused (Figure 4-6a). The objective was changed from $10\times$ to $40\times$ (NA 0.75), using the same laser and power at the sample. For an exposure of 1.5 minutes, a periodic structure is seen where the laser is focused. This can be seen in the SEM images in Figure 4-6b and 4-6c.
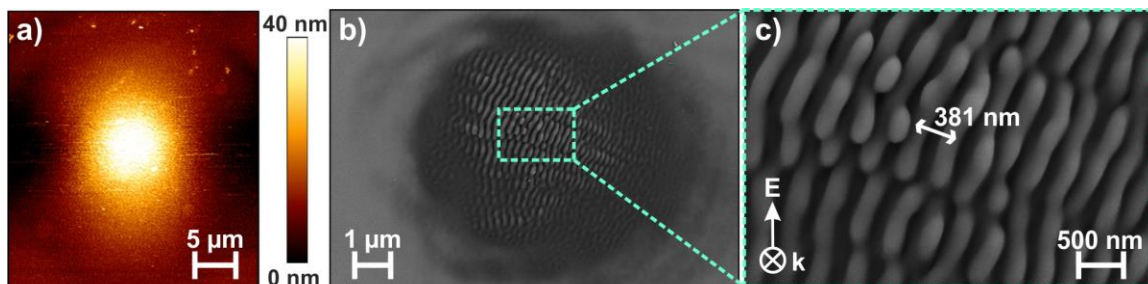
Figure 4-6 a) AFM image of diazonium salt functionalized on gold nanoislands under laser excitation; b) SEM image of a similar spot; c) SEM image of the grating-like structure, showing the spacing.

This periodic structure appears similar to laser-induced periodic surface structures (LIPSS), which can form on almost any material upon irradiation with a beam of sufficient intensity.[31] In LIPSS formation, the pump beam intensity is sufficient to cause a phase change, like melting, and has been observed in many different materials, including semiconductors, metal and dielectrics. Experimentally, the period of the LIPSS depends on the material, the wavelength, and the incident angle:[32]

$$\Lambda = \frac{\lambda}{n(1 \pm \sin \theta)} \tag{4.1}$$

where Λ is the grating period, λ is the excitation wavelength, n is the refractive index of the medium, and θ is the angle of incidence. In most cases, LIPSS involves the formation of ripples parallel to the direction of polarization. Using an excitation of 632.8 nm at normal incidence, and the refractive index for nitrobenzene at 633 nm of 1.5472,[33] the period of the grating is expected to be 409 nm, which roughly matches our experimental observations. Contrary to the observation, however, is the difference in power necessary for the formation of the periodic structure compared to LIPSS formation. Typical LIPSS formation involves pulsed lasers, with power density on the order of ~1 J/cm^2, though it depends on the material;[32,34] here, with a power of several milliwatts over several µm^2 for several minutes, the power needed is about eight orders of magnitude lower than typical LIPSS formation. Therefore, the periodic structures do not

necessarily have the energy as required for LIPSS, but may originate from a similar phenomenon, further amplified by the presence of the nanostructured metal.

A 100× objective (NA 0.90) was used to irradiate the same sample in the presence of the diazonium salt, reducing the spot for plasmon-mediated functionalization to ~1 µm and subsequently increasing the irradiance to ~5 mW/µm². After a long functionalization, mapping for several minutes, no periodic structures are seen, and the nanoislands appear annealed; therefore, further experiments were carried out using the lower magnification objectives. Plasmonic heating is further discussed in Chapter 5.3.
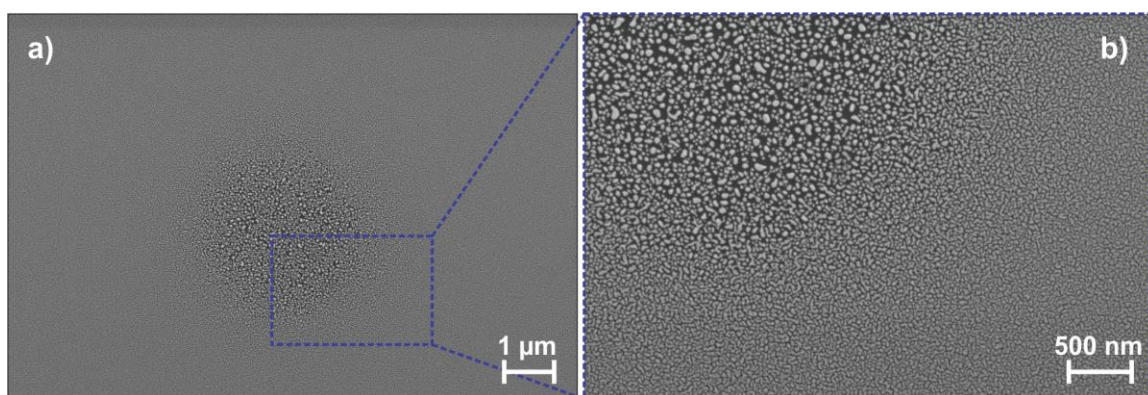
Figure 4-7 a) SEM image of annealed nanoislands under laser irradiation; b) Zoomed in, showing the change in shape of the nanoislands.

4.3.2 Patterned Au Surfaces

In order to better predict the spatial locations of hotspots, gold nanostructures in a regular pattern were also fabricated by nanosphere lithography (NSL). The regular pattern of the nanoprisms allow for better prediction of the localization of the plasmonic hotspots, and thus the regions where plasmon-mediated grafting is expected. This is an advantage over the gold nanoislands, which are of random size and arrangement. An SEM image is shown in Figure 4-8.
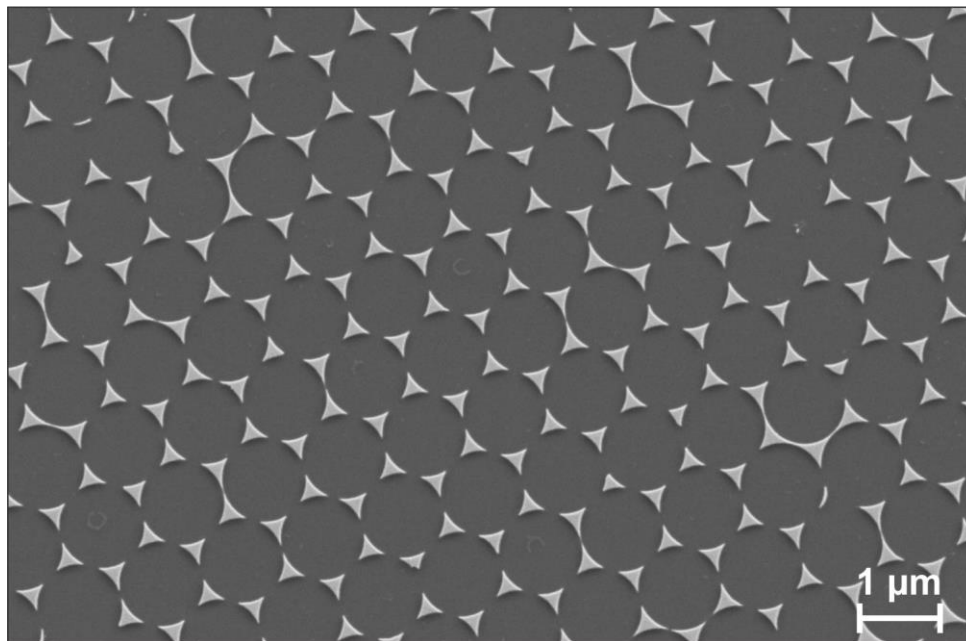
Figure 4-8 SEM image of the gold nanoprism surface, as produced by nanosphere lithography

As for the gold nanoislands, an absorption spectrum was collected, in order to determine the ideal excitation for plasmon-mediated functionalization, and is shown in Figure 4-9. The absorption spectrum shows that a 632.8 nm excitation is also appropriate for the gold NSL sample.
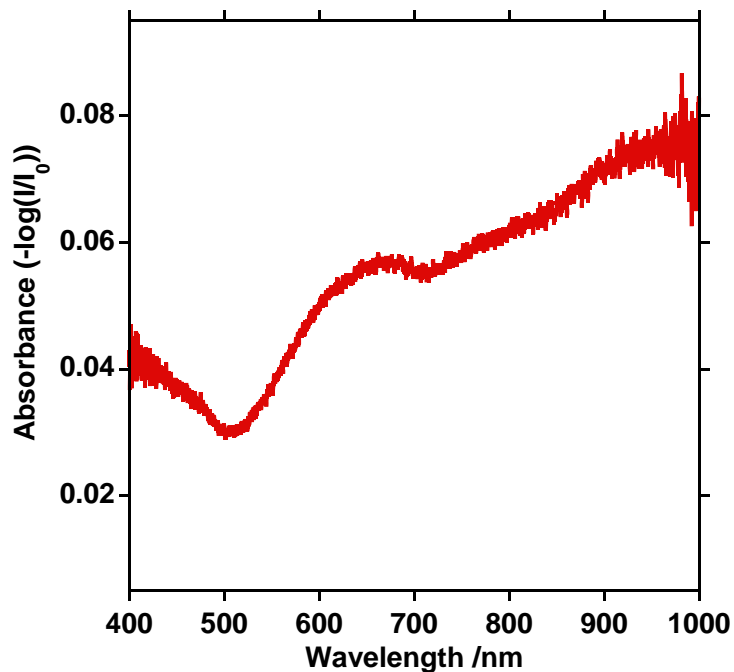
Figure 4-9 Absorption spectrum of the gold nanoprism substrate, as produced by nanosphere lithography

Gold nanoprisms made by NSL were functionalized using a $10\times$ objective, 632.8 nm laser with 0.5 mW of power at the sample for 1.5 minutes. Similar periodic structures are seen after functionalization (Figure 4-10). Near the edge of the periodic structure, the grafting appears more localized to the nanoprisms, as shown in Figure 4-10c. Outside of the focused beam, these areas are subject to lower irradiance under laser excitation; this suggests that a lower laser power, or an unfocused or expanded laser spot, may induce grafting localized to the hotspots of the nanoprisms.
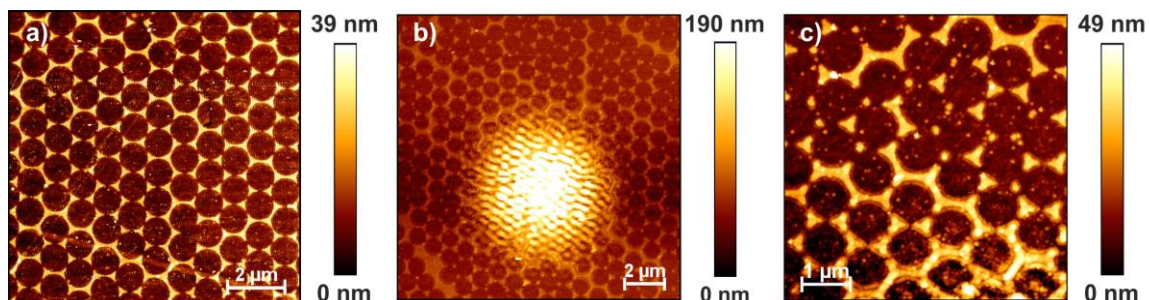
Figure 4-10 AFM images of a) gold nanoprisms, as produced by NSL; b) NSL pattern after functionalization by DNO$_2$ under laser irradiation, showing the formation of periodic structures; c) Functionalized NSL pattern, showing grafting more localized to the nanoprisms.

4.4   Conclusions

In summary, gold nanostructures (gold nanoislands, nanoprisms formed by NSL) were functionalized with 4-nitrobenzenediazonium and 4-cyanobenzene diazonium. As there was only a small difference in the SERS spectra in comparing plasmon-mediated to spontaneous grafting, the grafting was studied using AFM and SEM instead. Under laser excitation, large, periodic structures were observed where the laser beam was focused.

Further investigation of the grafting is necessary to determine the origin of these periodic structures, including determining whether the effect is truly plasmon-mediated or if it is simply photo-induced. For future grafting experiments, there likely exists an intermediate between a white light source, with low irradiance, and a focused laser beam, that will induce localized grafting in the hotspots of the nanostructures. The laser power and exposure time can be optimized to achieve this grafting. When this is achieved, it can be applied to novel nanostructures, and the grafting can be observed as a function of different laser polarization and wavelengths. Further chemical modification of the surface can be exploited for better detection sensitivity.

4.5   References

1.   Zhou, X.; Wenger, J.; Viscomi, F. N.; Le Cunff, L.; Béal, J.; Kochtcheev, S.; Yang, X.; Wiederrecht, G. P.; Colas des Francs, G.; Bisht, A. S.; Jradi, S.;

Caputo, R.; Demir, H. V.; Schaller, R. D.; Plain, J.; Vial, A.; Sun, X. W.; Bachelot, R. *Nano Lett.* **2015**, *15*, 7458-7466.

2. Nguyen, V.-Q.; Ai, Y.; Martin, P.; Lacroix, J.-C. *ACS Omega* **2017**, *2*, 1947-1955.

3. Nguyen, M.; Kherbouche, I.; Gam-Derouich, S.; Ragheb, I.; Lau-Truong, S.; Lamouri, A.; Lévi, G.; Aubard, J.; Decorse, P.; Félidj, N.; Mangeney, C. *Chem. Commun.* **2017**, *53*, 11364-11367.

4. Pinson, J. In *Aryl Diazonium Salts* **2012**, p 1-35.

5. Mesnage, A.; Lefèvre, X.; Jégou, P.; Deniau, G.; Palacin, S. *Langmuir* **2012**, *28*, 11767-11778.

6. Tijunelyte, I.; Kherbouche, I.; Gam-Derouich, S.; Nguyen, M.; Lidgi-Guigui, N.; de la Chapelle, M. L.; Lamouri, A.; Lévi, G.; Aubard, J.; Chevillot-Biraud, A.; Mangeney, C.; Felidj, N. *Nanoscale Horiz.* **2018**, *3*, 53-57.

7. Zhu, S.; Wang, D. *Adv. Energy Mater.* **2017**, *7*, 1700841.

8. Lemos de Souza, M.; Pereira dos Santos, D.; Corio, P. *RSC Adv.* **2018**, *8*, 28753-28762.

9. Zhang, L.; Ding, N.; Lou, L.; Iwasaki, K.; Wu, H.; Luo, Y.; Li, D.; Nakata, K.; Fujishima, A.; Meng, Q. *Adv. Funct. Mater.* **2019**, *29*, 1806774.

10. Boerigter, C.; Aslam, U.; Linic, S. *ACS Nano* **2016**, *10*, 6108-6115.

11. Peng, T.; Miao, J.; Gao, Z.; Zhang, L.; Gao, Y.; Fan, C.; Li, D. *Small* **2018**, *14*, 1703510.

12. Gellé, A.; Jin, T.; de la Garza, L.; Price, G. D.; Besteiro, L. V.; Moores, A. *Chem. Rev.* **2020**, *120*, 986-1041.

13. Jauffred, L.; Samadi, A.; Klingberg, H.; Bendix, P. M.; Oddershede, L. B. *Chem. Rev.* **2019**, *119*, 8087-8130.

14. Baumberg, J. J. *Faraday Discuss.* **2019**, *214*, 501-511.

15. Jain, P. K. *J. Phys. Chem. C* **2019**, *123*, 24347-24351.

16. Sarhan, R. M.; Koopman, W.; Schuetz, R.; Schmid, T.; Liebig, F.; Koetz, J.; Bargheer, M. *Sci. Rep.* **2019**, *9*, 3060.

17. Brongersma, M. L.; Halas, N. J.; Nordlander, P. *Nat. Nanotechnol.* **2015**, *10*, 25-34.

18. Christopher, P.; Moskovits, M. *Annu. Rev. Phys. Chem.* **2017**, *68*, 379-398.

19. Zhan, C.; Chen, X.-J.; Yi, J.; Li, J.-F.; Wu, D.-Y.; Tian, Z.-Q. *Nat. Rev. Chem.* **2018**, *2*, 216-230.

20. Kim, M.; Lin, M.; Son, J.; Xu, H.; Nam, J.-M. *Adv. Opt. Mater.* **2017**, *5*, 1700004.

21. Clavero, C. *Nat. Photonics* **2014**, *8*, 95-103.

22. Govorov, A. O.; Zhang, H.; Gun'ko, Y. K. *J. Phys. Chem. C* **2013**, *117*, 16616-16631.

23. Ding, T.; Mertens, J.; Lombardi, A.; Scherman, O. A.; Baumberg, J. J. *ACS Photonics* **2017**, *4*, 1453-1458.

24. Wang, Y.; Wang, S.; Zhang, S.; Scherman, O. A.; Baumberg, J. J.; Ding, T.; Xu, H. *Nano Res.* **2018**, *11*, 6384-6390.

25. Zhang, Z.; Richard-Lacroix, M.; Deckert, V. *Faraday Discuss.* **2017**, *205*, 213-226.

26. Qiu, J.; Wu, Y.-C.; Wang, Y.-C.; Engelhard, M. H.; McElwee-White, L.; Wei, W. D. *J. Am. Chem. Soc.* **2013**, *135*, 38-41.

27. Muniz-Miranda, M.; Pergolese, B.; Bigotto, A. *J. Phys. Chem. C* **2008**, *112*, 6988-6992.

28. Kim, K.; Choi, J.-Y.; Shin, K. S. *J. Phys. Chem. C* **2014**, *118*, 11397-11403.

29. Kumari, G.; Kandula, J.; Narayana, C. *J. Phys. Chem. C* **2015**, *119*, 20057-20064.

30. Masango, S. S.; Hackler, R. A.; Large, N.; Henry, A.-I.; McAnally, M. O.; Schatz, G. C.; Stair, P. C.; Van Duyne, R. P. *Nano Lett.* **2016**, *16*, 4251-4259.

31. Young, J. F.; Preston, J. S.; van Driel, H. M.; Sipe, J. E. *Phys. Rev. B* **1983**, *27*, 1155-1172.

32. Sakabe, S.; Hashida, M.; Tokita, S.; Namba, S.; Okamuro, K. *Phys. Rev. B* **2009**, *79*, 033409.

33. Kedenburg, S.; Vieweg, M.; Gissibl, T.; Giessen, H. *Opt. Mater. Express* **2012**, *2*, 1588-1611.

34. Li, M.; Lu, Q. H.; Yin, J.; Sui, Y.; Li, G.; Qian, Y.; Wang, Z. G. *Appl. Surf. Sci.* **2002**, *193*, 46-51.

Chapter 5

5 Nanomaterial Heating and Damage as Induced by Plasmon Resonances

Photoinduced heating of nanomaterials has been exploited for applications such as photothermal therapy[1-3] or photothermal-induced polymerization[4,5] through the generation of hot carriers in metals. However, the elevation of temperature in nanostructures is dependent on the opto-geometric parameters used for a given light-structure interaction, which can yield local overheating and damage of the nanostructures. In this chapter, the observation of plasmon-induced "drilling" of nanostructures is described, and potential heating causes are discussed.

5.1 Introduction

In tip-enhanced Raman spectroscopy (TERS), further signal enhancement is achieved when the analyte is placed on a metallic substrate, forming a nanoscale metallic junction between the metallic substrate and the metallic TERS tip. This mode is referred to as gap-mode TERS, and has been used to probe a variety of molecular systems such as small molecules,[6-11] nanostructured materials, and biomaterials.[12-20] In the transmission geometry, the excitation laser must first pass through the metallic substrate to reach the analyte and the TERS tip. The metallic substrate must be atomically flat, reducing parasitic scattering processes, and thin enough to essentially be optically transparent. Previous studies have been focused on the use of gold nanoplates as substrates, as these exhibit the required attributes and are chemically stable.[8,10,16-18,20,21] The use of silver nanoplates with silver TERS tips has been marginally reported, presumably due to the poor chemical stability of silver.[12,13]

Here, we have synthesized silver nanoplates (as described in Chapter 3.6.1) for use in gap-mode TERS with a gold-coated TERS tip, in order to compare the resultant enhancement of the common gold-silver and gold-gold substrate-tip configurations. After observation of a TERS signal, the nanoplate appears locally ablated, and the

possible origin of plasmon-mediated damage is investigated, given the weak irradiance conditions in TERS.

5.2 Plasmon-Mediated Drilling of Silver Nanoplates

For gap-mode TERS experiments using an inverted optical microscope, the metallic nanoplate should exhibit a high width/thickness aspect ratio with minimal surface roughness. Large lateral dimensions of the nanoplates, on the order of several microns, facilitate their observation under an optical microscope, whilst being thin enough for the laser to penetrate through the nanoplate and reach the metal tip without too much loss of intensity of the incident laser. Protocols for the synthesis of gold nanoplates that meet these requirements have been well established.[22,23] Conversely, the synthetic approaches to preparing silver nanoplates often yield smaller nanoplates with side lengths less than 500 nm, making them less ideal for gap-mode TERS applications. In this study, silver nanoplates were synthesized based on a seed-mediated method developed by Zhang *et al.,* as previously described in Chapter 3.6.1.[24] As can be seen in the scanning electron microscopy (SEM) image of Figure 5-1a, the resulting nanoplates of the seed-mediated synthesis are large, with a distribution in size ranging between two to six microns in side length. The prepared silver nanoplates were commonly found to be triangular or truncated triangles, as shown in Figure 5-1a. To determine the thickness of the nanoplates, atomic force microscopy (AFM) scans were performed. The inset of Figure 5-1a shows a representative AFM image of a silver nanoplate with the corresponding cross-section in Figure 5-1b. Here, the thickness of the nanoplates was found to vary from 40 – 60 nm, and that the surface exhibits an RMS roughness on the order of several nanometers, compared to about 500 pm for gold nanoplates.[8]
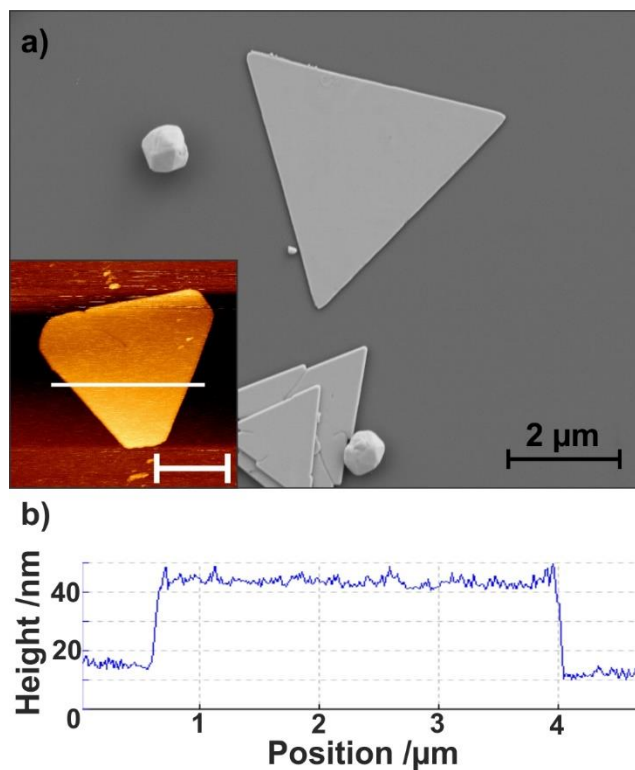
Figure 5-1 a) SEM of silver nanoplates, with representative AFM image inset, with scale bar of 2 μm; b) Cross-section of nanoplate along white line as indicated in the inset of a).

The absorbance spectrum of the silver nanoplates was measured and can be seen in Figure 5-2. It shows an absorption of 1.3 at 632.8 nm for a ~35-40 nm thick plate. The as-prepared nanoplates often stack (Figure 5-1a), or have smaller nanostructures, such as multifaceted nanoparticles, on their surfaces; however, clean, isolated silver plates can be found and used for the TERS experiments.
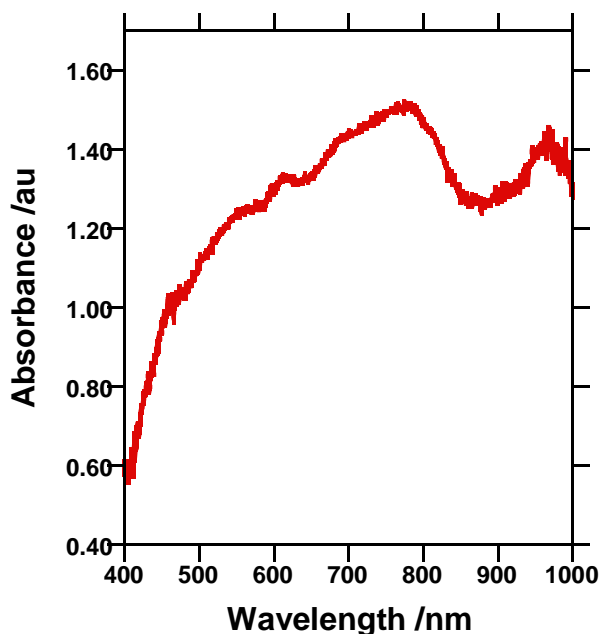
Figure 5-2 Absorbance spectrum of silver nanoplates

Prior to performing tip-enhanced measurements, the surface of the nanoplate was functionalized with a monolayer of 4-mercaptophenylboronic acid (4-MPBA). Figure 5-3a shows an AFM scan of a functionalized nanoplate with an intrinsically rough surface, but without other particles or plates present. The nanoplates as synthesized do provide SERS activity, as shown in Figure 5-3b, where the SERS spectrum has been multiplied by a factor of 10. This is likely due to the rough surface of the nanoplates, as the nanoscale roughness can support hotspots. As a linearly polarized laser was used in an axial geometry, the tip was localized slightly off-centre of the focused laser beam to benefit from the z-component of the tightly focused beam. To collect the TERS measurements, the tip was approached to the centre of the triangular nanoplate to minimize any effects from the edges of the nanoplates. Due to the thickness of the nanoplates, a laser intensity of 1 mW was used, as lower laser power (i.e. 100 µW) did not allow for collection of a TERS signal. Considering the thickness of the nanoplate (i.e. ~40 nm), the effective power is ~33 µW at the sample, which is focused by the 100×, 0.9 NA objective. To differentiate the TERS and SERS contributions, a collection of spectra was collected at increasing tip-sample distances, from 0 nm (tip engaged) to 500 nm with varying step sizes, and the results are shown in Figure 5-3b. When the tip is at

the surface of the nanoplate, the electromagnetic enhancement offered by the tip is able to locally enhance the Raman spectrum of the 4-MPBA molecules adsorbed on the Ag nanoplate. As the tip is retracted from the surface, the signal decays, but not completely. Instead, the signal from a tip retracted 500 nm above the nanoplate surface is more intense than the reference SERS spectrum collected on flat nanoplates without any TERS tip. To ascertain the origin of this increase in signal, a post-TERS AFM scan was performed (Figure 5-3c). The scan clearly shows that the centre of the nanoplate has been "drilled", with considerable additional roughness having been introduced around the ablated area. This deformation has amplified the SERS effect through an increase of the localized roughness, as shown in the AFM topography (Figure 5-3c).
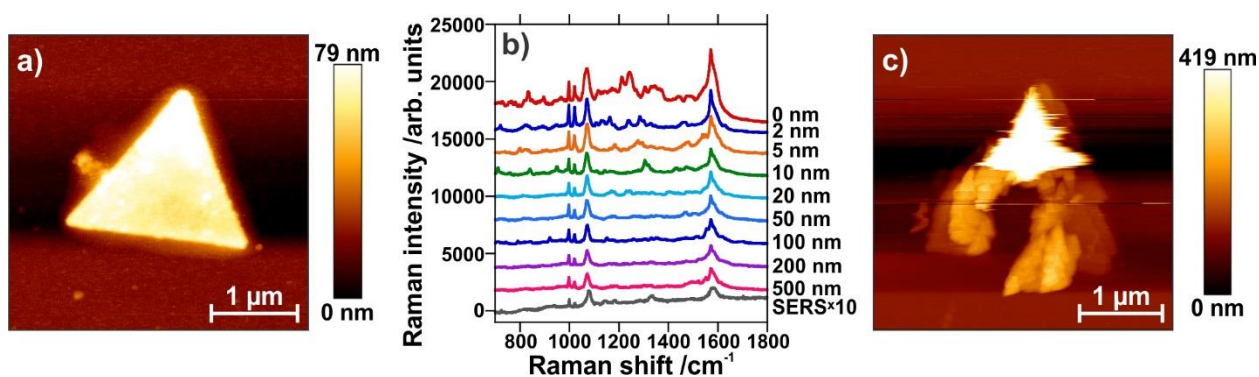
Figure 5-3 a) AFM image of silver nanoplate; b) TERS spectra obtained upon increasing the tip-sample distance, as indicated, compared to the SERS spectrum (multiplied by 10). Spectra have been offset for clarity. c) AFM image of silver nanoplate after TERS experiment.

To determine if this drilling effect is facilitated by the presence of an adsorbed molecule, the same process was repeated on a bare nanoplate (Figure 5-4a). Once again, after the tip-enhanced measurements were performed, deformation of the nanoplate was observed, and as shown in Figure 5-4b, is sufficiently large to be seen optically under a microscope.
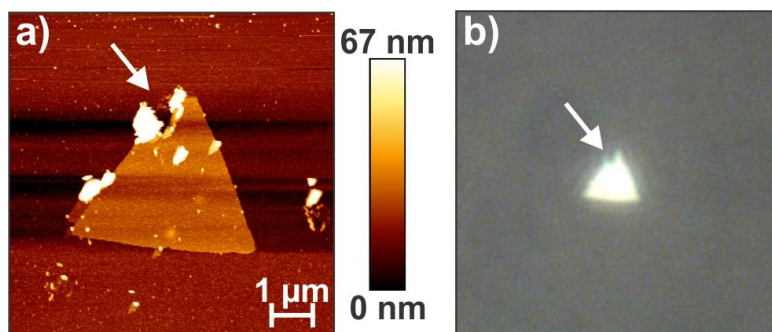
Figure 5-4 a) AFM image of a non-functionalized drilled silver nanoplate, with the arrow indicating damage; b) Optical image of the same nanoplate, with the arrow indicating the same point.

To further investigate the cause of this localized destruction, a TERS experiment was performed under optical misalignment, where the tip was placed on the edge of the focused laser focal plane. Under such a configuration, little to no electromagnetic enhancement at the tip apex should be present. As depicted in Figure 5-5a and 5-5b, selected points for spectral collection were chosen on and off the nanoplate. Under the misaligned conditions, no TERS spectra of the adsorbed molecule could be collected (Figure 5-5c). However, there is some silicon and 4-MPBA contributions, as shown in Figure 5-4c, since the tip is still in the vicinity of the focal point. As the irradiation time for this experiment was significantly shorter (by more than a minute) than that used in Figure 5-3, the sample was exposed to the laser for an additional five minutes to determine if the nanoplate had been damaged by laser-induced heating. The post-irradiation AFM scan (Figure 5-5d) did not exhibit any damage. To verify that the nanoplate was not impervious to drilling, the tip and laser were realigned to be in an ideal TERS configuration. Spectra were collected on and off the nanoplate in aligned conditions (red and blue dots, Figure 5-5a). When the tip is away from the nanoplate, spectral features of 4-MPBA and the silicon second-order transverse optical phonon mode from the tip can be observed. The 4-MPBA contribution is presumably coming from the presence of 4-MPBA at the surface of glass, while the silicon peak is coming from the AFM tip. Importantly, Figure 5-5e highlights that the system is well aligned, as shown by the intense contribution of 4-MPBA over the nanoplate compared to the

contamination seen in the spectrum collected off the nanoplate. Ten further spectra were collected in the centre of the nanoplate, at varying tip-sample distances. Additional single point measurements were collected at other positions on the nanoplate (Figure 5-5b). After collection of the TERS spectra in the selected areas, the AFM tip was changed to a new, non-coated tip, and a subsequent AFM scan was acquired (Figure 5-5f). Once again, local damage was observed in the exact position where the spectra were collected. The defects exhibit two critical structural components. Firstly, in the region that was irradiated over a longer period (barycentre of the triangle), the degree of damage is considerably greater than that of the areas where single TERS measurements were performed. Furthermore, regardless of the exposure time, the defects adapt a triangular shape, similar to that of the AFM tip. As the positions and relative sizes of the holes can be readily changed based on the TERS experiments, this approach could be used to pattern nanostructures through localized metal ablation.
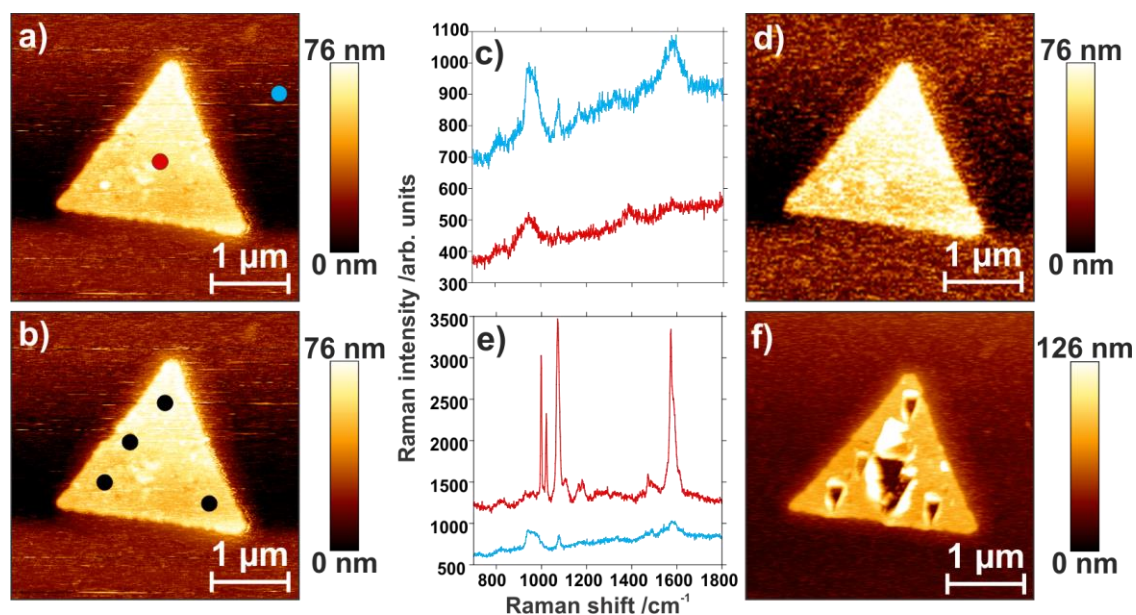
Figure 5-5 AFM images of a silver nanoplate, showing a) points at which spectra were collected on (red) and off (blue) the nanoplate, and b) other points of collection. c) No TERS signal is measured off alignment, resulting in d) no damage to the nanoplate. e) TERS spectrum is measured on the nanoplate (red), resulting in f) damage to the nanoplate, at the points as shown in a) and b).

Time-lapse series of experiments were conducted to monitor the 4-MPBA Raman spectral changes over irradiation time (Figure 5-6). Noticeable spectral changes such as weaker intensity and spectral profile changes are observed for spectra collected after a longer irradiation time, highlighting the onset of the structural damages to the Ag nanoplate.
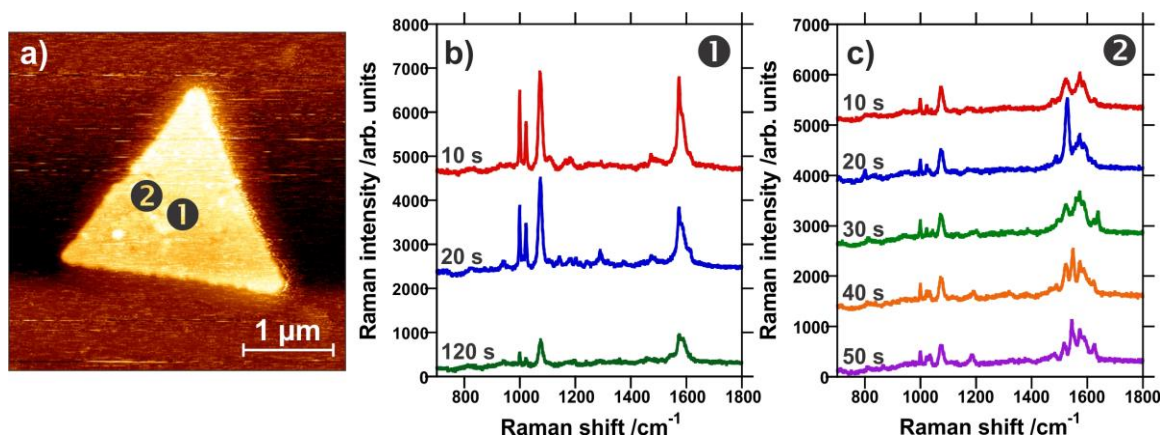
Figure 5-6 a) AFM images showing two distinct points (1) and (2) chosen for time lapse experiments; b) Series of three spectra collected under continuous irradiation on point 1 after irradiation of 10, 20 and 120 s. The Au-coated tip was new; c) Series of 5 spectra collected on point (2) after irradiation of 10, 20, 30, 40, 50 s. The Au coated tip was used to conduct the experiments in point (1).

Overall, these observations indicate that under an ideal TERS configuration, the TERS tip can induce significant damage on a metallic surface, and can be used to drill triangular holes into the nanoplates. As metallic nanoplates are commonly used in gap-mode TERS measurements, the source of this nanoscale surface ablation was further investigated. Possible causes of this drilling are multiple and can presumably be assigned to i) mechanical damage from the tip; ii) plasmonic heating; iii) a plasmon-mediated chemical or electrochemical reaction; or iv) some combination of these processes. As mentioned earlier, no hole generation was observed when the laser was not focused on the tip. Since pseudo-TERS measurements were performed (single point and tip-retraction), it is unlikely that mechanical damage is the cause, despite the triangular shape matching that of the metallized AFM tips. Furthermore, under prolonged irradiation with this

configuration, no damage was observed. This means that laser heating from a far-field focused beam alone is insufficient to drive this process, and that the presence of the tip at the focal point of the laser is necessary to induce local damage. The excitation source was set at 632.8 nm, and since the plasmon excitation is quite weak at this wavelength, this may exclude thermal effects in these experimental conditions. This does not preclude the possibility of heating due to the plasmonic resonance of the tip. As such, we focus here on the effect of an ideal TERS configuration, where the metallized tip is aligned with the laser.

5.3   Plasmonic Heating and Nanostructure Annealing

Optical confinement of the electric field in small volumes of metal nanoparticles results in plasmonic heating.[25,26] This heating has been exploited, among other uses, for cancer phototherapy[1-3] and molecular delivery.[27,28] Plasmonic heating can be sufficient to vaporize the surrounding medium,[29,30] or under intense continuous wave sources,[31] or pulsed lasers,[32] locally melt the nanoparticle. Previous studies have shown plasmonic heating to adversely affect the SERS spectra, as molecules are desorbed or nanoparticles are damaged.[33,34]

5.3.1 Hot Electron Generation *vs.* Plasmonic Heating

In plasmon-mediated reactions, an increased rate of reaction is observed, owing to either or both plasmonic heating and hot electron generation. There has been recent debate on which factor contributes more to enhanced reaction rates, and is still a topic of great interest.[35-37] It is therefore desirable to decouple these two mechanisms. In theory, this can be done by reproducing an experiment in the dark, under appropriate heating, but without plasmon excitation, and comparing the rate of reaction, if any. The difficulty in doing so involves accurately determining the temperatures achieved in plasmonic heating.

Temperatures in nanostructured systems are often measured through the injection of nanoprobes, such as fluorescent probes and quantum dots,[38,39] or through changes in the surroundings, by phase transitions of lipid bilayers.[40] These techniques are largely unsuited for temperature measurements in plasmon-mediated reactions, due to the

potential interference of the probes on the reaction. Experimentally, the temperature is sometimes measured by Raman thermometry, where the ratio of the intensities of the anti-Stokes and Stokes scattering peaks is obtained and the local temperature is extracted (following the Boltzmann distribution, equation 2.1).[34,36,41] When such measurements are not possible under the given reaction conditions, the temperature is estimated through simulations, often followed by bulk measurements of the temperature, when the reaction occurs in solution.[1]

5.3.2 Mechanism of Plasmonic Heating

The main source of heating during plasmon decay is Joule heating, resistive heating in a conductor. Within a picosecond of excitation, hot electrons have redistributed their energy to lattice phonons. Subsequently, the heated lattice undergoes phonon-phonon coupling to exchange energy with the surrounding medium.[42] This heat transfer can be written as:[26,43]

$$\rho C_p \frac{\partial T(\boldsymbol{r})}{\partial t} = \nabla \cdot [\kappa \nabla T(\boldsymbol{r})] + Q \tag{5.1}$$

where ρ is the density, C_p is the specific heat capacity at constant pressure, $T(r)$ is the absolute temperature, κ is the thermal conductivity, and Q is the external source of heat: in this case, the amount of heat produced per unit time and volume, originating mainly from Joule heating in the nanostructure. By Poynting's theorem, this can be written:[26]

$$Q = \iiint q_{EM} dV \tag{5.2}$$

where V is the volume and $q_{EM} = \frac{1}{2} Re(\boldsymbol{J} \cdot \boldsymbol{E}^*)$ is the electromagnetic power loss density, with $\boldsymbol{J} = \sigma \boldsymbol{E}$ the current density inside the nanoparticle as a function of the conductivity σ and electric field $\boldsymbol{E}$. Therefore, in order calculate the heat production, the electric field inside the nanoparticle must be determined. This can be calculated through Maxwell's equations (equation 3.1). Most commonly, this is done through modelling the electric field and resultant heat transfer using FEM.[26] For small spherical nanoparticles of radius R, it can be shown that:[44]

$$\Delta T(r) = \frac{\sigma_{abs} I_0}{4\pi\kappa r}, \qquad r > R \qquad\qquad (\mathbf{5.3})$$

where $\Delta T(r)$ is the temperature increase, σ_{abs} is the absorption cross-section of the nanoparticle, I_0 is the intensity of the incident light, and r is the distance from the surface of the nanostructure. This can be extended for non-spherical particles through the use of a correction factor β:[43]

$$\Delta T(r) = \frac{\sigma_{abs} I_0}{4\pi\kappa R_{eff}\beta} \qquad\qquad (\mathbf{5.4})$$

with R_{eff} as the effective radius of the nanoparticle.

5.3.3 Magnitude of Photoinduced Heating

As described by equation 5.3, the degree of heating is influenced by the incident light (I_0), the surrounding medium (κ), and the optical properties of the metal nanoparticle (C_{abs}) as determined by the size and shape of the nanoparticle, and the identity of the metal. There are many studies investigating different nanostructures and optimizing their opto-geometric properties using the finite element method (FEM): geometries such as nanospheres, nanorods, nanocages, and nanostars.[26,33,45] Depending on these factors, temperature increases achieved through plasmonic heating range from several K to hundreds of degrees.[26,34,46] Locally, this has been shown to form a vapor layer around the nanoparticle above $T = 200$ °C.[29]

Bulk materials have a much higher melting point than their nanostructured materials. Melting and reshaping of gold nanorods has been shown to occur at temperatures as low as 200 °C, while bulk gold has a melting point of 1064 °C.[47] Thermal annealing of gold nanospheres causes structural changes after 200 °C.[48] Nanostructures with finer features, such as nanostars, are expected to have a lower melting temperature.[26]

Here, the temperature is calculated using FEM, and compared to similar simulations of heating in TERS, as the extended tip structure may influences heating effects compared to single nanoparticle studies.

5.3.4 Modelling of Heating in Tip-Enhanced Raman Spectroscopy

To investigate the heating of the tip, finite element method (FEM) calculations were performed to evaluate the temperature gradient in the vicinity of the tip-nanoplate assembly. The geometry and material properties were set to match the experiment, with the laser linearly polarized and propagating along the tip axis. The power of the laser source was 1 mW before the nanoplate. The normalized electric field was calculated for a tip-sample separation of 2 nm, as shown in Figure 5-7a. The corresponding temperature change is reported in Figure 5-7b.
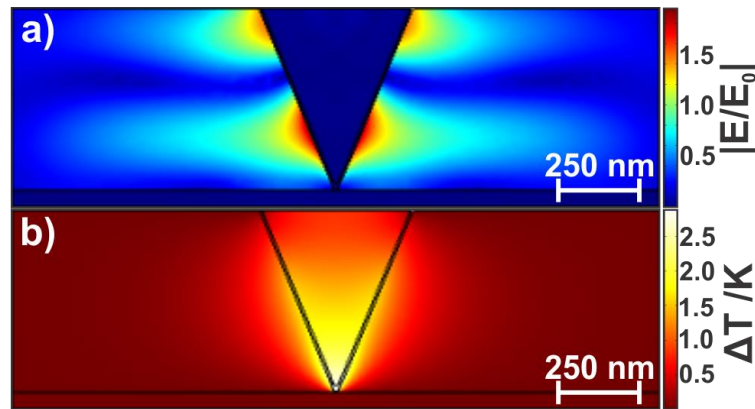
Figure 5-7 a) Electric field in the plane of polarization, with 2 nm between the TERS tip and the silver nanoplate; b) Resultant temperature increase.

For a tightly focused Gaussian beam in transmission geometry polarized along the x-direction, there is a component of the electric field along the tip axis:[49]

$$E_z = ik_0 \frac{\partial E_x}{\partial x} \tag{5.5}$$

where E_x and E_z are the x-and z-components of the electric field, respectively; i is the imaginary unit; and k_0 is wavevector of the incident wave. However, it is difficult to ascertain the exact value of this component in a real system. To determine the maximum electric field, and thus the maximum heating expected, the case where the laser is polarized along the tip axis with a side illumination geometry is also calculated (Figure 5-8).
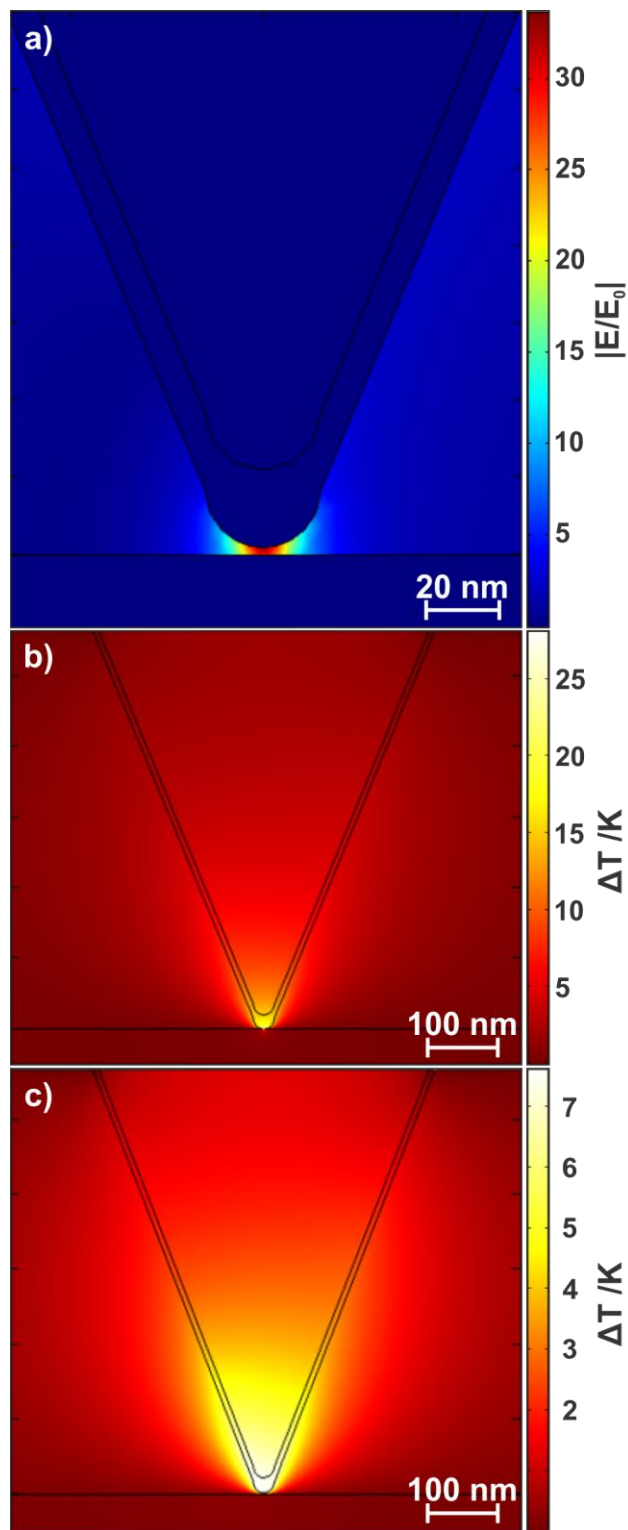
Figure 5-8 a) Electric field at tip, with the laser polarized along the tip axis; b) Temperature rise at tip-sample contact; c) Temperature rise at a tip-sample distance of 2 nm.

This result for the electric field calculation (Figure 5-7a) is consistent with previous results.[50,51] The resultant weak temperature increase, limited to about 2 K as shown in Figure 5-7b, is comparable to the work of Balois *et al.*, who have predicted an increase of several degrees under 50 µW plane wave side illumination with a gold tip-gold substrate junction.[50] Other work from Downes *et al.* predicts a much larger temperature increase, up to $\Delta T = 360$ K in the gold tip-silver substrate junction at 533 nm using side illumination;[52] in comparison, the reciprocal metal configuration (Ag tip and Au substrate) illuminated at 633 nm increases by only 30 K under the same irradiance conditions of 1 mW/µm^2.[46] Differences between these results and ours can be attributed to distinct excitation wavelengths and geometry. More specifically, in the backscattering configuration that we have used for our experiment and modelling, it is likely that the metal substrate has decreased the laser intensity reaching the tip, leading to limited heating at the tip apex as observed in Figure 5-7b. As shown in Figure 5-8, polarization along the tip axis yields a higher temperature increase of ΔT ~25 K but, to reiterate, the difference between our study and that of Downes *et al.* is their illumination with 532 nm compared to our excitation with 632.8 nm, as both calculations were conducted with irradiances of 1 mW/µm^2. The FEM simulations show that the calculated temperatures at the tip-substrate junction are insufficient to cause drastic damage to the nanoplates.

5.4 Analysis by Energy-Dispersive X-Ray Spectroscopy

To further investigate the role of the tip in the nanoplate drilling, the TERS tip was investigated under SEM and energy-dispersive X-ray (EDX) spectroscopy. SEM images were first obtained for a pristine TERS tip. A tip coated at the same time as the pristine tip was used for the TERS experiment. The tip selected for EDX measurements was minimally used. In this instance, the laser was focused on the nanoplate. When the tip was raster scanned over the nanoplate during the laser-tip alignment, the tip drilled a hole near the middle of the nanoplate (Figure 5-9). As this tip was not in the focal spot of the laser for only a few seconds, and was in motion during this time, plasmon-induced heating was minimized.
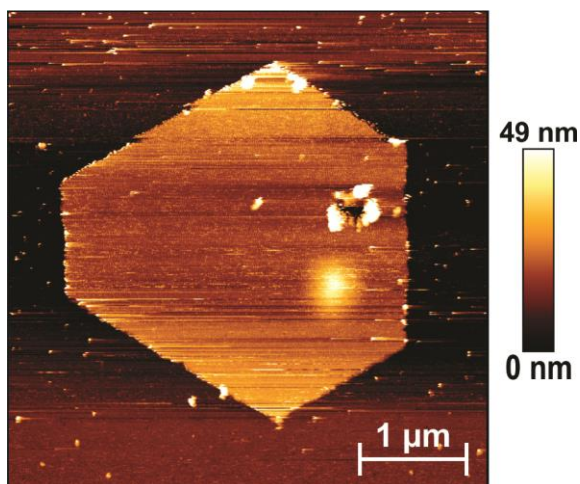
Figure 5-9 Atomic force micrograph of drilled silver nanoplate corresponding to the tip examined by EDX.

The SEM images of the pristine tip are shown in Figure 5-10a and 5-10 b. Figure 5-10c and 5-10d show the damage to the tip after the TERS experiment. As seen in Figure 5-10d, the gold layer is delaminated from the tip, revealing the silicon that constitutes the bulk of the tip. There are two distinct sections chosen for EDX measurement, just below and above the tip apex, as highlighted in Figure 5-6d. In the area above the tip apex, EDX measurements show the expected gold and silicon (Figure 5-10e): this section is the gold layer, ripped away from the tip during alignment. On the lower section, contribution from silver are also seen (Figure 5-10f). A small contribution from aluminum is observed (Figure 5-10f), but belongs to the background noise, since no contrast could be seen in the aluminum EDX map.
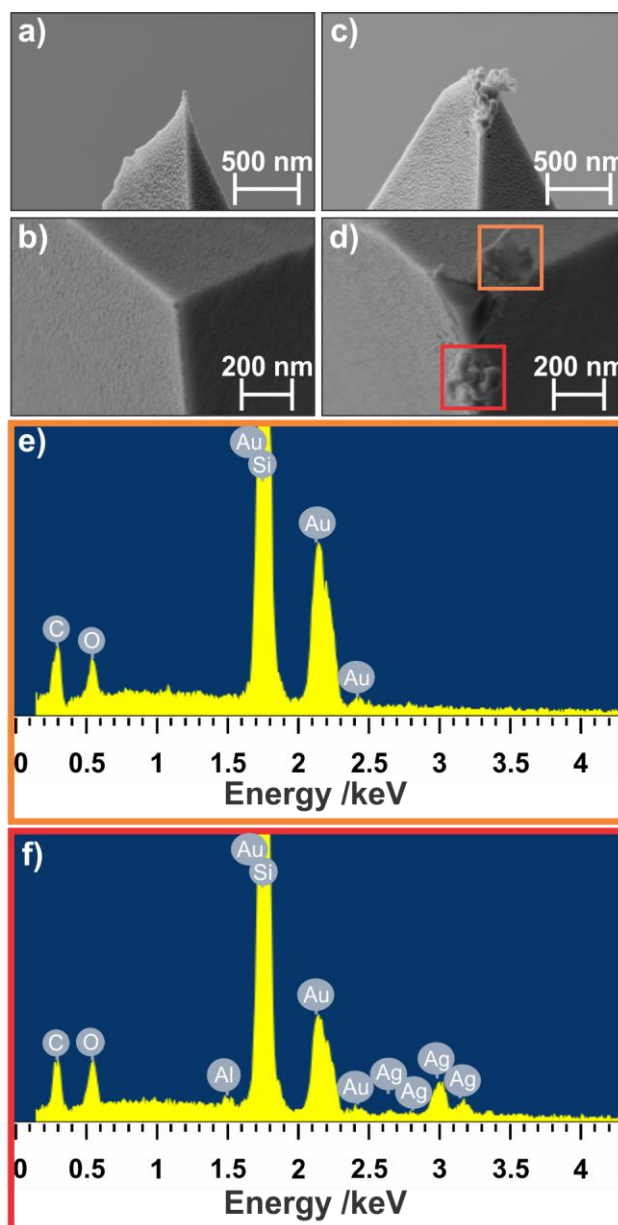
Figure 5-10 SEM images of a, b) a pristine TERS tip; c) a TERS tip after silver nanoplate drilling, indicating d) areas at which EDX spectra were collected. e), f) Corresponding EDX spectra.

Maps showing the distribution of each element of interest were also acquired, correlating to the SEM of the damaged tip (Figure 5-11a). The gold map, in Figure 5-11b, shows gold in all undamaged areas of the tip, but not the exposed silicon or the area below the tip apex. Conversely, the silicon map shows the highest signal in the area exposed

(Figure 5-11c), is also present under the undamaged layer of gold, but no signal is seen in the area below the tip apex. The map of silver shows only a presence in the area below the tip apex (Figure 5-11d). Gold and silicon are also likely present under the tip apex, but are shielded by the silver structure.
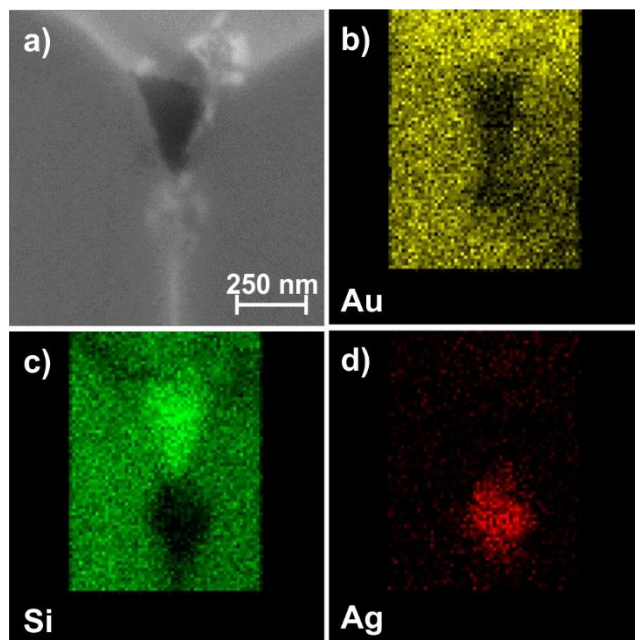
Figure 5-11 a) SEM image of a TERS tip after drilling; EDX maps of b) gold; c) silicon; d) silver.

5.4.1 Plasmon-Mediated Reaction

The presence of amorphous silver on the TERS tip suggests silver species are transferred from the nanoplate to the tip by a plasmon-mediated reaction. Such reactions are triggered by the combination of the locally enhanced electric field and the presence of hot electrons, highly energetic electrons that are the result of non-radiative plasmon decay. The generation of hot electrons has been described for both silver and gold nanostructures. To further understand the relationship between TERS and hot-electron generation, it is necessary to compare our configuration to other gap-mode TERS experiments.

Typically, gap-mode TERS experiments employ the use of gold nanoplates. For the resulting tip-plate junctions (gold-gold, silver-gold), to the best of our knowledge, no

previous studies have demonstrated deformation of the nanoplate after TERS measurements to the degree we have shown and under modest irradiation conditions. The use of a silver nanoplate with a gold tip is likely the driving force behind the ablation of the nanoplate. Here, we surmise that two factors either individually or in combination, yield the changes to the structure of the nanoplate. It has been shown the citrate can be oxidized by hot holes; electrons released from this oxidation can then reduce Ag^+ ions.[53] Under different conditions, Ag^+ can be reduced directly by hot electrons.[54] The transfer of the hot electrons from the tip to the nanoplate can be aided by the layer of atmospheric water at the tip-substrate interface, or from the direct contact between the tip and nanoplate during measurement. As citrate is used in the synthesis of the nanoplates described in this study, it is possible that even after functionalization with 4-MPBA, some citrate remains on the surface. Citrate residues have been observed in the TERS spectrum, at 1400 cm^{-1}, as shown in Figure 5-12.[55-57]
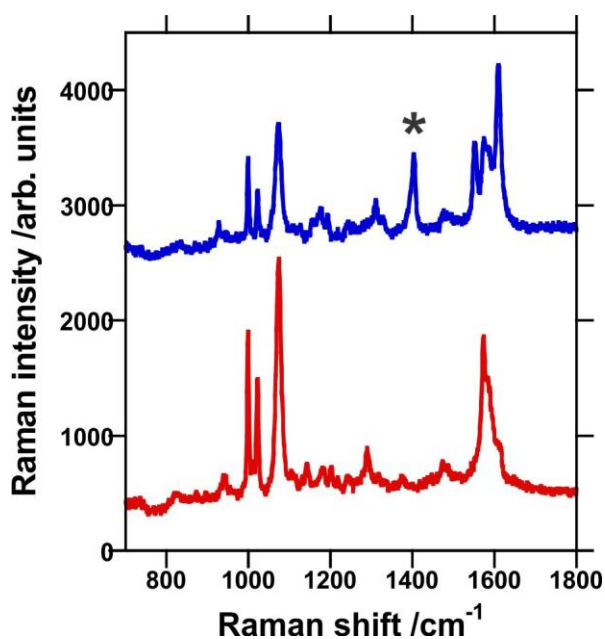
Figure 5-12 Comparison of a TERS spectra including citrate (blue) to a typical TERS spectrum of 4-MPBA (red). Spectra have been offset for clarity.

It is known that coating a surface with a thin layer of SiO_2 can prevent hot electrons from reaching or escaping the surface.[58] However, in the case of coating the metal tip with such a layer, we have previously shown that this diminishes the EM enhancement and the

resulting TERS compatibility of the tip.[51] As the use of silver nanoplates with gap-mode TERS is limited,[12,13] it is difficult to ascertain if this effect occurs exclusively with silver nanoplates. In those described works, a silver tip was used in conjunction with the silver plates; however, we employ the use of a gold tip as opposed to a silver tip. As our conditions use a heterometallic junction, the hot electron generated by the gold tip could reduce surface silver species onto the tip, potentially when the tip makes contact with the surface. The triangular geometry of the resulting hole is related to the direction of the hot electron coming off of the tetrahedral tip.

5.5   Conclusions

In summary, silver nanoplates were synthesized by the seed-mediated method for use as substrates for gap-mode TERS experiments. During both the alignment process and the collection of TERS spectra, nanoscale holes with a triangular shape were ablated in the nanoplate when the tip was aligned with the laser. Using FEM calculations, we investigated the role of plasmon-induced heating and determined that the elevation in temperature at the junction between the tip and nanoplate was not enough to account for the surface damage. EDX measurements of a tip used to generate the triangular nanoholes showed the presence of silver on the tip, making the reduction of silver species from the nanoplate onto the tip a likely cause of this nanoplate drilling. Further investigations to determine the exact trigger of this process could provide greater insight into plasmon-mediated chemical reactions, especially when they can be controlled with nanoscale precision.

5.6   References

1.   Ayala-Orozco, C.; Urban, C.; Knight, M. W.; Urban, A. S.; Neumann, O.; Bishnoi, S. W.; Mukherjee, S.; Goodman, A. M.; Charron, H.; Mitchell, T.; Shea, M.; Roy, R.; Nanda, S.; Schiff, R.; Halas, N. J.; Joshi, A. *ACS Nano* **2014**, *8*, 6372-6381.

2.   Lal, S.; Clare, S. E.; Halas, N. J. *Acc. Chem. Res.* **2008**, *41*, 1842-1851.

3.   Ricciardi, L.; Sancey, L.; Palermo, G.; Termine, R.; De Luca, A.; Szerb, E. I.; Aiello, I.; Ghedini, M.; Strangi, G.; La Deda, M. *Nanoscale* **2017**, *9*, 19279-19289.

4.   Jiang, J.; Ye, G.; Lorandi, F.; Liu, Z.; Liu, Y.; Hu, T.; Chen, J.; Lu, Y.; Matyjaszewski, K. *Angew. Chem. Int. Ed.* **2019**, *58*, 12096-12101.

5.   Maity, S.; Wu, W.-C.; Xu, C.; Tracy, J. B.; Gundogdu, K.; Bochinski, J. R.; Clarke, L. I. *Nanoscale* **2014**, *6*, 15236-15247.

6.   Awada, C.; Plathier, J.; Dab, C.; Charra, F.; Douillard, L.; Ruediger, A. *Phys. Chem. Chem. Phys.* **2016**, *18*, 9405-9411.

7.   Kumar, N.; Stephanidis, B.; Zenobi, R.; Wain, A. J.; Roy, D. *Nanoscale* **2015**, *7*, 7133-7137.

8.   Pashaee, F.; Hou, R.; Gobbo, P.; Workentin, M. S.; Lagugné-Labarthet, F. *J. Phys. Chem. C* **2013**, *117*, 15639-15646.

9.   Stadler, J.; Oswald, B.; Schmid, T.; Zenobi, R. *J. Raman Spectrosc.* **2013**, *44*, 227-233.

10.   van Schrojenstein Lantman, E. M.; Deckert-Gaudig, T.; Mank, A. J. G.; Deckert, V.; Weckhuysen, B. M. *Nat. Nanotechnol.* **2012**, *7*, 583-586.

11.   Yang, M.; Mattei, M. S.; Cherqui, C. R.; Chen, X.; Van Duyne, R. P.; Schatz, G. C. *Nano Lett.* **2019**, *19*, 7309-7316.

12.   Deckert-Gaudig, T.; Deckert, V. *J. Raman Spectrosc.* **2009**, *40*, 1446-1451.

13.   Deckert-Gaudig, T.; Erver, F.; Deckert, V. *Langmuir* **2009**, *25*, 6032-6034.

14.   Alexander, K. D.; Schultz, Z. D. *Anal. Chem.* **2012**, *84*, 7408-7414.

15.   Blum, C.; Schmid, T.; Opilik, L.; Metanis, N.; Weidmann, S.; Zenobi, R. *J. Phys. Chem. C* **2012**, *116*, 23061-23066.

16.   Deckert-Gaudig, T.; Kämmer, E.; Deckert, V. *J. Biophotonics* **2012**, *5*, 215-219.

17.   Deckert-Gaudig, T.; Rauls, E.; Deckert, V. *J. Phys. Chem. C* **2010**, *114*, 7412-7420.

18.   Pashaee, F.; Tabatabaei, M.; Caetano, F. A.; Ferguson, S. S. G.; Lagugné-Labarthet, F. *Analyst* **2016**, *141*, 3251-3258.

19.   Paulite, M.; Blum, C.; Schmid, T.; Opilik, L.; Eyer, K.; Walker, G. C.; Zenobi, R. *ACS Nano* **2013**, *7*, 911-920.

20.   Sereda, V.; Lednev, I. K. *Appl. Spectrosc.* **2017**, *71*, 118-128.

21.   Deckert-Gaudig, T.; Deckert, V. *Small* **2009**, *5*, 432-436.

22.   Chu, H.-C.; Kuo, C.-H.; Huang, M. H. *Inorg. Chem.* **2006**, *45*, 808-813.

23.   Guo, Z.; Zhang, Y.; Mao, Y.; Huang, L.; Gu, N. *Mater. Lett.* **2006**, *60*, 3522-3525.

24.   Zhang, Q.; Hu, Y.; Guo, S.; Goebl, J.; Yin, Y. *Nano Lett.* **2010**, *10*, 5037-5042.

25.   Baffou, G.; Quidant, R. *Laser Photonics Rev.* **2013**, *7*, 171-187.

26.   Jauffred, L.; Samadi, A.; Klingberg, H.; Bendix, P. M.; Oddershede, L. B. *Chem. Rev.* **2019**, *119*, 8087-8130.

27. Huschka, R.; Zuloaga, J.; Knight, M. W.; Brown, L. V.; Nordlander, P.; Halas, N. J. *J. Am. Chem. Soc.* **2011**, *133*, 12247-12255.

28. Riley, R. S.; Dang, M. N.; Billingsley, M. M.; Abraham, B.; Gundlach, L.; Day, E. S. *Nano Lett.* **2018**, *18*, 3565-3570.

29. Baffou, G.; Polleux, J.; Rigneault, H.; Monneret, S. *J. Phys. Chem. C* **2014**, *118*, 4890-4898.

30. Dagallier, A.; Boulais, E.; Boutopoulos, C.; Lachaine, R.; Meunier, M. *Nanoscale* **2017**, *9*, 3023-3032.

31. Setoura, K.; Okada, Y.; Hashimoto, S. *Phys. Chem. Chem. Phys.* **2014**, *16*, 26938-26945.

32. Valev, V. K.; Denkova, D.; Zheng, X.; Kuznetsov, A. I.; Reinhardt, C.; Chichkov, B. N.; Tsutsumanova, G.; Osley, E. J.; Petkov, V.; De Clercq, B.; Silhanek, A. V.; Jeyaram, Y.; Volskiy, V.; Warburton, P. A.; Vandenbosch, G. A. E.; Russev, S.; Aktsipetrov, O. A.; Ameloot, M.; Moshchalkov, V. V.; Verbiest, T. *Adv. Mater.* **2012**, *24*, OP29-OP35.

33. Zeng, Z.-C.; Wang, H.; Johns, P.; Hartland, G. V.; Schultz, Z. D. *J. Phys. Chem. C* **2017**, *121*, 11623-11631.

34. Mochizuki, M.; Lkhamsuren, G.; Suthiwanich, K.; Mondarte, E. A.; Yano, T.-a.; Hara, M.; Hayashi, T. *Nanoscale* **2017**, *9*, 10715-10720.

35. Jain, P. K. *J. Phys. Chem. C* **2019**, *123*, 24347-24351.

36. Sarhan, R. M.; Koopman, W.; Schuetz, R.; Schmid, T.; Liebig, F.; Koetz, J.; Bargheer, M. *Sci. Rep.* **2019**, *9*, 3060.

37. Baumberg, J. J. *Faraday Discuss.* **2019**, *214*, 501-511.

38. Maestro, L. M.; Haro-González, P.; Coello, J. G.; Jaque, D. *Appl. Phys. Lett.* **2012**, *100*, 201110.

39. Freddi, S.; Sironi, L.; D'Antuono, R.; Morone, D.; Donà, A.; Cabrini, E.; D'Alfonso, L.; Collini, M.; Pallavicini, P.; Baldi, G.; Maggioni, D.; Chirico, G. *Nano Lett.* **2013**, *13*, 2004-2010.

40. Bendix, P. M.; Reihani, S. N. S.; Oddershede, L. B. *ACS Nano* **2010**, *4*, 2256-2262.

41. Cai, Y.-Y.; Sung, E.; Zhang, R.; Tauzin, L. J.; Liu, J. G.; Ostovar, B.; Zhang, Y.; Chang, W.-S.; Nordlander, P.; Link, S. *Nano Lett.* **2019**, *19*, 1067-1073.

42. Brongersma, M. L.; Halas, N. J.; Nordlander, P. *Nat. Nanotechnol.* **2015**, *10*, 25-34.

43. Baffou, G.; Quidant, R.; García de Abajo, F. J. *ACS Nano* **2010**, *4*, 709-716.

44. Keblinski, P.; Cahill, D. G.; Bodapati, A.; Sullivan, C. R.; Taton, T. A. *J. Appl. Phys.* **2006**, *100*, 054305.

45. Rodríguez-Oliveros, R.; Sánchez-Gil, J. A. *Opt. Express* **2012**, *20*, 621-626.

46.   Downes, A.; Salter, D.; Elfick, A. *Opt. Express* **2006**, *14*, 5216-5222.

47.   Petrova, H.; Perez Juste, J.; Pastoriza-Santos, I.; Hartland, G. V.; Liz-Marzán, L. M.; Mulvaney, P. *Phys. Chem. Chem. Phys.* **2006**, *8*, 814-821.

48.   Oras, S.; Vlassov, S.; Vigonski, S.; Polyakov, B.; Antsov, M.; Zadin, V.; Lõhmus, R.; Mougin, K. *Beilstein J. Nanotechnol.* **2020**, *11*, 61-67.

49.   Lax, M.; Louisell, W. H.; McKnight, W. B. *Phys. Rev. A* **1975**, *11*, 1365-1370.

50.   Balois, M. V.; Hayazawa, N.; Catalan, F. C.; Kawata, S.; Yano, T.-a.; Hayashi, T. *Anal. Bioanal. Chem.* **2015**, *407*, 8205-8213.

51.   Kazemi-Zanjani, N.; Vedraine, S.; Lagugné-Labarthet, F. *Opt. Express* **2013**, *21*, 25271-25276.

52.   Zhang, W.; Schmid, T.; Yeo, B.-S.; Zenobi, R. *J. Phys. Chem. C* **2008**, *112*, 2104-2108.

53.   Chen, X.; Wen, R.; Zhang, L.; Lahiri, A.; Wang, P.; Fang, Y. *Plasmonics* **2014**, *9*, 945-949.

54.   Lee, S. J.; Piorek, B. D.; Meinhart, C. D.; Moskovits, M. *Nano Lett.* **2010**, *10*, 1329-1334.

55.   Munro, C. H.; Smith, W. E.; Garner, M.; Clarkson, J.; White, P. C. *Langmuir* **1995**, *11*, 3712-3720.

56.   Siiman, O.; Bumm, L. A.; Callaghan, R.; Blatchford, C. G.; Kerker, M. *J. Phys. Chem.* **1983**, *87*, 1014-1023.

57.   Tada, H.; Bronkema, J.; Bell, A. T. *Catal. Lett.* **2004**, *92*, 93-99.

58.   Takeyasu, N.; Yamaguchi, K.; Kagawa, R.; Kaneta, T.; Benz, F.; Fujii, M.; Baumberg, J. J. *J. Phys. Chem. C* **2017**, *121*, 18795-18799.

Chapter 6

6   Exploiting Fractal Patterns for the Rational Development of Metallic Nanostructure Geometries

As applications of plasmonics are invariably linked to their optical properties, as determined by the geometry and composition of the nanostructure, as well as the irradiation conditions, it is important to develop and characterize new structures for future applications. This is particularly true for applications in plasmon-mediated reactions, where hot carriers are steered by the geometry of the nanostructure.[1,2] In this chapter, the development of fractal nanostructures and the simulated and experimental behaviour of their plasmon modes, investigated using a variety of techniques and calculations, is discussed. Finally, the structures are functionalized and their applicability for surface-enhanced measurements is demonstrated.

6.1   Introduction

Metallic nanostructures with simple geometries, such as small gold nanospheres, are generally limited to two resonances in the visible regime: the dipolar and quadripolar mode (Figure 6-1a).[3] This limits their applicability to plasmon-mediated reactions and other applications. In order to develop a broadband plasmonic response, fractal nanostructures have been examined.[4-6] A fractal structure results in multiple plasmonic resonances, which can be predicted by modelling and measured experimentally, using techniques such as mid-infrared nanoscopy (nano-FTIR) and electron energy loss spectroscopy (EELS). By tuning the polarization and wavelength of the incident beam, the hotspots associated with confinement of electromagnetic field can be selectively excited, enabling full optical control over the plasmons associated with a given structure. The numerous plasmonic resonances occurring in fractal structures can be explained using a hybridization model, wherein the modes of a structure and a cavity can constructively or destructively interfere to create new modes (Figure 6-1b).[7,8] In the case of a nanoshell, the plasmons induce surface charges at the inner and outer interfaces of the metal shell; due to the finite thickness of the shell, these plasmons interact, splitting into two new plasmon resonances.
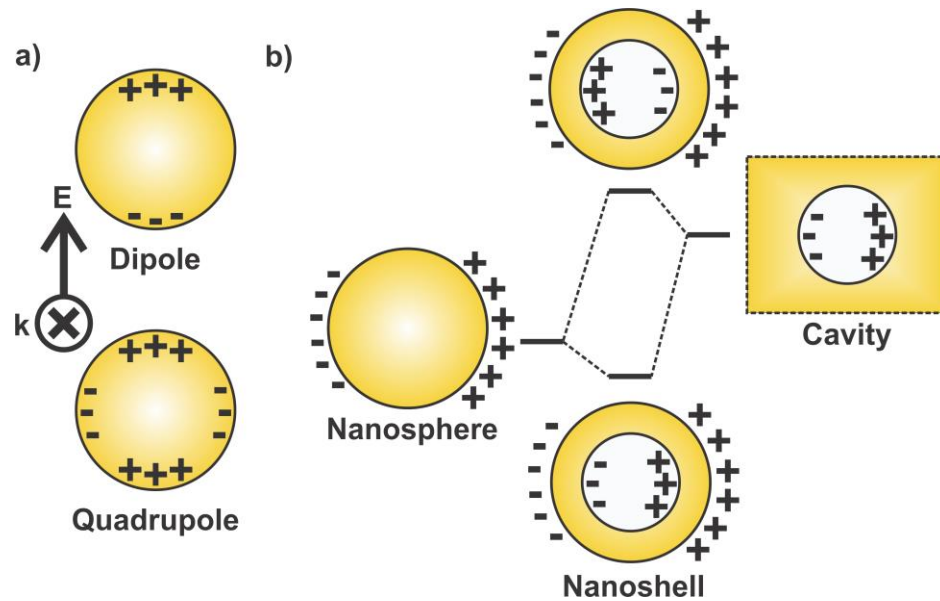
Figure 6-1 a) Dipole and quadrupole modes of a gold nanosphere; b) Hybridization model of plasmonic resonances, where the energies of the plasmon modes of a gold nanoshell are described as a combination of those of a nanosphere and a cavity.

The fractals on which the nanostructures in this thesis are based are the Bethe lattice and the Sierpiński triangle. The Bethe lattice is a branching structure, identified by the number of branches b. In each subsequent generation of the fractal, each branch leads to $b - 1$ new branches, as shown in Figure 6-2a.[9] Bethe lattice fractals are labelled by the number of branches and the generation i.e. 3BG2 indicates a three-branched structure with two generations (Figure 6-2a). The Sierpiński triangle involves removing a section of an equilateral triangle, as defined by the midpoints of the sides of the triangle, as in Figure 6-2b.[10] This process is repeated iteratively, each new generation n comprising 3^n triangles.
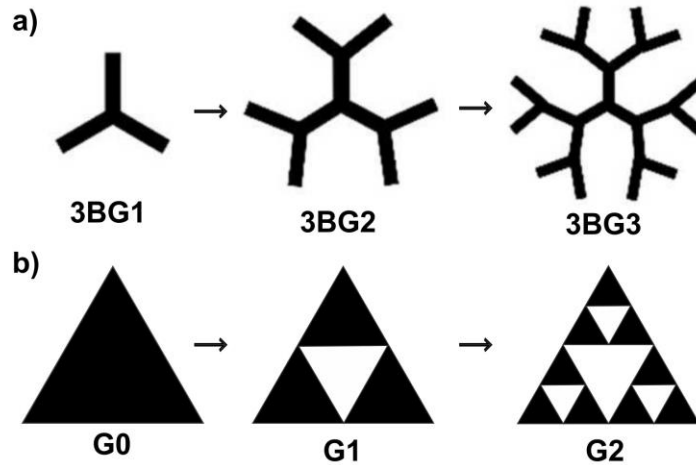
Figure 6-2 a) Three-branched Bethe lattice, from first generation (3BG1) to the third (3BG3); b) Sierpiński triangle, from the base unit (equilateral triangle, G0) to the second generation (G2)

Mathematically, fractals are infinite; experimentally, these fractals are truncated after several generations, so that they can be reproduced through nanofabrication techniques which have an intrinsic spatial resolution of about 10 nm. Additionally, the terms Bethe lattice and Sierpiński triangle both refer to two-dimensional fractals; typically, they are fabricated with metal thicknesses in the range of tens of nanometres.

In this chapter, we will:

i) use nano-FTIR to investigate the plasmonic modes of a Bethe Lattice fractal nanostructure, and compare to those predicted by finite-difference time-domain (FDTD) simulations;

ii) study the evolution of the plasmon modes of a silver Sierpiński nanostructure by EELS and FDTD;

iii) apply the gold Sierpiński nanostructure to surface-enhanced Raman mapping, and compare to the electric field simulated by FDTD.

6.2   Bethe Lattice

Five-branched Bethe lattice of the second generation (5BG2) and three-branched, fifth-generation (3BG5) metastructures were fabricated in arrays of 50×50 μm^2 (10×10 to 30×30 individual fractal structures, separated by 0.8 μm) by electron-beam lithography (Chapter 3.6.3). SEM images of individual structures are shown in Figure 6-3a,b. Microabsorption measurements were conducted, using a mid-IR synchrotron source combined with a far-field microscope. As shown in Figure 6-3c, the 5BG2 fractal exhibits two dominant resonances in the near- to mid-IR range (6000–1000 cm^{-1}), while the 3BG5 fractal exhibits a series of 4-5 resonances spanning the same spectral domain (Figure 6-3d). These resonances, dependent upon the number of fractal generations, are associated with both dipolar and multipolar modes. The first-order generation exhibits a single resonance, with each subsequent generation introducing a new plasmon resonance. Applying the hybridization model (as shown in Figure 6-1b), it appears that the modes with the higher energies are associated with the outermost generation, while the modes with the lower energies appear as coupling of modes from the outer structure towards the inner, first-generation structure.[5] This holds true for the lowest energy resonances of the 3BG5 fractal.
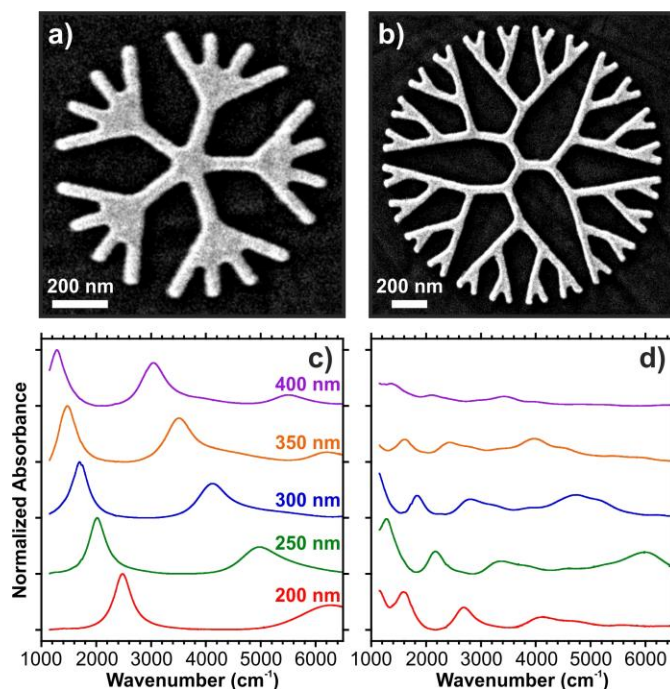
Figure 6-3 SEM images of a) 5BG2 with rod length 300 nm and b) 3BG5 with rod length 200 nm. Near- to mid-IR absorption spectra of the c) 5BG2 and d) 3BG5 fractal, with rod lengths varying from 200 to 400 nm.

Figures 6-3c and 6-3d further demonstrate that by changing the length of the rods, the "G0" building block, the spectral positions and the number of resonances can be tailored. The ability to tune the plasmonic properties is a critical factor for potential applications. Further study of these resonances is achieved through the combination of FDTD calculations and experimental nano-FTIR measurements.

6.2.1 Electromagnetic Field Modelling and Nano-FTIR Measurements

In order to correlate these resonances observed in the IR absorption spectra with the spatial distribution of the enhanced electromagnetic field, mid-infrared nanoscopy (nano-FTIR) measurements were made on the 5BG2 fractal. As previously discussed (Chapter 3.2.1), this involves using a sharp metal tip, and tracking the backscattered IR light to yield the IR spectrum of the sample in the near-field. This is usually modelled through simulations; however, such simulations can be of limited accuracy, largely due to differences between the simulated and experimental geometries caused by rounding of

edges experimentally, surface roughness introduced during the metal deposition, and potential defects. Additionally, as in investigating arrays of relatively large structures (micron scale) with small features (nanometer scale), these simulations can be costly in time or computational resources.

Firstly, an AFM image of the 5BG2 nanostructure array was acquired (Figure 6-4a). This array is with the rod length of 300 nm, making the entire fractal structure about 1.2 µm wide, which are then arranged in an array of 27×27 nanostructures. Subsequently, the near-field distribution of $|E_p|$ was collected (Figure 6-4b), polarized along one of the branches of the fractal, as indicated by the black arrow in the figure. This was acquired at a wavelength of 5.88 µm, corresponding to the resonance at 1700 cm^{-1}, as shown in the IR absorption spectrum (Figure 6-3c; blue line). The strongest response in the near-field distribution of $|E_p|$ is observed along the branch parallel to the direction of polarization. Following this, the near-field phase φ_p and Re(E_p) are measured (Figure 6-4c,d), with the relation Re(E_p) = $|E_p|\cos(\varphi_p)$. This phase map shows a 180° phase change perpendicular to the direction of polarization; this is characteristic of a dipolar resonance.[11-13] In all of these maps, the homogeneity of the signal from structure to structure is clear, indicating that the array gives a uniform response. In order to compare the efficacy of these experimental techniques to the standard simulation methods, finite-difference time-domain (FDTD) simulations were performed on the fractal nanostructure. In the simulation, this resonance occurs at 6.2 µm, redshifted from the experimental measurement by about 320 nm; this is due to the limitations of simulated as discussed above. The calculated Re(E_z) near-field distribution, as shown in Figure 6-4e, matches the experimental Re(E_p) well; this implies that the electric field components as detected experimentally are largely polarized in the z-direction. The calculated electric field amplitude $|E|$ (Figure 6-4f) is similar to the experimental distribution, with the branches along the direction of polarization showing the strongest response.
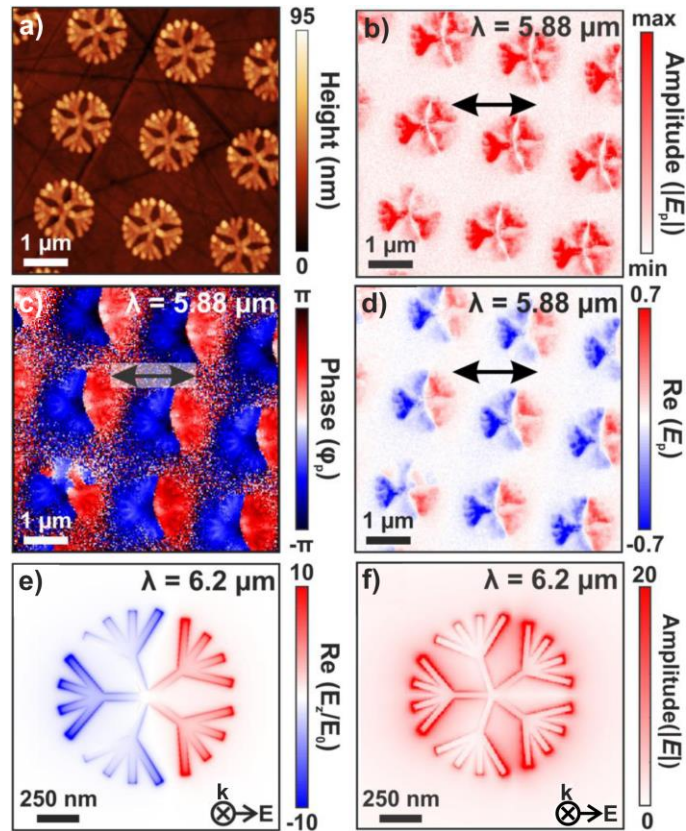
Figure 6-4 a) AFM image of 5BG2 fractal, with rod length 300 nm, with corresponding experimental b) amplitude, c) phase and d) Re(E_p) maps. Calculated results of e) Re(E_z/E_0) and f) near-field amplitude $|E|$ for the same structure.

Despite the limitations of simulations as previously discussed, the broadband nature of FDTD simulations allows for insights that are not easily achieved using nano-FTIR. In Figure 6-5a and 6-5b, the 5BG2 and 3BG5 structures are shown, corresponding to the isowavelength maps in Figure 6-5c and d. These maps are constructed from simulating the electromagnetic field at the surface of the nanostructure at 54 wavelengths, spaced out between 1.4 and 12 µm. The component of the electric field along the direction of polarization, E_x, is mapped, forming a 4-D tensor: the value of E_x as a function of position (x, y) and wavelength. For each point (x, y) of the map, the maximum value of E_x is found, and the wavelength for which this maximum occurred is recorded in the isowavelength map. Therefore, the constructed map simply shows the enhanced electric field as a function of wavelength. In the isowavelength map of the 5BG2 structure, only one main resonance is shown: the 6.2 µm dipolar resonance mapped previously. The

map of the 3BG5 resonances shows more resonances, with those of higher energy including less of the structure, tending toward the outer branches. There is some overlap of enhancement regions, as these outermost branches contribute consistently to more than one resonance; in sensing, this could mean adsorbed molecules could be probed at more than one wavelength.
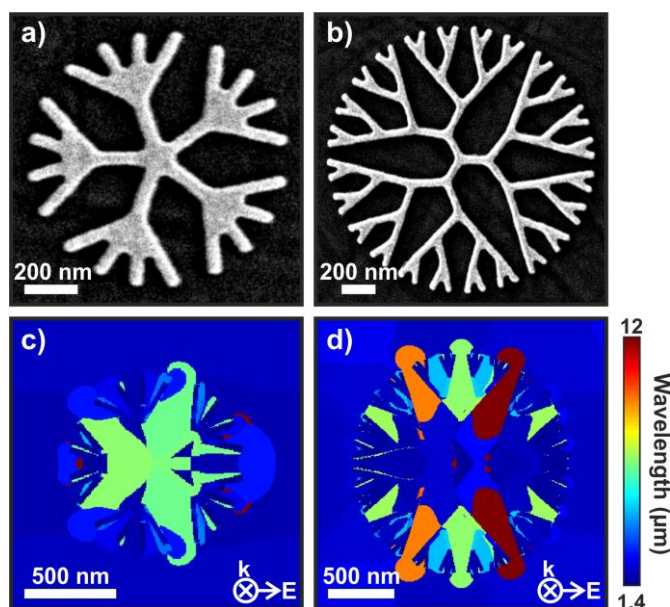
Figure 6-5 SEM images of the a) 3BG5 and b) 5BG2 structures, corresponding to the isowavelength maps c) and d).

The Bethe lattice and the application of nano-FTIR and FDTD to study the resonances in the IR region has been discussed. In the following sections, the response of the Sierpiński triangle-based nanostructures in the visible region is studied both by FDTD and electron-energy loss spectroscopy (EELS), and applied to SERS.

6.3 Sierpiński Nanostructures

Sierpiński nanostructures were fabricated by electron-beam lithography, using both silver and gold. Firstly, a series of triangles were fabricated in silver, for study by electron energy loss spectroscopy (EELS). In order to study the effect of introducing an aperture to the solid G0 silver nanostructure in moving from G0 to G1, a series of nanoprisms with increasingly large apertures was created (Figure 6-6a). Additionally, nanostructures

with a side length of 125 nm were fabricated, with 3 nm of titanium followed by 20 nm of gold. In order to study the effect of the fractal pattern, the fractal nanostructure was made from G1 to G8, comprising up to $3^8 = 6561$ individual nanoprisms; G3, G4, G6 and G8 are shown in Figure 6-6b-d.
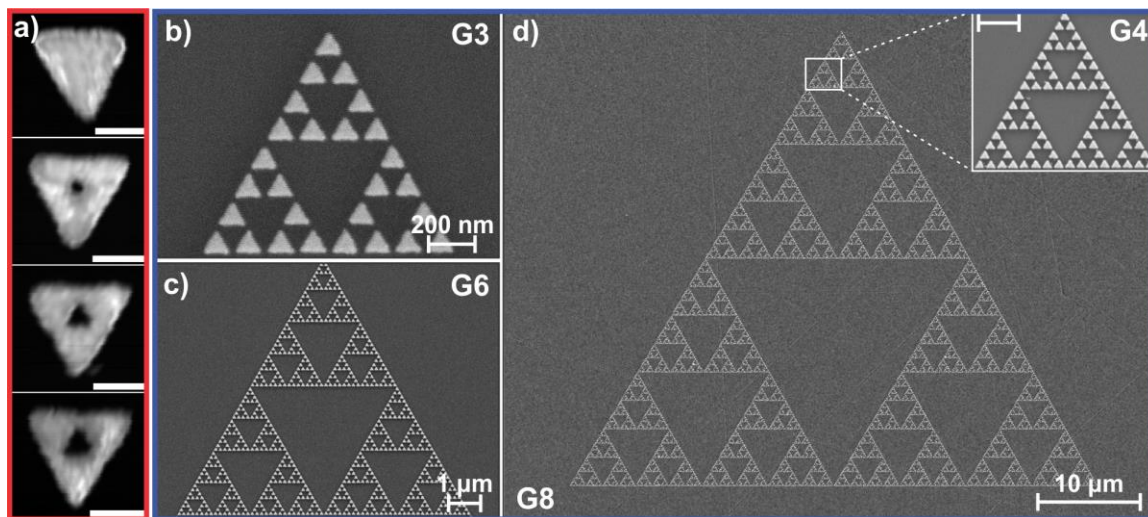
Figure 6-6 a) HAADF-STEM images of Sierpiński structures in silver, showing the transition from G0 to G1, with a scale bar of 150 nm. SEM images of the gold Sierpiński nanostructures at a) G3, b) G6 and c) G9, with G4 inset (scale bar of 500 nm).

In this chapter, the smaller silver nanostructures are studied by FDTD, and the evolution of the plasmon modes in creating the fractal pattern is investigated by STEM-EELS. In this instance, a subtractive, or convergent, fractal is studied, as the higher-order generations of the fractal are obtained through the removal of material at the centre of the building block G0 structure. Silver was chosen for so that higher order modes were in the visible range, such that they can be probed by EELS. The larger gold nanostructures are studied using FDTD calculations, and applied to SERS measurements of 4-nitrothiophenol (4-NTP). These fractals are considered additive, or divergent, fractals, such that the individual building block, the G0 triangle, is maintained at the same size, and the triangles are added to obtain higher generation fractals.

6.3.1 Modelling and Electron Energy Loss Spectroscopy of Silver Sierpiński Nanostructures

Through finite-difference time-domain (FDTD) calculations, it is possible to simulate the electromagnetic field of nanostructure as a function of wavelength, allowing for the further calculation of the surface charges and scattering or absorption cross-sections. From the electric field surrounding the nanostructure, the divergence of the electric field can be calculated. Assuming there are no bound charges, this allows for the calculation of the surface charge on the nanostructure through the application of Gauss' Law. This was applied to the study of the silver, subtractive fractal. The aim was to determine how fractalization affected the plasmon modes of the Sierpiński fractal. To achieve this, a series of G0 and G1 fractals of side length 285 nm were simulated. The series of fractals have an increasing aperture size, from G0, with no aperture, to a G1 fractal that is three individual nanoprisms, the latter matching the shape of the gold fractal discussed in Chapter 6.3.2.

The surface charges of the G0 inverse structure, a triangular aperture of 285 nm in a thin metal surface, followed by the G0 to G1 series, are shown in Figure 6-7. The two lowest energy optical modes are mapped. As observed from the energies of the modes, these are orthogonal, degenerate modes, until the fractal is separated into three nanoprisms and the degeneracy is broken, forming new hybridized modes (Figure 6-7e). The modes are redshifted as the size of the aperture is increased. Additionally, it can be noted that the respective energies of the modes are the same for the positive and inverse G0 structure (Figure 6-7a and b). This follows from the Babinet principle, which states that incident light will excite an aperture antenna when the light polarization is orthogonal to that used to excite the complementary positive structure.[14,15] This complementary behaviour is observed in comparing the charge maps: in the inverse structure, charges can flow around corners, but are confined by the edges, and build-up of charge along the edges creates dipolar fields across the aperture. Conversely, the positive structure confines charges at the vertices.
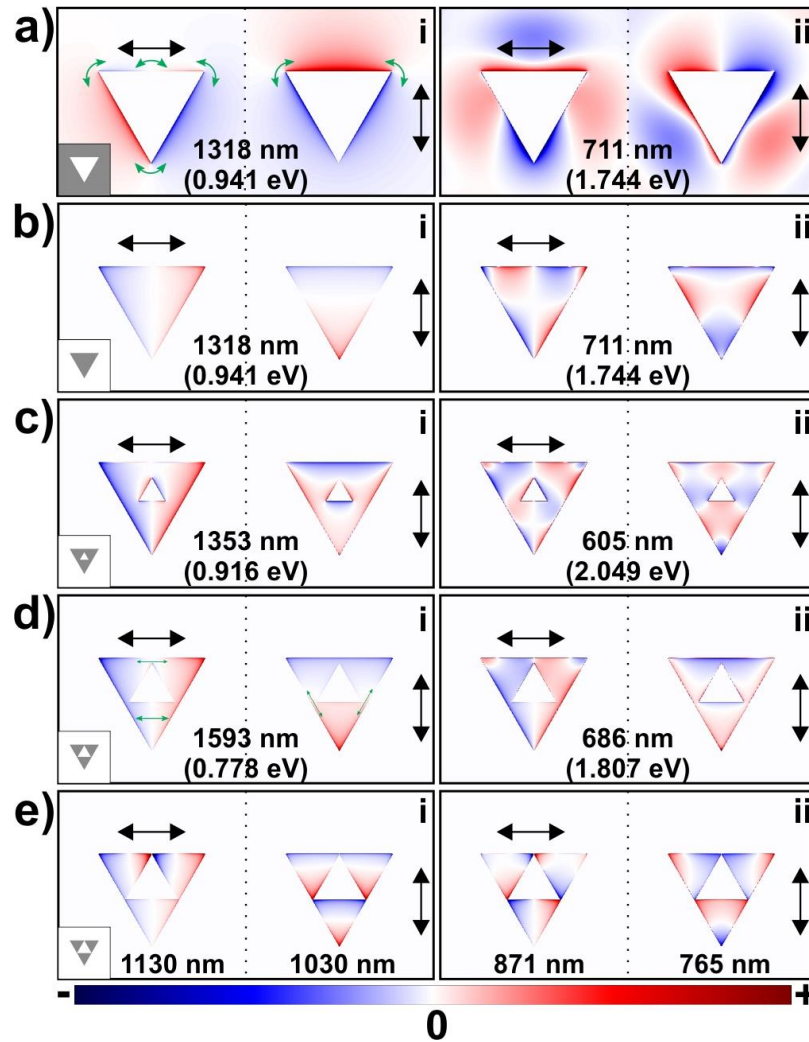
Figure 6-7 Calculated surface charge distributions for the first mode i) and second mode ii) of a) a 285 nm inverse G0 aperture in a silver film; b) a silver G0 triangle of the same size; c) a 285 nm G1 structure with a 73 nm hole; d) a 285 nm G1 structure with a hole 10 nm from the edge of the triangle; e) a 285 nm G1 structure with no coupling between individual triangles. Wavelengths in e) correspond to 1130 nm = 1.097 eV; 1030 nm = 1.204 eV; 871 nm = 1.423 eV; and 765 nm = 1.621 eV. Polarization, wavelength and corresponding energies are as indicated; a diagram of the structure is shown in the inset.

By monitoring the incident and scattered electric fields around the nanostructure, the absorption or scattering cross-sections can be calculated. In the study of the silver, subtractive fractals, the scattering cross-section was calculated for the G0 to G1 series

(Figure 6-8a) as well as the inverse structures, triangular apertures of 73 nm, 142.5 nm and 285 nm, corresponding to the aperture size corresponding to the spectrum in orange in Figure 6-8a (and mapped in Figure 6-8c); the aperture size corresponding to the spectrum in purple in Figure 6-9a (and mapped in Figure 6-8e); and the inverse, 285 nm aperture, mapped in Figure 6-7a, respectively. As expected from the energies of the calculated surface charge maps, there is a redshift in the resonance as the size of the aperture is increased, until the fractal is no longer one solid structure and the degeneracy is broken (Figure 6-8a; purple spectrum). This trend is also observed in the spectrum of the apertures alone: as the size of the aperture is increased from 73 nm to 285 nm, the resonance peak redshifts.
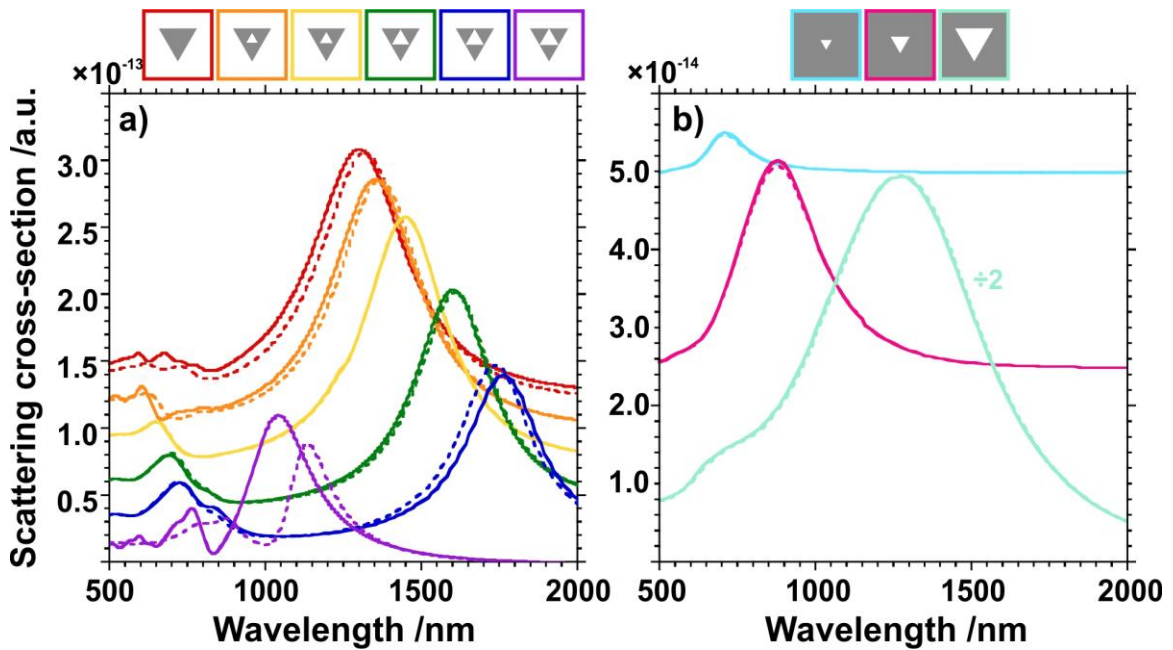
Figure 6-8 Calculated scattering cross-section of a) a solid G0 285 nm silver structure (red); the same structure with a 73 nm aperture (orange); with a 122.5 nm aperture (yellow); with 10 nm (green); with 6 nm (blue); with no coupling between individual triangles (purple); and b) the inverse structure, an aperture of 73 nm in a silver film (light blue); 142.5 nm (magenta); and 285 nm (mint, cross-section divided by 2). Polarization is vertical (solid line) or horizontal (dashed line); spectra are offset for clarity.

After simulation of the optical modes of the fractals, the modes were probed experimentally by electron energy loss spectroscopy (EELS). Differences between the modes as observed by EELS and the optical simulations are due to several factors, including that EELS can observe dark modes, and EELS is polarization insensitive. Dark modes are non-radiative, having zero net dipole moment and are thus not excited optically.[16,17]

All EELS experiments were conducted at the Canadian Centre for Electron Microscopy at McMaster University, within a collaboration with Prof. Gianluigi Botton and his student, Isobel Bicket, and post-doctoral researcher, Dr. Edson Bellido.

Structures were fabricated as silver nanostructures, with a side length 285 nm, within an accuracy of 10 nm. All structures were fabricated simultaneously, to achieve uniformity. In Figure 6-9, the high-angle annular dark-field scanning transmission electron microscopy (HAADF-STEM) images are shown for the G0 to G1 series with increasing aperture size. Maps of the plasmon resonances are extracted at the energies as indicated, with energy windows chosen to minimize overlap between the maps. The resulting maps are classified as edge modes, where the EELS probability distribution is confined to the edges, and cavity modes, where the distribution lies in the structure. These cavity modes are dark modes, as they are not excited optically and thus are not observed in the simulated results above.
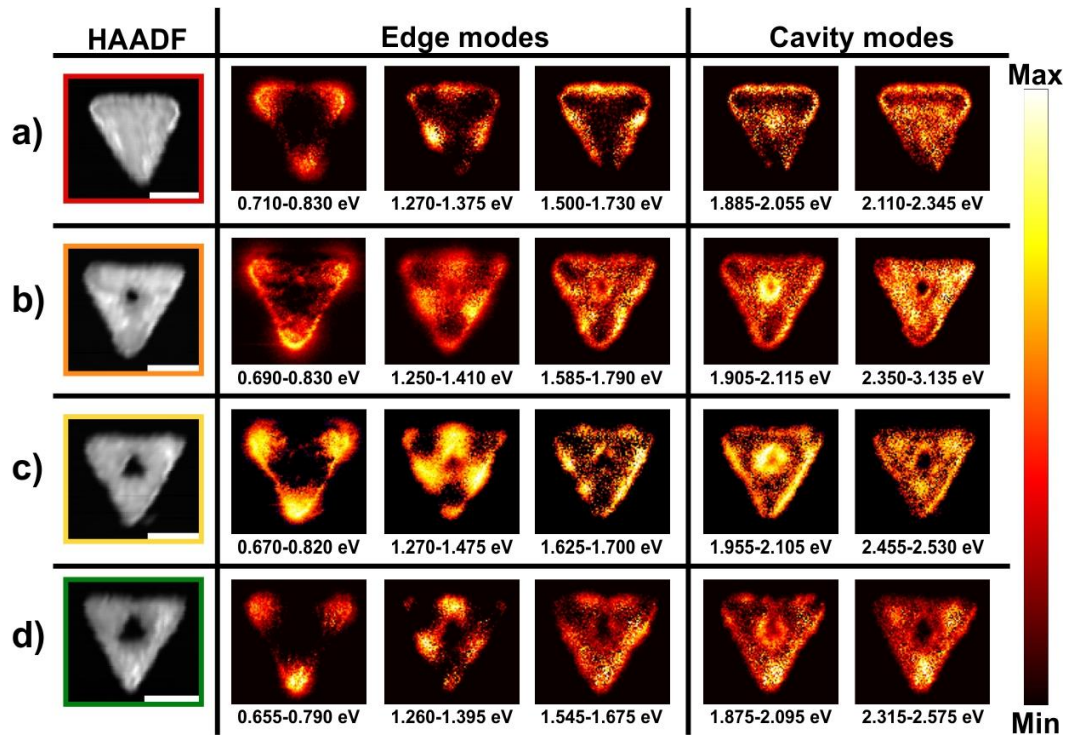
Figure 6-9 HAADF-STEM images and corresponding EELS intensity distributions of edge and cavity modes at energies as indicated, for a) G0 triangle; b) G1 fractal with small circular aperture; c) G1 fractal with larger triangular aperture; d) G1 fractal with slightly larger triangular aperture. Scale bar in HAADF-STEM images is 150 nm.

As was shown in the simulated results, the dipole mode (lowest energy edge mode) redshifts after the introduction of the aperture, to 0.78 eV, and is further grown, to 0.74 and 0.73 eV. The EELS probability distribution, proportional to the normal component of the electric field of this mode, does not change greatly as the size of the aperture is increased; this implies that the electric field distribution does not greatly modify the distribution of the electric field. This is supported by the calculated surface charges (Figure 6-7c,d), where there is only a small build-up of charge around the aperture.

This redshift can be described by the coupling of the solid G0 structure and the modes of the aperture. Although these modes are of very different energies (Figure 6-8a *vs.* b), their electric field distributions are similar, as described by the Babinet principle. This allows the modes to couple, shifting the energy of the dipole modes. As the G0

nanoprism and the aperture are of the same symmetry, both degenerate dipole modes shift equally when the aperture is introduced. As the aperture size increases, this mode is redshifted, resulting in more spectral overlap with the mode of the G0 parents and a stronger redshift. When the structure is broken into three nanoprisms, the aperture no longer supports a resonance, breaking this coupling and resulting in the loss of degeneracy of the modes.

The second-order edge mode is a dark mode, not observed in the FDTD simulations. It varies only a little in energy, with no strong trend, but the EELS distribution is affected by the growth of the aperture, with the antinode shifting from the centre of the edge toward the central aperture. Unlike the first-order mode, it does not couple to the aperture mode, potentially because the Babinet principle does not necessarily apply to dark modes.

The third-order edge mode consists of three nodes and four antinodes along each edge of the triangle, and is the second optical mode observed in the FDTD simulations. Upon introduction of the aperture, there is a blueshift of 100 meV in the energy of this mode, but further increase in the size of the aperture does not greatly affect the energy. The polarization-sensitivity of the optical simulations is useful here, in revealing that this mode consists of two degenerate modes with orthogonal polarizations.

Two dark cavity modes are observed in the EELS maps. The lowest energy mode is only slightly shifted (20 meV) by the introduction of the aperture, implying that the energy of the mode is not greatly affected by the introduction of the aperture. Similar in behaviour to the dark, second-order edge mode, the EELS distribution changes, moving towards the inner aperture in accommodating its introduction. The second-order cavity mode blueshifts with the introduction of the aperture, and further blueshifts as the aperture is grown. In the EELS probability distribution, a high EELS signal is seen in the centre of the smaller G0 fractal units.

6.3.2 Modelling and Surface-Enhanced Raman Spectroscopy of Gold Sierpiński Nanostructures

Determination of the spatial location of these hotspots is critical for applications in plasmon-mediated chemistry, where reactions are catalyzed in the hotspots.[1,2] The gold, additive G1 fractal was modelled by three 125 nm nanoprisms of 20 nm of Au on top of 3 nm of Ti on a glass substrate. When irradiated with vertically polarized plane wave, the electric field distribution at 800 nm shows the highest intensity at the top apices of the individual nanoprisms forming the G1 fractal structure (Figure 6-10a). For the orthogonal polarization, the electric field at 800 nm is confined to the bottom apices of the nanoprisms, as shown in Figure 6-10b. The fractal metastructure is self-similar, such that this result for the electric field can be extrapolated for higher-order generations. As individual nanoprisms are added, in moving from G1 to G8, the polarization-dependent hotspots are located in the gaps between the nanoprisms.
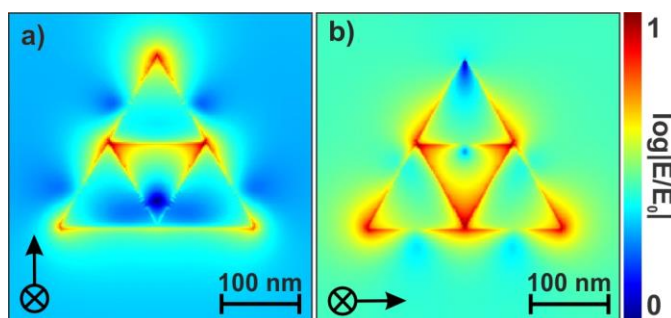
Figure 6-10 Calculated normalized distributions of the electric field at 800 nm, polarized a) vertically and b) horizontally.

From the calculated map of the electric field of the gold G1 fractal structure (Figure 6-10), it was determined that the higher-order metastructures could be used for applications in surface-enhanced Raman spectroscopy (SERS) due to the multiple resonances in the visible range. To investigate this, the nanostructures were incubated in a 10 mM solution of 4-nitrothiophenol (4-NTP) in order to obtain a monolayer. Both 632.8 nm and 785 nm laser excitations were used for the SERS study, as shown in the spectra in Figure 6-11a. Microspectroscopy measurements allowed for the determination of the distribution of the 4-NTP over the surface of the metastructure: at each point of the map of the

metastructure, a SERS spectrum is acquired. Through the integration of a particular mode, in this instance the symmetric NO_2 stretching mode of 4-NTP ([1300-1375] cm^{-1} range), the distribution of the 4-NTP over the metastructure is determined. Uniform functionalization of the gold fractal nanostructures is achieved, as shown in Figure 6-11b, exhibited by the minimal variation of the signal intensity. Regions off the gold metastructures appear darker in the map, with little to no 4-NTP adsorbed on the substrate and no enhancement of the Raman signal in these areas. Under 632.8 nm excitation, SERS maps were acquired on G6, G7 and G8 metastructures; under 783 nm excitation, the G7 metastructure was investigated (Figure 6-11b, i-iv). SERS measurements are diffraction-limited, so in these measurements it is not possible to spatially resolve metastructures smaller than G5 (Figure 6-11b, i & iv), and individual hotspots as predicted by the calculation in Figure 6-10, are not distinguishable. Under these conditions the G5 structure (~ 4000 nm across) is sufficiently larger than the beam diameter. With a longer excitation wavelength, a poorer spatial resolution is obtained, as is expected for diffraction-limited measurements, resulting in more difficulty in distinguishing G5 in the map at 785 nm (Figure 6-11b iv), than the maps at 632.8 nm (Figure 6-11b i-iii).

A further map of G6 was collected with the laser power increased tenfold, from 0.88 mW to 8.8 mW, in order to further investigate the optical properties of the functionalized metastructure. This map was then analyzed by principle component analysis (PCA), transforming the data set constituting the map into uncorrelated principle components. Analysis of the one of the principle components (Figure 6-11c) shows that it matches the SERS spectrum of 4,4'-dimercaptoazobenzene (DMAB), the dimer of 4-NTP, which shows characteristic peaks at 1134 cm^{-1} (C-H bend + C-N stretch), and 1387 and 1434 cm^{-1} (N=N stretch + C-C stretch + C-H bend).[18] The dimerization of p-NTP to DMAB, as triggered in the hotspots of metal nanostructures, is a well-studied plasmon-mediated reaction.[18,19] Figure 6-11d shows the distribution of this component over the surface of the metastructure, showing in red the areas of highest prevalence of this component, and thus the areas of highest electric field enhancement. The non-uniformity of these hotspots could be due to defects in the structure; although electron-beam lithography can reproducibly fabricate the structures (as shown in Figure 6-6b-d), sub-nanoscale

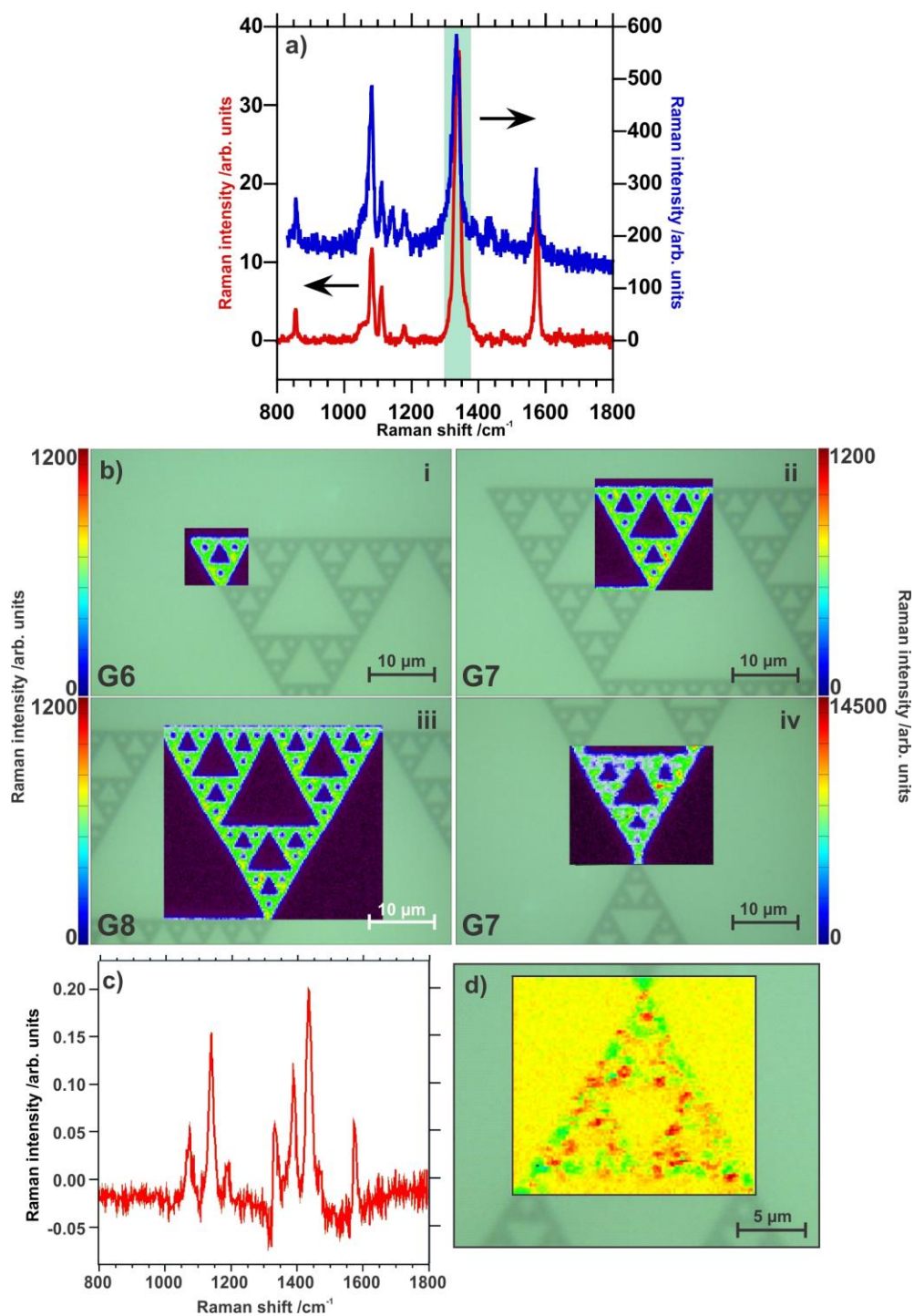variations and ultrathin gaps at the metal surface further increase the confinement of the electromagnetic field.[20-22]

Figure 6-11 a) SERS spectra collected on the gold Sierpiński structures at λ = 632.8 nm (red) and λ = 785 nm (blue), with the ν_s NO$_2$ mode highlighted; b) SERS maps

obtained from the integration of the mode highlighted in a) on i) G6, ii) G7, iii) G8 at λ = 632.8 nm; and iv) G7 at λ = 785 nm. c) Principle component with peaks of DMAB and d) map of the distribution of this component over the metastructure surface.

6.4 Conclusions

Overall, the plasmon modes of Bethe lattice and Sierpiński fractal nanostructures have been methodically evaluated using both experimental measurements and numerical calculations. By performing s-SNOM measurements on the Bethe Lattice fractals, the experimental distributions for the near-field enhancement can be obtained at the level of a single structure and compared with numerical results. For silver Sierpiński fractal nanostructures, the behaviour of the plasmon modes was investigated using FDTD simulations and EELS measurements. For this subtractive fractal, it was found that increasing the generation number redshifted the primary dipolar energy, with no change in the physical footprint of the nanostructure. Increasing the generation number of the fractal may be an efficient way to redshift the dipolar modes of the nanostructure, but is limited practically by the resolution of nanofabrication techniques. Gold Sierpiński fractal metastructures, fabricated from the first to the eighth generation, were studied through FDTD calculations, and their applicability to SERS measurements was demonstrated.

6.5 References

1.   Nguyen, V.-Q.; Ai, Y.; Martin, P.; Lacroix, J.-C. *ACS Omega* **2017**, *2*, 1947-1955.

2.   Nguyen, M.; Kherbouche, I.; Gam-Derouich, S.; Ragheb, I.; Lau-Truong, S.; Lamouri, A.; Lévi, G.; Aubard, J.; Decorse, P.; Félidj, N.; Mangeney, C. *Chem. Commun.* **2017**, *53*, 11364-11367.

3.   Amendola, V.; Pilot, R.; Frasconi, M.; Maragò, O. M.; Iatì, M. A. *J. Phys.: Condens. Matter* **2017**, *29*, 203002.

4.   Gottheim, S.; Zhang, H.; Govorov, A. O.; Halas, N. J. *ACS Nano* **2015**, *9*, 3284-3292.

5.   Wallace, G. Q.; Foy, H. C.; Rosendahl, S. M.; Lagugné-Labarthet, F. *J. Phys. Chem. C* **2017**, *121*, 9497-9507.

6.   Wallace, G. Q.; Lagugné-Labarthet, F. *Analyst* **2019**, *144*, 13-30.

7. Nordlander, P.; Oubre, C.; Prodan, E.; Li, K.; Stockman, M. I. *Nano Lett.* **2004**, *4*, 899-903.

8. Prodan, E.; Radloff, C.; Halas, N. J.; Nordlander, P. *Science* **2003**, *302*, 419-422.

9. Bethe, H. A.; Bragg, W. L. *Proc. R. Soc. London, Ser. A* **1935**, *150*, 552-575.

10. Kempkes, S. N.; Slot, M. R.; Freeney, S. E.; Zevenhuizen, S. J. M.; Vanmaekelbergh, D.; Swart, I.; Smith, C. M. *Nat. Phys.* **2019**, *15*, 127-131.

11. Grefe, S. E.; Leiva, D.; Mastel, S.; Dhuey, S. D.; Cabrini, S.; Schuck, P. J.; Abate, Y. *Phys. Chem. Chem. Phys.* **2013**, *15*, 18944-18950.

12. Neuman, T.; Alonso-González, P.; Garcia-Etxarri, A.; Schnell, M.; Hillenbrand, R.; Aizpurua, J. *Laser Photonics Rev.* **2015**, *9*, 637-649.

13. Schnell, M.; Garcia-Etxarri, A.; Huber, A. J.; Crozier, K. B.; Borisov, A.; Aizpurua, J.; Hillenbrand, R. *J. Phys. Chem. C* **2010**, *114*, 7341-7345.

14. Booker, H. G. *J. Inst. Electr. Eng. Part IIIA* **1946**, *93*, 620-626.

15. Horák, M.; Křápek, V.; Hrtoň, M.; Konečná, A.; Ligmajer, F.; Stöger-Pollach, M.; Šamořil, T.; Paták, A.; Édes, Z.; Metelka, O.; Babocký, J.; Šikola, T. *Sci. Rep.* **2019**, *9*, 4004.

16. Gómez, D. E.; Teo, Z. Q.; Altissimo, M.; Davis, T. J.; Earl, S.; Roberts, A. *Nano Lett.* **2013**, *13*, 3722-3728.

17. Deng, T.-S.; Parker, J.; Yifat, Y.; Shepherd, N.; Scherer, N. F. *J. Phys. Chem. C* **2018**, *122*, 27662-27672.

18. Sarhan, R. M.; Koopman, W.; Schuetz, R.; Schmid, T.; Liebig, F.; Koetz, J.; Bargheer, M. *Sci. Rep.* **2019**, *9*, 3060.

19. Gan, X. Y.; Keller, E. L.; Warkentin, C. L.; Crawford, S. E.; Frontiera, R. R.; Millstone, J. E. *Nano Lett.* **2019**, *19*, 2384-2388.

20. Baumberg, J. J.; Aizpurua, J.; Mikkelsen, M. H.; Smith, D. R. *Nat. Mater.* **2019**, *18*, 668-678.

21. Urbieta, M.; Barbry, M.; Zhang, Y.; Koval, P.; Sánchez-Portal, D.; Zabala, N.; Aizpurua, J. *ACS Nano* **2018**, *12*, 585-595.

22. Trautmann, S.; Aizpurua, J.; Götz, I.; Undisz, A.; Dellith, J.; Schneidewind, H.; Rettenmayr, M.; Deckert, V. *Nanoscale* **2017**, *9*, 391-401.

Chapter 7

7 Conclusions and Outlook

In this thesis, we have investigated plasmon-mediated chemistry, and designed new fractal structures for future applications. This has involved experiments using a variety of plasmon-mediated techniques, including surface- and tip-enhanced Raman spectroscopy, which are particularly useful for monitoring the plasmon-mediated reactions.

A general introduction of the wider application of plasmon-mediated reactions, to water splitting and carbon dioxide reduction, is elaborated. The goal of this research is to improve the efficiency of these plasmon-catalyzed reactions under visible light irradiation, such that they could be photocatalyzed by sunlight.[1,2] Following this discussion, the essential theoretical background for the understanding of plasmon-mediated chemistry is provided. The principles of Raman spectroscopy and plasmonics are described, followed by their combination in plasmon-mediated spectroscopy, particularly surface- and tip-enhanced Raman spectroscopy. The decay of plasmons, involving the ejection of hot carriers and subsequent heating effects, is discussed, including its coupling to chemical reactions. In Chapter 3, the technical details of these techniques are described, including the details of the fabrication of metallic nanostructures, the relevant optical microscopic and spectroscopic techniques, and the modelling of the light-matter interaction.

In Chapter 4, the plasmon-catalyzed reduction of aryl diazonium salts on gold surfaces is discussed. The reaction of both 4-nitrobenzenediazonium and 4-cyanobenzenediazonium was investigated on both gold nanoisland and gold nanoprisms formed by nanosphere lithography. Differentiation of plasmon-mediated and spontaneous grafting was not possible using surface-enhanced Raman spectroscopy. Using atomic force microscopy and scanning electron microscopy instead, large, periodic structures were observed where the laser was focused for plasmon-mediated grafting; this is preliminarily attributed to a

process similar to laser-induced periodic surface structures (LIPSS). This process is observed on both gold nanoisland and gold nanoprism substrates.

Chapter 5 of this thesis focusses on the tip-enhanced Raman spectroscopic measurements on silver nanoplates, which were synthesized by seed-mediated synthesis. Local ablation of the nanoplates was observed during spectral acquisition, with a pattern matching that of the tetrahedral tip. Plasmonic heating was discussed as a possible cause, followed by the estimation of plasmonic heating in our system through finite element calculations. It was concluded that plasmonic heating alone was not the cause of the damage; following energy dispersive X-ray spectroscopic measurements, it was discovered that silver had migrated to the tip. This makes the reduction of silver from the nanoplate onto the tip a likely cause of the ablation. Investigation into the precise processes and reactions involved could provide insight into plasmon-mediated chemical reactions controlled with nanoscale precision.

Designing new fractal nanostructures for future applications in plasmon-mediated chemistry is the focus of Chapter 6. Two fractal-based nanostructures are used, the Bethe lattice and the Sierpiński triangle, both of which were studied using experimental measurements and numerical calculations. For the Bethe lattice fractals, the experimental distributions of the electromagnetic near-field are observed through scanning near-field optical microscopy, for individual structures. This is then compared to the expected response as calculated through finite-difference time-domain methods. Sierpiński fractal nanostructures were fabricated in both silver and gold, and studied using the combination of finite-difference time-domain methods with electron energy loss spectroscopy and surface-enhanced Raman spectroscopy, respectively. For the fractal in silver, the effect of increasing the generation number of the fractal was studied, and it was concluded that this redshifted the primary dipolar energy. This can be used in future work to redshift the dipolar resonances without changing the footprint of the nanostructure, keeping in mind limits of nanofabrication techniques. Gold Sierpiński fractal metastructures were fabricated up to the eighth generation. The location of the electromagnetic hotspots was predicted by calculations, and the enhanced electric field was applied to surface-enhanced

Raman measurements. Analysis of the resultant maps showed the plasmon-mediated dimerization of the analyte during measurements.

Extension of this work could involve further investigation of the plasmon-mediated grafting of the diazonium salts. This would include determining if the effect is plasmon-mediated or photo-induced, and to what degree plasmonic heating contributes.

Laser power and exposure time can be optimized to achieve grafting patterned precisely at plasmonic hotspots.[3-5] As the location of the hotspots are dependent upon the intensity, wavelength and polarization of the excitation laser, the plasmonic platform can be multi-functionalized through sequentially grafting diazonium salts while changing polarization or wavelength parameters.[5] Multi-functionalization of surfaces represents a new and exciting avenue for surface chemistry (Figure 7-1a). Tip-enhanced Raman microscopy would be useful in investigating such functionalized platforms, the nanoscale resolution allowing for distinguishing regions where different molecules are functionalized.

These functionalized regions could be further modified to bind to a certain analyte, with the diazonium salt modified to detect only a select target. This could include glycan sensing, a molecule that is overexpressed in cancer cells, which has previously been investigated in the Lagugné group.[6]

When this is achieved, it can be applied to novel nanostructures, and the grafting can be observed as a function of different laser polarization and wavelengths. For this, the fractal structures recently developed, such as those described in Chapter 6 and shown in Figure 7-1b, are of particular interest since they present multiple resonances that can be excited by changing the wavelength and the polarization of light.[7,8]
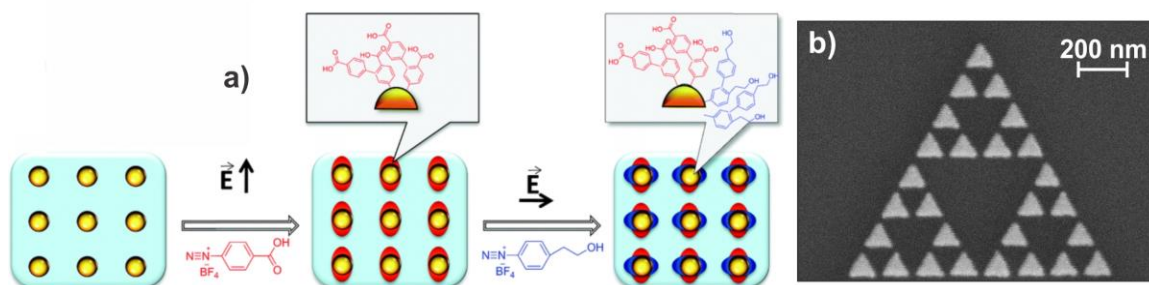
Figure 7-1 a) Multi-functionalization of simple gold nanodisks using different excitation polarizations. Adapted with permission from ref. [5]. Copyright 2018 Royal Society of Chemistry. b) Sierpiński fractal nanostructure, applicable to future studies in plasmon-mediated chemistry.

Critical to many fields of science, including food safety,[9,10] medicine,[11] and environmental monitoring,[9] is the detection of molecules in very low concentrations. This necessitates characterization methods that exhibit high sensitivity, label-free detection and high spatial resolution. Beyond the research community, this approach ultimately aims at developing more sensitive sensors with higher specificity towards a selected analyte.

7.1 References

1. Idriss, H. *Catal. Sci.* **2020**, *10*, 304-310.

2. Kawamura, G.; Matsuda, A. *Catalysts* **2019**, *9*, 982.

3. Nguyen, M.; Kherbouche, I.; Gam-Derouich, S.; Ragheb, I.; Lau-Truong, S.; Lamouri, A.; Lévi, G.; Aubard, J.; Decorse, P.; Félidj, N.; Mangeney, C. *Chem. Commun.* **2017**, *53*, 11364-11367.

4. Nguyen, V.-Q.; Ai, Y.; Martin, P.; Lacroix, J.-C. *ACS Omega* **2017**, *2*, 1947-1955.

5. Tijunelyte, I.; Kherbouche, I.; Gam-Derouich, S.; Nguyen, M.; Lidgi-Guigui, N.; de la Chapelle, M. L.; Lamouri, A.; Lévi, G.; Aubard, J.; Chevillot-Biraud, A.; Mangeney, C.; Felidj, N. *Nanoscale Horiz.* **2018**, *3*, 53-57.

6. Tabatabaei, M.; Wallace, G. Q.; Caetano, F. A.; Gillies, E. R.; Ferguson, S. S. G.; Lagugné-Labarthet, F. *Chem. Sci.* **2016**, *7*, 575-582.

7. Wallace, G. Q.; McRae, D. M.; Lagugné-Labarthet, F. *Opt. Lett.* **2019**, *44*, 3865-3868.

8. Bicket, I. C.; Bellido, E. P.; McRae, D. M.; Lagugné-Labarthet, F.; Botton, G. A. *ACS Photonics* **2019**, *6*, 2974-2984.

9. Tang, H.; Zhu, C.; Meng, G.; Wu, N. *J. Electrochem. Soc.* **2018**, *165*, B3098-B3118.

10. Lin, Z.; He, L. *Curr. Opin. Food Sci.* **2019**, *28*, 82-87.

11. Zhang, Y.; Wang, Z.; Wu, L.; Zong, S.; Yun, B.; Cui, Y. *Small* **2018**, *14*, 1704433.

Appendix A - Copyrights

Watching Visible Light-Driven CO2 Reduction on a Plasmonic Nanoparticle Catalyst

ACS Publications
Most Trusted. Most Cited. Most Read.

Author: Gayatri Kumari, Xueqiang Zhang, Dinumol Devasia, et al

Publication: ACS Nano

Publisher: American Chemical Society

Date: Aug 1, 2018

Copyright © 2018, American Chemical Society

Danielle McRae

Dear Danielle McRae,

Thank you for contacting The Optical Society.

For the use of material from Gregory Q. Wallace, Danielle M. McRae, and François Lagugné-Labarthet, "Probing mid-infrared plasmon resonances in extended radial fractal structures," Opt. Lett. 44, 3865-3868 (2019):

> Because you are the author of the source paper from which you wish to reproduce material, OSA considers your requested use of its copyrighted materials to be permissible within the author rights granted in the Copyright Transfer Agreement submitted by the requester on acceptance for publication of his/her manuscript. If the entire article is being included, it is requested that the **Author Accepted Manuscript** (or preprint) version be the version included within the thesis and that a complete citation of the original material be included in any publication. This permission assumes that the material was not reproduced from another source when published in the original publication.

> The **Author Accepted Manuscript** version is the preprint version of the article that was accepted for publication but not yet prepared and/or formatted by The Optical Society or its vendors.

While your publisher should be able to provide additional guidance, OSA prefers the below citation formats:

> For citations in figure captions:

> [Reprinted/Adapted] with permission from [ref #] © The Optical Society. (Please include the full citation in your reference list)

> For images without captions:

> Journal Vol. #, first page (year published) An example: Opt. Lett. 44, 3865 (2019)

Please let me know if you have any questions.

Kind Regards,

Rebecca Robinson

Rebecca Robinson
March 30, 2020
Authorized Agent, The Optical Society

The Optical Society (OSA)
2010 Massachusetts Ave., NW
Washington, DC 20036 USA
www.osa.org

Copyright Clearance Center

RightsLink®

Home | Help | Email Support | Sign in | Create Account

ACS Publications
Most Trusted. Most Cited. Most Read.

Carving Plasmon Modes in Silver Sierpiński Fractals

Author: Isobel C. Bicket, Edson P. Bellido, Danielle M. McRae, et al
Publication: ACS Photonics
Publisher: American Chemical Society
Date: Nov 1, 2019

Copyright © 2019, American Chemical Society

PERMISSION/LICENSE IS GRANTED FOR YOUR ORDER AT NO CHARGE

This type of permission/license, instead of the standard Terms & Conditions, is sent to you because no fee is being charged for your order. Please note the following:

- Permission is granted for your request in both print and electronic formats, and translations.
- If figures and/or tables were requested, they may be adapted or used in part.
- Please print this page for your records and send a copy of it to your publisher/graduate school.
- Appropriate credit for the requested material should be given as follows: "Reprinted (adapted) with permission from (COMPLETE REFERENCE CITATION). Copyright (YEAR) American Chemical Society." Insert appropriate information in place of the capitalized words.
- One-time permission is granted only for the use specified in your request. No additional uses are granted (such as derivative works or other editions). For any other uses, please submit a new request.

BACK   CLOSE WINDOW

RightsLink®

Welcome   Log out | Help

License Details

This Agreement between Ms. Danielle McRae ("You") and Elsevier ("Elsevier") consists of your license details and the terms and conditions provided by Elsevier and Copyright Clearance Center.

Print   Copy

License Number	4797220052997
License date	Mar 27, 2020
Licensed Content Publisher	Elsevier
Licensed Content Publication	Applied Catalysis B: Environmental
Licensed Content Title	Plasmon-induced photoelectrocatalytic activity of Au nanoparticles enhanced TiO2 nanotube arrays electrodes for environmental remediation
Licensed Content Author	Ling Wu,Fang Li,Yuanyuan Xu,Jane W. Zhang,Dieqing Zhang,Guisheng Li,Hexing Li
Licensed Content Date	Mar 1, 2015
Licensed Content Volume	164
Licensed Content Issue	n/a
Licensed Content Pages	8
Type of Use	reuse in a thesis/dissertation
Portion	figures/tables/illustrations
Number of figures/tables/illustrations	1
Format	both print and electronic
Are you the author of this Elsevier article?	No
Will you be translating?	No
Title	Plasmon-Enabled Physical and Chemical Transformations of Nanomaterials
Institution name	n/a
Expected presentation date	Jun 2020
Portions	Figure 2
Requestor Location	Ms. Danielle McRae
Publisher Tax ID	GB 494 6272 12
Total	0.00 CAD

BACK

Sierpiński Fractals as Plasmonic Metastructures for Second-Harmonic Generation

ACS Publications
Most Trusted. Most Cited. Most Read.

Author: Danielle M. McRae, Denis A. B. Therien, Renjie Hou, et al

Publication: ACS Applied Nano Materials

Publisher: American Chemical Society

Date: Mar 1, 2020

Copyright © 2020, American Chemical Society

License Details

This Agreement between Ms. Danielle McRae ("You") and John Wiley and Sons ("John Wiley and Sons") consists of your license details and the terms and conditions provided by John Wiley and Sons and Copyright Clearance Center.

Print   Copy

License Number	4797160812675
License date	Mar 27, 2020
Licensed Content Publisher	John Wiley and Sons
Licensed Content Publication	Angewandte Chemie International Edition
Licensed Content Title	Plasmon-Mediated Syntheses of Metallic Nanostructures
Licensed Content Author	Chad A. Mirkin, Michelle L. Personick, Mark R. Langille
Licensed Content Date	Nov 26, 2013
Licensed Content Volume	52
Licensed Content Issue	52
Licensed Content Pages	31
Type of Use	Dissertation/Thesis
Requestor type	University/Academic
Format	Print and electronic
Portion	Figure/table
Number of figures/tables	1
Will you be translating?	No
Title of your thesis / dissertation	Plasmon-Enabled Physical and Chemical Transformations of Nanomaterials
Expected completion date	Jun 2020
Expected size (number of pages)	160
Original Wiley figure/table number(s)	Figure 14
Requestor Location	Ms. Danielle McRae
Publisher Tax ID	EU826007151
Total	**0.00 CAD**

BACK

Copyright Clearance Center

RightsLink®

My Orders > Orders > All Orders

License Details

This Agreement between Ms. Danielle McRae ("You") and John Wiley and Sons ("John Wiley and Sons") consists of your license details and the terms and conditions provided by John Wiley and Sons and Copyright Clearance Center.

Print   Copy

License Number	4797160812675
License date	Mar 27, 2020
Licensed Content Publisher	John Wiley and Sons
Licensed Content Publication	Angewandte Chemie International Edition
Licensed Content Title	Plasmon-Mediated Syntheses of Metallic Nanostructures
Licensed Content Author	Chad A. Mirkin, Michelle L. Personick, Mark R. Langille
Licensed Content Date	Nov 26, 2013
Licensed Content Volume	52
Licensed Content Issue	52
Licensed Content Pages	31
Type of Use	Dissertation/Thesis
Requestor type	University/Academic
Format	Print and electronic
Portion	Figure/table
Number of figures/tables	1
Will you be translating?	No
Title of your thesis / dissertation	Plasmon-Enabled Physical and Chemical Transformations of Nanomaterials
Expected completion date	Jun 2020
Expected size (number of pages)	160
Original Wiley figure/table number(s)	Figure 14
Requestor Location	Ms. Danielle McRae
Publisher Tax ID	EU826007151
Total	**0.00 CAD**

BACK

License Details

This Agreement between Ms. Danielle McRae ("You") and Elsevier ("Elsevier") consists of your license details and the terms and conditions provided by Elsevier and Copyright Clearance Center.

Print   Copy

License Number	4797210108911
License date	Mar 27, 2020
Licensed Content Publisher	Elsevier
Licensed Content Publication	Materials Research Bulletin
Licensed Content Title	Plasmon mediated visible light photocurrent and photoelectrochemical hydrogen generation using Au nanoparticles/TiO2 electrode
Licensed Content Author	Wenjuan Chen,Yuhua Lu,Wen Dong,Zhuo Chen,Mingrong Shen
Licensed Content Date	Feb 1, 2014
Licensed Content Volume	50
Licensed Content Issue	n/a
Licensed Content Pages	5
Type of Use	reuse in a thesis/dissertation
Portion	figures/tables/illustrations
Number of figures/tables/illustrations	1
Format	both print and electronic
Are you the author of this Elsevier article?	No
Will you be translating?	No
Title	Plasmon-Enabled Physical and Chemical Transformations of Nanomaterials
Institution name	n/a
Expected presentation date	Jun 2020
Portions	Figure 1
Requestor Location	Ms. Danielle McRae
Publisher Tax ID	GB 494 6272 12
Total	**0.00 CAD**

BACK

Copyright
Clearance
Center

RightsLink®

My Orders > Orders > All Orders

License Details

This Agreement between Ms. Danielle McRae ("You") and John Wiley and Sons ("John Wiley and Sons") consists of your license details and the terms and conditions provided by John Wiley and Sons and Copyright Clearance Center.

Print   Copy

License Number	4797150593571
License date	Mar 27, 2020
Licensed Content Publisher	John Wiley and Sons
Licensed Content Publication	ChemCatChem
Licensed Content Title	Suzuki-Miyaura Cross-Coupling Using Plasmonic Pd-Decorated Au Nanorods as Catalyst: A Study on the Contribution of Laser Illumination
Licensed Content Author	Mattheus Verkaaik, Roos Grote, Nicole Meulendijks, et al
Licensed Content Date	Sep 18, 2019
Licensed Content Volume	11
Licensed Content Issue	19
Licensed Content Pages	7
Type of Use	Dissertation/Thesis
Requestor type	University/Academic
Format	Print and electronic
Portion	Figure/table
Number of figures/tables	1
Will you be translating?	No
Title of your thesis / dissertation	Plasmon-Enabled Physical and Chemical Transformations of Nanomaterials
Expected completion date	Jun 2020
Expected size (number of pages)	160
Original Wiley figure/table number(s)	Figure 1
Requestor Location	Ms. Danielle McRae

Publisher Tax ID	EU826007151
Total	**0.00 CAD**

BACK

My Orders   My Library   My Profile

Welcome   Log out | Help

My Orders > Orders > All Orders

License Details

This Agreement between Ms. Danielle McRae ("You") and Elsevier ("Elsevier") consists of your license details and the terms and conditions provided by Elsevier and Copyright Clearance Center.

Print   Copy

License Number	4797200707636
License date	Mar 27, 2020
Licensed Content Publisher	Elsevier
Licensed Content Publication	Chemical Physics
Licensed Content Title	Localized surface plasmons and hot electrons
Licensed Content Author	Kyle Marchuk,Katherine A. Willets
Licensed Content Date	Dec 5, 2014
Licensed Content Volume	445
Licensed Content Issue	n/a
Licensed Content Pages	10
Type of Use	reuse in a thesis/dissertation
Portion	figures/tables/illustrations
Number of figures/tables/illustrations	1
Format	both print and electronic
Are you the author of this Elsevier article?	No
Will you be translating?	No
Title	Plasmon-Enabled Physical and Chemical Transformations of Nanomaterials
Institution name	n/a
Expected presentation date	Jun 2020
Portions	Figure 4
Requestor Location	Ms. Danielle McRae
Publisher Tax ID	GB 494 6272 12
Total	**0.00 CAD**

BACK

Copyright Clearance Center | Marketplace™

Order Number: 1025301
Order Date: 27 Mar 2020

Payment Information

Danielle McRae

Payment method: Invoice

Billing Address:
Ms. Danielle McRae

Customer Location:
Ms. Danielle McRae

Order Details

1. Physical chemistry chemical physics

Billing Status:
Open

Order license ID	1025301-1
Order detail status	Completed
ISSN	1463-9084
Type of use	Republish in a thesis/dissertation
Publisher	ROYAL SOCIETY OF CHEMISTRY
Portion	Chart/graph/table/figure

0.00 CAD

LICENSED CONTENT

Publication Title	Physical chemistry chemical physics	Country	United Kingdom of Great Britain and Northern Ireland
Author/Editor	Royal Society of Chemistry (Great Britain)	Rightsholder	Royal Society of Chemistry
Date	01/01/1999	Publication Type	e-Journal
Language	English	URL	http://firstsearch.oclc.org/journal=1463-9076;screen=info;ECOIP

REQUEST DETAILS

Portion Type	Chart/graph/table/figure	Distribution	Canada
		Translation	Original language of publication
Number of charts / graphs / tables / figures requested	1	Copies for the disabled?	No

Format (select all that apply)	Print,Electronic	**Minor editing privileges?**	No
Who will republish the content?	Academic institution	**Incidental promotional use?**	No
Duration of Use	Life of current edition	**Currency**	CAD
Lifetime Unit Quantity	Up to 1,000,000		
Rights Requested	Main product		

NEW WORK DETAILS

Title	Plasmon-Enabled Physical and Chemical Transformations of Nanomaterials	**Institution name**	Western University
		Expected presentation date	2020-06-17
Instructor name	Danielle McRae		

ADDITIONAL DETAILS

The requesting person / organization to appear on the license	Danielle McRae

REUSE CONTENT DETAILS

Title, description or numeric reference of the portion(s)	Scheme 1	**Title of the article/chapter the portion is from**	Plasmon-mediated chemical transformation from alkane to alkene on a silver nanoparticle array under 532 nm excitation
Editor of portion(s)	N/A		
Volume of serial or monograph	21		
Page or page range of portion	7502-7507	**Author of portion(s)**	Royal Society of Chemistry (Great Britain)
		Publication date of portion	2019-03-11

Total Items: 1

Subtotal: 0.00 CAD

Order Total: 0.00 CAD

Copyright Clearance Center | **Marketplace™**

Order Number: 1026535
Order Date: 03 Apr 2020

Payment Information

Danielle McRae

Payment method: Invoice

Billing Address:
Ms. Danielle McRae

Customer Location:
Ms. Danielle McRae

Order Details

1. Nanoscale Horizons

Billing Status:
Open

Order license ID	1026535-1
Order detail status	Completed
ISSN	2055-6764
Type of use	Republish in a thesis/dissertation
Publisher	Royal Society of Chemistry
Portion	Chart/graph/table/figure

0.00 CAD
Republication Permission

LICENSED CONTENT

Publication Title	Nanoscale Horizons	Country	United Kingdom of Great Britain and Northern Ireland
Author/Editor	Guo jia na mi ke xue zhong xin (China),,Royal Society of Chemistry (Great Britain),	Rightsholder	Royal Society of Chemistry
Date	01/01/2016	Publication Type	e-Journal
Language	English		

REQUEST DETAILS

Portion Type	Chart/graph/table/figure	Distribution	Worldwide
		Translation	Original language of publication
Number of charts / graphs / tables / figures requested	1	Copies for the disabled?	No

Format (select all that apply)	Print,Electronic	**Minor editing privileges?**	No
Who will republish the content?	Academic institution	**Incidental promotional use?**	No
Duration of Use	Life of current edition	**Currency**	CAD
Lifetime Unit Quantity	Up to 1,000,000		
Rights Requested	Main product		

NEW WORK DETAILS

Title	Plasmon-Enabled Physical and Chemical Transformations of Nanomaterials	**Institution name**	Western University
		Expected presentation date	2020-06-01
Instructor name	Danielle McRae		

ADDITIONAL DETAILS

The requesting person / organization to appear on the license	Danielle McRae

REUSE CONTENT DETAILS

Title, description or numeric reference of the portion(s)	Scheme 1	**Title of the article/chapter the portion is from**	Multi-functionalization of lithographically designed gold nanodisks by plasmon-mediated reduction of aryl diazonium salts
Editor of portion(s)	n/a		
Volume of serial or monograph	3	**Author of portion(s)**	Guo jia na mi ke xue zhong xin (China),; Royal Society of Chemistry (Great Britain),
Page or page range of portion	53-57		
		Publication date of portion	2017-09-25

Total Items: 1

	Subtotal:	0.00 CAD
	Order Total:	**0.00 CAD**

Curriculum Vitae

Name: Danielle McRae

Post-secondary   Carleton University
Education and   Ottawa, Ontario, Canada
Degrees: 2011-2015 B.Sc. Chemistry & Physics

                   University of Western Ontario
                   London, Ontario, Canada
                   2015-2020 Ph.D. Physical Chemistry

Honours and   Mitacs Globalink Research Award
Awards: 2019

                   Oral Presentation Award, NanoOntario Conference
                   2018

                   NSERC Postgraduate Scholarship – Doctoral
                   2018-2020

                   L'Oréal Canada – France Canada Research Fund Fellowship
                   2017-2018

                   Ontario Graduate Scholarship
                   2017-2018; declined 2018-2019, 2016-2017

                   NSERC Canada Graduate Scholarship – Master's
                   2016-2017

                   Christian Sivertz Scholarship in Physical Chemistry
                   2015-2016

Related Work   Teaching Assistant
Experience   University of Western Ontario
                   2016-2019

Publications:

10. Bicket, I.; Bellido, E.; **McRae, D. M.;** Lagugné-Labarthet, F.; Botton, G. A. Hierarchical Plasmon Resonances in Fractal Structures. *ACS Photonics,* **2020**, *7,* 1246-1254.

9. **McRae, D. M.**; Therien, D.A.B.; Hou, R.; Wallace, G. Q.; Lagugné-Labarthet, F. Sierpiński Fractals as Plasmonic Metastructures for Second-Harmonic Generation. *ACS Appl. Nano Mater.,* **2020**, *3,* 3922-3929.

8. Villamagna, I. J.; **McRae, D. M.**; Borecki, A.; Lagugné-Labarthet, F.; Beier, F.; Gillies, E. R. GSK3787-Loaded Poly(ester amide) Particles for Intra-Articular Drug Delivery. *Polymers,* **2020**, *12,* 736.

7 Bicket, I.; Bellido, E.; **McRae, D. M.**; Lagugné-Labarthet, F.; Botton, G. Carving Plasmon Modes in Silver Sierpinski Fractals. *ACS Photonics*, **2019**, *6*, 2974-2984.

6. **McRae, D. M.**; Lagugné-Labarthet, F. In Search of the Hot-Spot. *Nat. Nanotechnol.* **2019**, 10.1038/s41565-019-0540-9

5. Wallace, G. Q.; **McRae, D. M.**; Lagugné-Labarthet, F. Probing Mid-Infrared Plasmon Resonances in Extended Radial Fractal Structures. *Opt. Lett.*, **2019**, *44*, 3865-3868.

4. **McRae, D. M.**; Jeon, K.; Lagugné-Labarthet, F. Plasmon-Mediated Drilling in Thin Metallic Nanostructures. *ACS Omega*, **2018**, *3*, 7269–7277

3. Ding, Z.; Stubbs, J.; **McRae, D.**; Blaquiere, J.; Lagugné-Labarthet, F.; Mittler, S. A Mass-Producible and Versatile Sensing System: Localized Surface Plasmon Resonance Excited by Individual Waveguide Modes. *ACS Sens.* **2018**, *3*, 334-341.

2. Wallace, G. Q.; Read, S. T.; **McRae, D. M.;** Rosendahl, S. M.; Lagugné-Labarthet, F. Exploiting Anisotropy of Plasmonic Nanostructures with Polarization Modulation Infrared Linear Dichroism Microscopy (µPM-IRLD). *Adv. Opt. Mater.,* **2018**, *6,* 1701336

1. Tabatabaei, M.; **McRae, D.**; Lagugné-Labarthet, F. Recent Advances of Plasmon-Enhanced Spectroscopy at Bio-Interfaces (2016) In *Frontiers of Plasmon Enhanced Spectroscopy*; Y. Ozaki, Ed.; ACS eBooks. 2: 183–207.